DISSERTATION

THE STRUCTURE AND DYNAMICS OF SUPERCOOLED SPC/E WATER CONFINED IN

SILICA NANOPORES AND EQUILIBRIUM GLASSY FILMS: A TWO-SYSTEM STUDY

Submitted by

Nicholas J. Kuon

Department of Physics

In partial fulfillment of the requirements

For the Degree of Doctor of Philosophy

Colorado State University

Fort Collins, Colorado

Spring 2019

Doctoral Committee:

   Advisor: R. Mark Bradley
   Co-Advisor: Grzegorz Szamel

   Martin Gelfand
   Ted Watson

ABSTRACT

THE STRUCTURE AND DYNAMICS OF SUPERCOOLED SPC/E WATER CONFINED IN

SILICA NANOPORES AND EQUILIBRIUM GLASSY FILMS: A TWO-SYSTEM STUDY

Supercooled liquids and glasses is still an area of active research. Despite the wide use of glass in society today, the underlying physics of this phase of matter still contains mysteries. This thesis will examine two different systems of supercooled liquids via molecular simulation and investigate the two systems' structure and dynamics. We first study the temperature dependence of the structure and dynamics of supercooled water confined in hydrophilic silica nanopores. In particular, we focus on the self-intermediate scattering functions. We simulate this system using the SPC/E model of water. These water molecules are confined in model MCM-41 nanopores with radii of 20, 30, and 40 Å. The structure of the water within the pores is first examined and it is found that water molecules form layers near the wall of the pores. However, in the center of the pores, the density is relatively uniform. Using this fact, the pore is divided into two regions: the core and the shell regions. The dynamics of the water molecules that start in each region are then compared. We measure the mean squared displacements and the self-intermediate scattering functions for these two regions. These measurements allows for connection with quasi-elastic neutron scattering experiments. The dependence of the self-intermediate scattering function on direction and magnitude of the wavevector is examined, as well as the function's dependence on proximity to the pore surface. In addition, the rotational-translational decoupling is measured, and it is found that the decoupling is weakly temperature dependent. The second system studied is an equilibrium glassy film deposited onto a substrate in a manner akin to vapor deposition. Glasses created in this manner can have higher kinetic stabilities and different thermodynamic properties than glasses prepared by liquid cooling. This is due to the enhanced mobility of particles at the surface of the film, which allows the particles to find lower potential energy states. We

study the temperature dependence of the average and single particle dynamics for particles that start at the surface of the film and for those particles that start in the bulk of the film. First, we examine the average dynamics by calculating the self-intermediate scattering functions and their relaxation times for particles that start in the surface or the bulk region. Then, we calculate the probability of the logarithm of single particle displacements for particles starting in the surface and bulk regions. We find that, in both regions, the distribution of single particle displacements indicate subpopulations of fast and slow particles. This is indicative of heterogeneous dynamics. We also find that the single particle dynamics of particles on the surface mirror particles in the bulk. However, the mirrored dynamics occur several orders of magnitude faster for particles on the surface than for those in the bulk.

ACKNOWLEDGEMENTS

Thanks to the people that have introduced me to the subject matter and have helped me along the way. These people include: Dr. Branka Ladanyi (R.I.P.), Dr. Grzegorz Szamel, Dr. Elijah Flenner, Dr. Anatoli Milischuk, and Dr. Hannah Staley.

DEDICATION

This is thesis is dedicated to the late Professor Branka Ladanyi. I would also like to dedicate this to my parents, family and friends for their continued support throughout the years.

TABLE OF CONTENTS

LIST OF TABLES

LIST OF FIGURES

Chapter 1

Introduction

1.1   Motivation

A supercooled liquid is a liquid that has been cooled below its normal freezing temperature and yet remains a liquid. However, this state of matter isn't only useful for entertainment value in youtube videos of water bottles in freezers. A supercooled liquid is the first step toward the creation of an amorphous solid, also known as the glassy state of matter. The glassy state of matter has been used by humanity for millennia for a wide variety of practical uses that are now ubiquitous in society. Thus, it should come as a surprise to most that the theory of supercooled liquids and glasses is still in its infancy and remains an elusive topic in the scientific community. This thesis will consider two different systems of supercooled liquids; examine their properties; contribute new information to their respective fields; and push the boundaries of understanding.
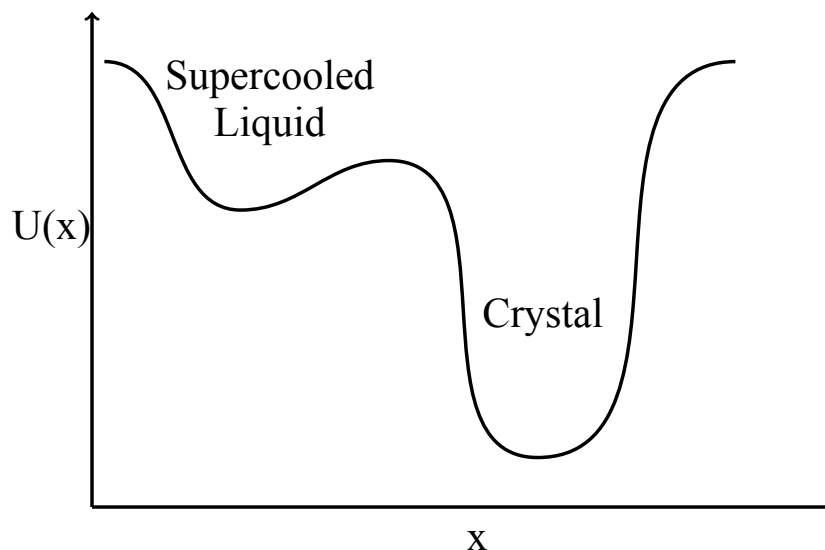
Figure 1.1: Conceptual diagram of potential energy landscape

Figure 1.1 will be used to introduce the concept of a potential energy landscape, a common concept that helps explain the behavior of supercooled liquids. The figure depicts the potential energy of the liquid system as a function of the position coordinates of the particles within the liquid. Consider a liquid system that is within a potential energy landscape as shown in figure 1.1. The liquid system can explore this landscape and will eventually settle into an equilibrium state. The landscape has two potential energy minima: a local minimum and a global minimum. A local maximum lies between the two minima. The local and global minima may be interpreted, respectively, as a supercooled liquid and a crystalline solid.

As the liquid is cooled, it is most likely to end up in the global minimum. If the liquid is cooled quickly enough, however, it will not have time to fully explore its potential energy landscape. Thus, it may end up in the local minimum for a time. However, this minimum is metastable. A large enough energy "kick" to this liquid will cause it to fall into the global minimum of the crystal phase. The maximum between the supercooled liquid minimum and the crystal minimum is called a transition state.

An example of the metastability of a supercooled liquid is the demonstration of water as a supercooled liquid. Water, if pure and placed in a smooth enough container, may be placed in a freezer for an extended amount of time and remain a liquid. Thus, it becomes a supercooled liquid. Once removed from the freezer, hitting the bottle on a table will cause supercooled liquid to immediately crystallize. In Figure 1.1, this is interpreted as the supercooled water being given a large enough energy kick for it to settle into its crystalline minimum.

Figure 1.10 shows a more complex version of figure 1.1. In this figure, the temperature T_g is called the glass transition temperature. This temperature is the point at which the material has fallen out of equilibrium, a characteristic of a liquid's transition to an amorphous solid. The temperature T_A indicates the temperature at which a supercooled liquid begins to exhibit non-Arrhenius dynamics, a topic that will be explored in a later section. As can be seen, there are multiple basins and transition states in the potential energy landscape. As is expected, the lowest is the crystalline state. There are multiple basins corresponding to glasses and supercooled liquids.
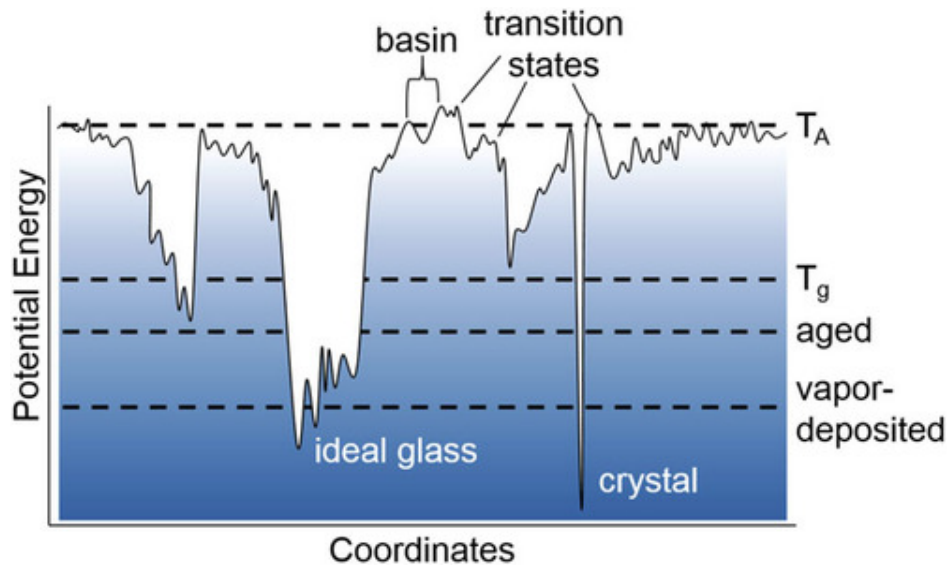
Figure 1.2: Diagram of potential energy landscape. Reprinted with permission from M.D. Ediger, J. Chem. Phys. **147**, 210901 (2017). Copyright 2017 American Physical Society.

A glass is no longer in equilibrium. A glass that has been aged is, thus, in a deeper basin of the potential energy landscape. The deepest basin, for a glass, on the figure is a vapor-deposited glass. Glasses that have been created via vapor-deposition show remarkably higher stability in comparison with aged glasses. A glass that is lower in its potential energy landscape will be more stable than other glasses, thus making it useful for practical applications as it has relatively constant thermodynamic properties with respect to time. A glassy system prepared via vapor-deposition is one of the two systems studied in this thesis.

This thesis will explore two systems: supercooled water confined in hydrophilic silica nanopores; and a supercooled liquid film. For the water system, the motivation will be the difficulty of exploring water's phase diagram in its supercooled and amorphous solid phases. Confining water in nanoporous structures presents an opportunity to more easily access this region, and is thus a matter of scientific significance. The supercooled liquid film system will be studied to determine the stability of glassy films created by vapor deposition. This thesis will investigate the cause of this stability and the details of its mechanisms.

1.2 Molecular Simulation

The research done in this thesis was completed using two simulation techniques: Molecular Dynamics (MD) and Monte Carlo (MC) simultions. These techniques are used to simulate many-particle systems when analytical techniques are either impossible or too complex to be practical. Simulation is often used as a bridge to connect the physical descriptions of multi-particle systems to experimental studies. Computer simulations of liquids are often referred to as "computer experiments."

1.2.1 Molecular Dynamics

Molecular dynamics (MD) simulations are the most intuitive of the two molecular simulations and constitute a "brute force" method of simulating the time-evolution of multi-particle systems. MD simulations proceed as follows: the system's initial properties, positions and velocities are selected; the forces on each of the particles are computed; Newton's laws are then integrated for each of the particles; and the latter two steps are repeated until the time evolution of the system for the desired length of time is completed [3]. Upon completion, the averages of measured quantities such as temperature, pressure, kinetic energy etc. are computed and the trajectories of the individual atoms are output.

The core of the MD simulation is the integration of Newton's Laws of motion. A variety of algorithms have been developed for accomplishing this step. The primary MD algorithm used in this work is the velocity-Verlet algorithm [47, 106]. In this algorithm, a small timestep, Δt, is defined and the position and velocity of each particle, represented by the index i, is expanded into a Taylor series. The algorithm is implemented as follows: [3]

1. $\mathbf{r}_i(t + \Delta t) = \mathbf{r}_i(t) + \mathbf{v}_i(t)\Delta t + \frac{1}{2\mathrm{m}}\mathbf{F}_i(t)\Delta t^2$

2. $\mathbf{a}_i(t + \Delta t) = -\sum_{j\neq i}^{N} \frac{\nabla U[\mathbf{r}_{ij}(t+\Delta t)]}{\mathrm{m}}$

3. $\mathbf{v}_i(t + \Delta t) = \mathbf{v}_i(t) + \frac{1}{2}\left[\mathbf{a}_i(t) + \mathbf{a}_i(t + \Delta t)\right]\Delta t$

A molecular dynamics simulation is primarily implemented in the following steps: initialization, equilibration, and production. In the initialization phase, the desired number of particles are placed within a simulation box of a desired volume. For computational ease, they are often placed on a cubic lattice. The particles are given initial velocities that are chosen from a Boltzmann distribution corresponding to the desired temperature of the simulation. Periodic boundary conditions are implemented for particles leaving and entering the box. In the equilibration step, an MD simulation is implemented until thermodynamic quantities have reached approximate constant average values in time, thus indicating equilibrium. In the production phase, MD simulations of a desired length are performed on the equilibrated system and configurations (the positions, velocities, and forces of each particle) are output every n timesteps. Upon completion of a production run, the trajectory may be used to calculate pertinent physical quantities.

Ensembles in Molecular Dynamics

MD simulations are used to simulate the time evolution of a system of N particles within a volume V. The energy E is a constant of the motion. If it is assumed that time averages of a system property are equivalent to ensemble averages, then time averages of the results of an MD simulation are ensemble averages of the microcanonical ensemble [1]. Thus, direct simulation of other ensembles, such as the canonical ensemble, is not impossible. However, schemes have been developed that allow other ensembles to be simulated in MD simulations.

The method used in this thesis of performing MD simulations in ensembles other than the microcanonical ensemble involve the reformulation of the Lagrangian equations of motion of the system. This method utilizes an extended Lagrangian that contains additional, but artificial, coordinates and velocities. These artificial additions to the Lagrangian may be interpreted as having connected the system to a thermostat or a barostat that keeps the quantity in question (in this thesis, the pressure and/or the temperature) relatively constant over the course of the simulation [2]. The primary ensembles used in this thesis are the canonical (constant N, V and T) ensemble and the isobaric-isothermal (constant N, P and T) ensemble. These were simulated using the Nosè-Hoover thermostat and barostat [3].

1.2.2 Monte Carlo Simulations

In statistical mechanics, average thermodynamic properties of a system are calculated by evaluating integrals of the form

$$\langle \phi \rangle = \int d^{3N}\mathbf{x}\, \phi(\mathbf{x}^N) f(\mathbf{x}^N). \tag{1.1}$$

In this equation, $\mathbf{x}$ is the position coordinate, N is the number of particles, $\mathbf{x}^N$ is the set of position coordinates, $\phi(\mathbf{x}^N)$ is a physical observable, and $f(\mathbf{x}^N)$ is a probability distribution normalized such that $f(\mathbf{x}^N) \geq 0$ and $\int d^{3N}\mathbf{x}\, f(\mathbf{x}^N) = 1$.

The Monte Carlo method evaluates these integrals by performing trial moves on the particles. The trial moves may be attempts at translations, rotations, box volume changes or the creation of particles. These trial moves are accepted or rejected according to the distribution $f(\mathbf{x}^N)$. If the system is in a state $\mathbf{x}^N$, the trial moves are accepted or rejected according to the following algorithm:

1. A trial move is attempted that takes the system from state $\mathbf{x}^N$ to state $\mathbf{y}^N$.

2. The distributions $f(\mathbf{x}^N)$ and $f(\mathbf{y}^N)$ are calculated.

3. The trial move is accepted with probability $A(\mathbf{x}^N|\mathbf{y}^N) = \min\left[1, f(\mathbf{x}^N)/f(\mathbf{y}^N)\right]$.

This process is continued until convergence is achieved.

The Gibbs Ensemble

The ensemble used for the Monte Carlo simulations in this thesis is called the Gibbs ensemble. It is primarily used for calculating phase coexistence curves as these are commonly measured in experiment. The conditions for phase coexistence in a one component system are such that the temperature T, pressure P, and chemical potential μ of both phases are equal. However, since T, P and μ are intensive quantities, no ensemble exists that holds all three constant.

In a series of papers, Panagiotopoulos derived an ensemble such that Monte Carlo simulations may be used to calculate phase coexistence curves [41, 42]. In this ensemble, the two phases are kept in separate simulation boxes. The Monte Carlo simulation is performed in either the canonical

(constant N, V and T) or the isobaric-isothermal (constant N, P and T) ensemble. For this thesis, the isobaric-isothermal ensemble is used. Trial moves are attempted that insert/delete particles from one box into the other box, translate/rotate the particles, or change volume of the boxes. In this manner, the simulation may be continued until the equilibrium condition stated in the above paragraph is achieved.

1.2.3 The SPC/E Model

The molecular simulation of water provides its own difficulties. In fact, a review listed 46 models of water, each with its own advantages and disadvantages [4]. However, some models of water are used more than others, and this thesis uses a model that was chosen to best balance accuracy, computational efficiency and connection to previous studies. For this work, the model of water used is known as the Simple Point Charge Extended (SPC/E) model [49].
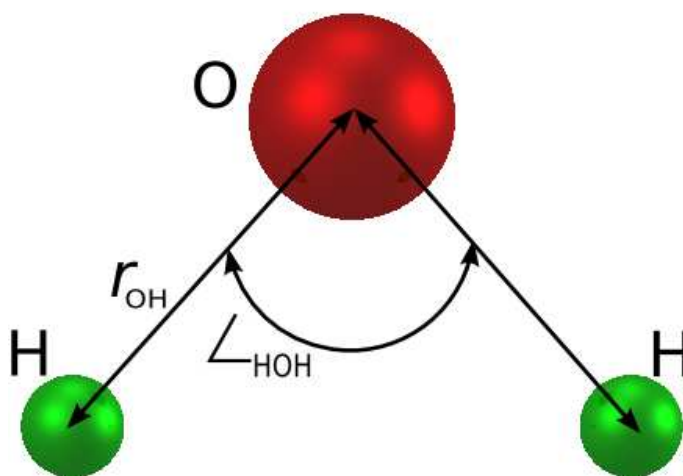
Figure 1.3: Diagram showing model structure of SPC/E water.

The SPC/E model of water is an modified version of a three-site model of water called the SPC model. This three-site model is shown in figure 1.3. This model contains two hydrogen atoms and one oxygen atom. These three atoms are connected via rigid bonds of length 1.0 Åand a fixed angle θ_{HOH}. The potential type between the water molecules is of Lennard-Jones plus Coulomb-type and

has the functional form,

$$u(r_{ij}) = 4\epsilon_{ij} \left[\left(\frac{\sigma_{ij}}{r_{ij}} \right)^{12} - \left(\frac{\sigma_{ij}}{r_{ij}} \right)^{6} \right] + \frac{q_i q_j}{4\pi\epsilon_0 r_{ij}}. \tag{1.2}$$

In this expression, i and j are particle indices with $i \neq j$, ϵ and σ are the Lennard-Jones site parameters, and q is a partial charge. The Lennard-Jones sites are situated on the oxygen atoms. The values given to these parameters are shown in the table below [49].

Table 1.1: SPC/E water model potential parameters

Potential Parameter	Value
σ	3.166 Å
ϵ	0.650 kJ/mol
r_{OH}	1.00 Å
$\angle HOH$	109.47
q_O	-0.8467e
q_H	$|q_O|/2$

This model is used in this thesis for all situations involving the simulation of water.

1.2.4 The Kob-Anderson Model

The model used in this work to simulate supercooled equilibrium films is called the Kob-Anderson model [103–105]. In this model, two particles, called A and B particles, make up the liquid. The A-particles are larger than the B-particles and the liquid that they make up has a mixture of 80% A-particles and 20% B-particles. These particles interact via a Lennard-Jones interaction potential (the first term in equation 1.2).

The following table shows the Lennard-Jones parameters for the Kob-Anderson model. In this table, the parameters for interactions between A and A particles, B and B particles, and A and B particles are listed as AA, BB and AB respectively. We note that, for this system, the Lennard-Jones parameters are written in units of σ_{AA} and ϵ_{AA}.

Table 1.2: Kob-Andersen potential parameters

Potential Parameters	Values
ϵ_{AA}	1.0
ϵ_{AB}	1.5
ϵ_{BB}	0.5
σ_{AA}	1.0
σ_{AB}	0.8
σ_{BB}	0.88

1.3   Analysis of Simulations

Upon completion of simulations, analysis of the results is crucial to the interpretation of the simulations. The usual outputs from a MD simulation are the positions of all particles at each time t, and the quantities calculated may only depend on the position variable and time. Fortunately, the trajectory of the system at each timestep is sufficient to calculate most quantities important to compare with experimental results. In this section, we will outline the primary quantities calculated in this thesis, how they behave as a liquid is supercooled, and their relation to quantities measured in experiments.

1.3.1   Liquid Structure

The structure of the liquid refers to time-independent quantities that quantify how particle positions are correlated with their positions at later times and with other particles' positions. These quantities can be used to determine the short and long-range structural order that is present in the system. There are two primary quantities that are commonly calculated to get a good picture of the structure of a liquid: The probability that a particle has a position between $\mathbf{r}$ and $\mathbf{r} + d\mathbf{r}$, and the probability that a set of two particles are separated by a distance $\mathbf{r}'$ and $\mathbf{r}' + d\mathbf{r}'$ [5]. The first of these quantities is the local number density of the liquid, defined as

$$\rho(\mathbf{r}) = \left\langle \sum_{i=1}^{N} \delta(\mathbf{r} - \mathbf{r}_i) \right\rangle. \tag{1.3}$$

. The local number density is defined in terms of the positions of the particles as In this expression, the sum is over all particles in the system and the angular brackets denote an ensemble average [5].
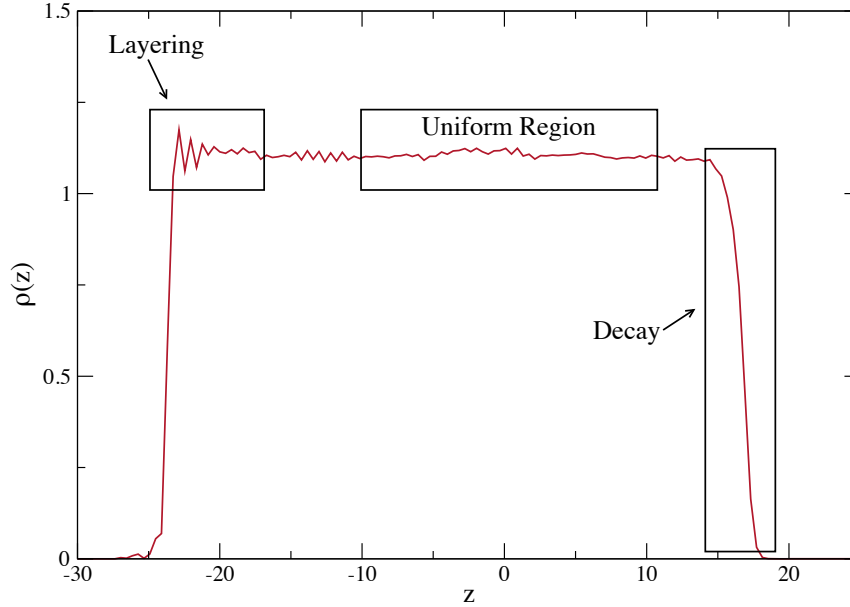
Figure 1.4: Plot of density versus z-coordinate of a Kob-Andersen glassy film. Different regions of the density diagram are labeled and boxed.

The following figure shows an example liquid number density. The density is of a film of Kob-Andersen particles deposited onto a substrate and therefore is a function of position z. Important features of the density have been boxed and labeled. Easily seen are the initial decays of the density when the edges of the film are reached, and the uniform region in the center of the film. The small peaks just before the uniform region of the film are indicative of features called layers [6]. They are characteristic of density profiles that are in the vicinity of a surface. Layering affects are seen in both systems studied in this thesis.

The probability that a set of two particles are separated by a distance $\mathbf{r}'$ and $\mathbf{r}' + d\mathbf{r}'$ is slightly more complicated. It is defined as

$$g(r) = \frac{1}{\rho} \left\langle \frac{1}{N} \sum_{i=1}^{N} \sum_{j \neq i} \delta(\mathbf{r} - \mathbf{r}_j + \mathbf{r}_i) \right\rangle . \tag{1.4}$$

In this equation, the index i is over all particles, and index j is over all particles different from particle i. This quantity is called the radial distribution function, or the pair correlation function [5].
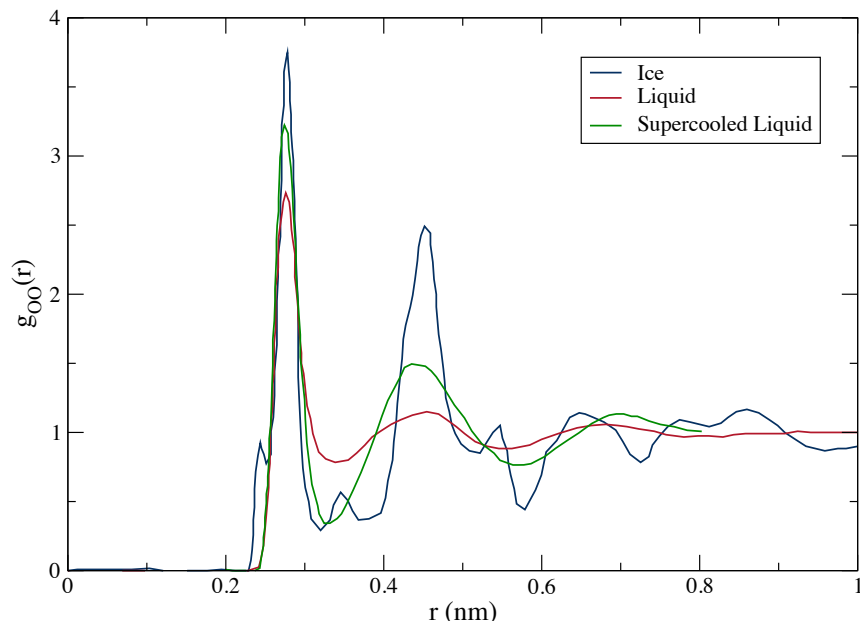
Figure 1.5: Radial distribution function of the different phases of water. The red curve corresponds to the stable liquid, the blue curve corresponds to ice, and the green curve corresponds to the supercooled liquid. Data taken from L.G. Pettersson and A. Nilsson, *J. Non-Cryst. Liquids* **407**, 399 (2015) and A. K. Soper, *J. Chem Phys.* **258**, 121 (2000).

The following figure shows the radial distribution function for the SPC/E model of water. It is a function of radial distance away from the reference particle. The reference particles, in this case, are the oxygen atoms. Each curve on the figure shows a different phase of water. The red curve shows the liquid phase at 300 K; the green curve is the supercooled liquid phase [7]; and the blue curve is the crystalline phase [8]. As can be seen, the liquid phase and the supercooled liquid phase are very similar. A first large peak is present at approximately the same distance away from the reference oxygen in each phase. This is indicative of the nearest oxygen neighbors of the reference oxygens. At larger values of r, this peak if followed a series of smaller peaks before the function converges to a value of unity. The only differences between the supercooled liquid and the normal liquid are a difference in heights of the peaks (the supercooled liquid peaks are higher) and width

(the supercooled liquid peaks are narrower). Their overall structure is very similar. The crystalline curve, however, is more striking. The crystalline curve has several more peaks indicating a higher level of order. This is associated with the higher tetrahedral order of ice. As can be seen, the pair correlation function is indispensable for helping to identify the phase of a substance as well as its underlying structure.

1.3.2   Liquid Dynamics

Of fundamental importance to the analysis of the dynamics of a liquid is the mean squared displacement (MSD),

$$\langle \delta r^2 \rangle = \left\langle \frac{1}{N} \sum_{i=1}^{N} (\mathbf{r}_i(t) - \mathbf{r}_i(0))^2 \right\rangle. \tag{1.5}$$

In this equation, the angled brackets are an ensemble average and $\mathbf{r}_i(t)$ is the position at time t. At short times, particles undergo ballistic motion and $\langle \delta r^2 \rangle \propto t^2$ At long times, the motion is diffusive and the MSD obeys the following relation

$$\lim_{t \to \infty} \langle \delta r^2 \rangle = 2fDt. \tag{1.6}$$

In this equation, D is the diffusion coefficient, and f is the number of spatial dimensions used to calculate the MSD [3].

Figure 1.6 shows the mean squared displacements of a bulk Kob-Anderson liquid as a function of time. Multiple curves are shown on the plot, with each individual curve being at a different temperature. As can be seen, the motion at long times is linear as in equation 1.6.

At intermediate times, a plateau can be seen developing as the temperature is lowered. This feature of the MSD is indicative of supercooling and is the result of particles being trapped in cages of their nearest neighbors. As the liquid is supercooled further, this plateau typically lowers in height and persists for a longer length of time. This plateau continues to persist for longer and longer periods of time as the liquid is further supercooled. In the limit that the supercooled liquid
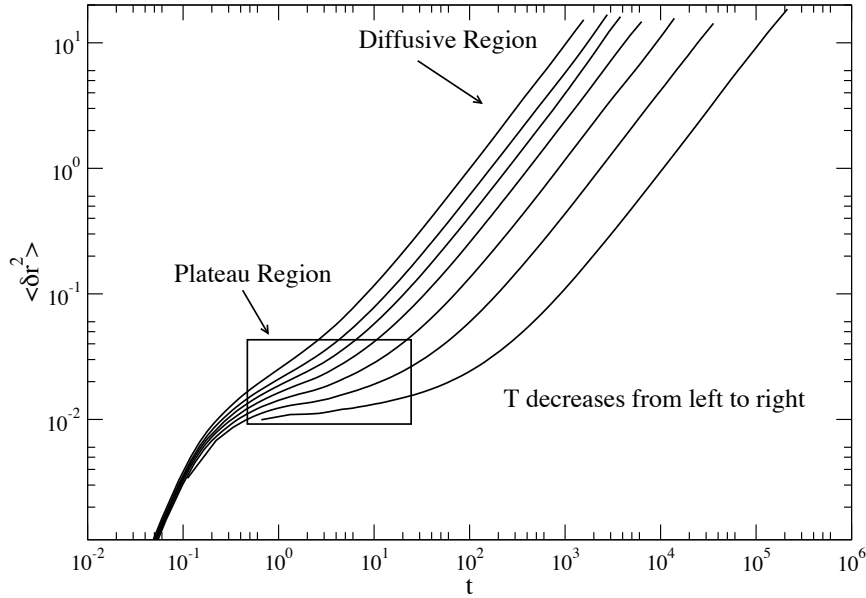
Figure 1.6: Mean squared displacement of bulk Kob-Anderson particles. Each curve represents a different temperature and the important regions are labeled and/or boxed.

becomes an amorphous solid, this plateau will persist for longer timescales than are accessible by experiments.

Density Auto-correlation Functions

Along with the MSD, the primary analysis functions used in this thesis will be density auto-correlation functions. The easiest to intuit of these is the self-van Hove function which is defined as

$$G_S(\mathbf{r}, t) = \frac{1}{\rho} \left\langle \sum_{i=1}^{N} \delta(\mathbf{r} - \mathbf{r}_i(t) + \mathbf{r}_i(0)) \right\rangle. \tag{1.7}$$

The function $G_S(\mathbf{r}, t)d\mathbf{r}$ may be physically interpreted as the probability that particle i has moved a distance $\mathbf{r}$ in a time t [5].

Although the self-van Hove function is easier to grasp intuitively, the Fourier Transforms of this function are of importance to analysis of experimental results. In particular, we will analyze the spatial Fourier Transform of the self-van Hove function

13

$$F_S(\mathbf{k}, t) = \frac{1}{2\pi} \int_{-\infty}^{\infty} G_S(\mathbf{r}', t) \exp(i\mathbf{k} \cdot \mathbf{r}') \, d\mathbf{r}' \qquad (1.8)$$

where $\mathbf{k}$ is the wavevector. For the confined water system, the wavevector will be denoted by $\mathbf{Q}$. This function is known as the self-intermediate scattering function (SISF) [5].
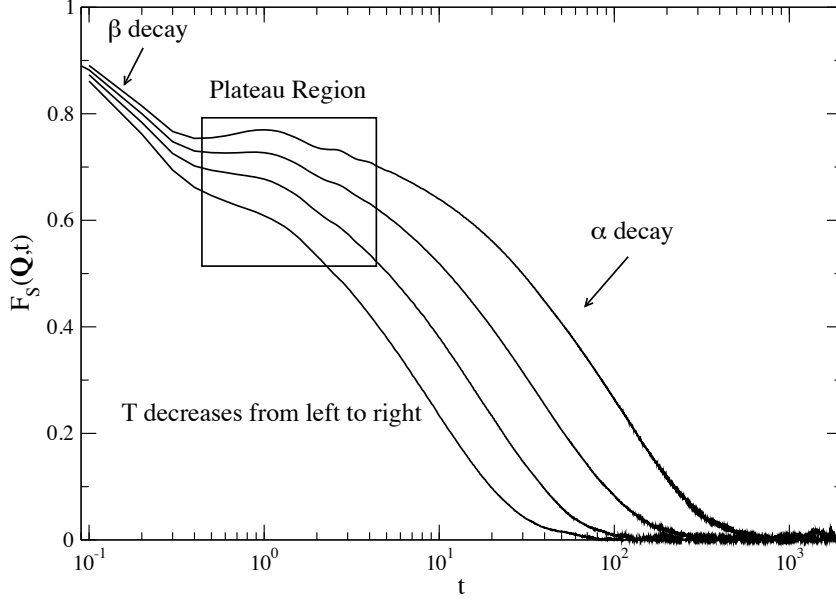
Figure 1.7: Self-Intermediate scattering functions of SPC/E water at a specified Q-value of 1.89^{-1}. Each curve corresponds to a different temperature.

Figure 1.7 shows the self-intermediate scattering function for bulk SPC/E water as a function of time. Each curve is for a different temperature, with the longer decays occurring at the lower temperatures. In general, two different relaxation timescales can be seen. The first is called beta relaxation and encompasses ballistic motion before the molecule interacts with its neighbors. At long times, there is a decay that lengthens in time as the temperature is lowered. This is called alpha relaxation and is often fit to a stretched exponential function, i.e.

$$F_S(\mathbf{Q}, t \to \infty) \approx e^{-(t/\tau)^{\beta}} \qquad (1.9)$$

At intermediate times, a plateau develops in the self-intermediate scattering function.

This plateau is indicative of the same motion seen at intermediate times in the MSD and implies that the molecules are trapped in a cage of their nearest neighbors. As with the MSD, this plateau lengthens as a liquid is supercooled, becoming infinite in length with the transition to an amorphous solid. An important quantity determined from the SISF is the alpha relaxation time, τ_α, which is often defined via

$$F_S(\mathbf{Q}, \tau_\alpha) = 1/e \tag{1.10}$$

At certain points in this thesis, 0.2 will be used instead of 1/e, but it is out of convenience that this value is used.

The diffusion coefficient extracted from the mean squared displacement and the alpha relaxation time are both measured of the average dynamics of particles in the system. In fact, at small values of the wavevector $\mathbf{Q}$, the two quantities are inversely proportional to each other and are related through the wavevector $\mathbf{Q}$ by,

$$\tau_\alpha = \frac{1}{|\mathbf{Q}|^2 D}. \tag{1.11}$$

Figure 1.8 shows the alpha relaxation time, τ_α of SPC/E water at a Q-value of $1.89\,^{-1}$ versus temperature. It also shows the diffusion coefficient for SPC/E water calculated in the form of equation 1.11. As can be seen, the two quantities have the same quantitative behavior, with only small differences occurring as the temperature is lowered. This difference is to be expected. As the temperature is lowered, the dynamics change and are better described as a stretched exponential.

Average Dynamics

The behavior of the alpha relaxation time and the diffusion coefficient with temperature is a way of quantifying how the average dynamics of a given system vary as the temperature is lowered. These dynamics vary in specific ways for different types of glasses, but may be categorized as having Arrhenius dynamics or non-Arrhenius dynamics.

In Arrhenius dynamics, the relaxation time (or the inverse diffusion coefficient) versus temperature can be fit to the Arrhenius equation,
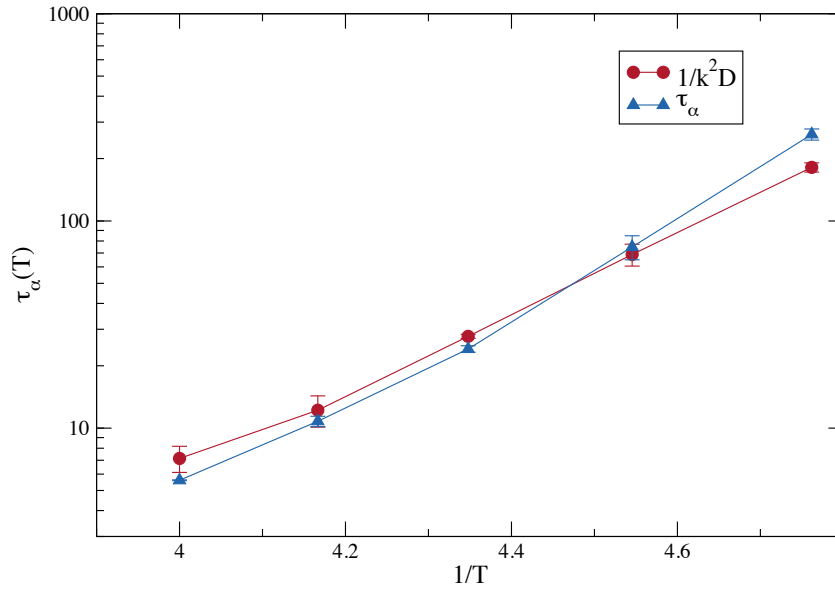
Figure 1.8: The alpha relaxation time, and the diffusion coefficient in the form of equation 1.11 are shown versus temperature for SPC/E water. The blue curve is the alpha relaxation time, while the red curve is the diffusion coefficient.

$$\tau_\alpha(T) = \tau_0 e^{\frac{E_A}{k_B T}} \tag{1.12}$$

where k_B is Boltzmann's constant and E_A is an activation energy [9]. Glasses that have Arrhenius dynamics are called strong glasses. In contrast, a glass that has non-Arrhenius dynamics is called a fragile glass. These glasses generally fit to an equation attributed to Volger, Fulcher, and Tamman (VFT) [10–12] given as,

$$\tau_\alpha(T) = \tau_0 e^{\frac{A}{T-T_0}} \tag{1.13}$$

where T_0 represents a temperature at which the relaxation time diverges and A is a constant akin to an activation energy.

Figure 1.9 shows the viscosity of a variety of glass-forming materials versus T_g/T, where T_g is the glass transition temperature. The viscosity is related to the diffusion coefficient (and hence the alpha relaxation time) through the Stokes-Einstein equation,
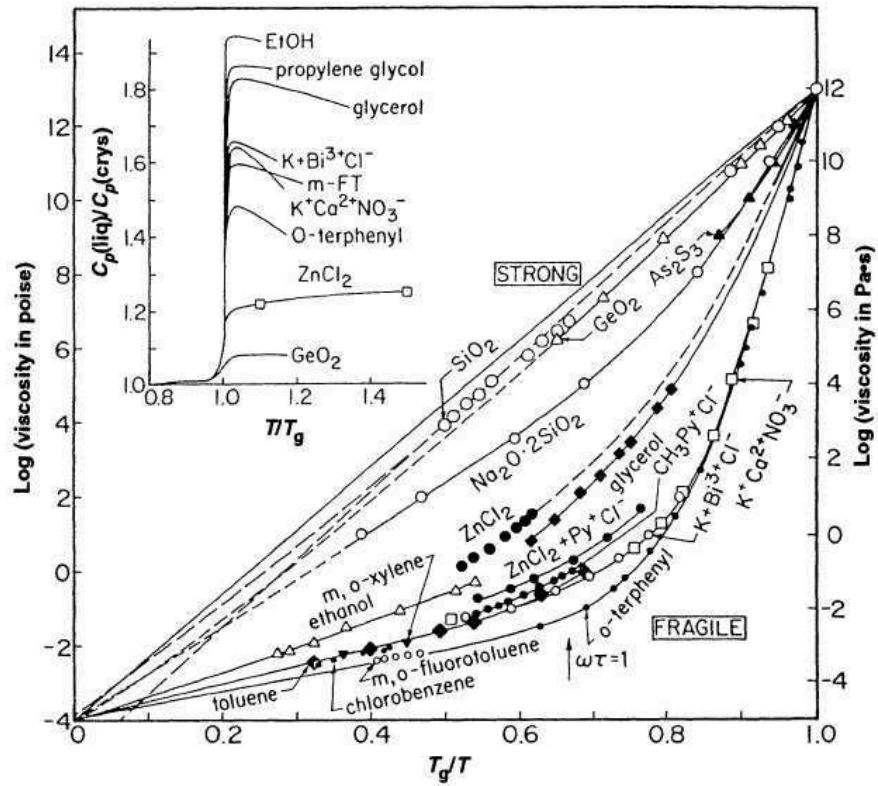
Figure 1.9: Arrhenius plot of multiple glass-formering materials highlighting Arrhenius and non-Arrhenius dynamics. *Republished with permission from the American Association for the Advancement of Science.*

17

$$D \propto \frac{k_b T}{\eta}, \tag{1.14}$$

where η is the viscosity. The materials in figure 1.9 that follow a straight line are those that have Arrhenius dynamics, and are labeled in the figure as strong. Those that do not follow a straight line have non-Arrhenius dynamics, and are labeled in the figure as fragile.

1.4 Confined Supercooled Water in Silica Nanopores

Despite its omnipresence in our lives, water on a scientific level still contains mysteries. The molecule's affinity for hydrogen bonding makes the study of its properties at supercooled temperatures a daunting task. In fact, water in the bulk is impossible to supercool past a certain temperature. This temperature is known as the homogeneous nucleation temperature. At temperatures below the homogeneous nucleation temperature , which is approximately 235 K, nucleation sites spontaneously form in the bulk liquid. This results in crystallization of the liquid. If pressures of up to 0.3 GPa are applied, the the homogeneous nucleation temperature may be lowered by about 50 K, but crystallization is still inevitable [19]. These areas of the supercooled liquid phase of water have been given the nickname "no-man's land." At ambient pressure, this region is between approximately 230 K and 150 K.

The following figure shows the pressure-temperature phase diagram of water between the temperatures of 273.15 K and 73 K. The "no-man's land" section of the phase diagram is bounded by the dashed lines and coexistence curves are shown as solid black lines. As can be seen from the figure, the region is bounded below by two types of amorphous solid: low density and high density. These two types of amorphous solid may be experimentally created through vapor deposition, vitrification of micron-sized water drops through hyperquenching, and amorphization of ice through high pressure or radiative means [20]. The region is bounded above by supercooled water, which is created by the method of quenching a bulk water sample.

The "no-man's land" region of the supercooled water phase diagram thus remains a difficult to explore region. As a result, methods have had to be developed in order to study this region.
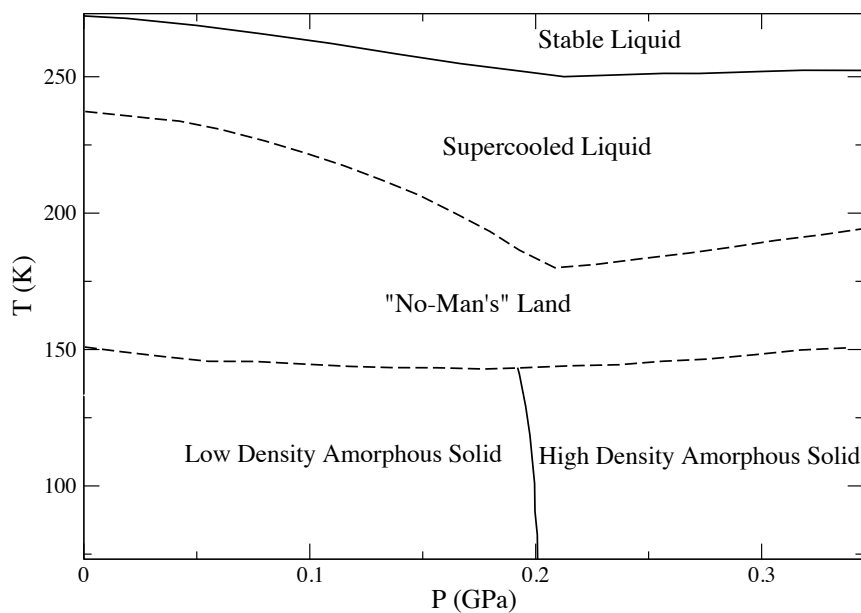
Figure 1.10: Phase diagram of supercooled and amorphous water. The no-man's land region has been highlighted and coexistence curves between supercooled liquid and amorphous solid and supercooled liquid and stable liquid are shown and the different regions are labeled. Data taken from K. Amann-Winkel, R. Böhmer, F. Fujara, C. Gainaru, B. Geil, and T. Loerting, Rev. Mod. Phys. **88**, 011002 (2016).

The most promising of these systems for a model of supercooled water is water under heavy confinement. The following sections will outline the effects that heavy confinement has on water; the types of confinement and the materials materials used for them; and the connection of molecular simulation studies of highly confined water with experiment.

1.4.1 Motivation for Studying Nano-Confined Supercooled Water

The primary motivation for studying supercooled water under high confinement is that heavy confinement supresses water's transition to the crystalline phase. The melting temperature of water under high confinement in cylindrical nanopores has been shown to lower as as the radius decreases. [33]

Through thermodynamic arguments, it is possible to understand the physics of this phenomenon by balancing the free energy contributions from the solid and liquid phase from both interfacial (next to the pore wall) and bulk water inside the pore. Using this analysis, it has been found that cylindrical pores of radius R obey the following relation,

$$\Delta T_m = T_m - T_{m,pore} = \frac{2T_m(\gamma_{ws} - \gamma_{wl})v_1}{Rh_m}. \tag{1.15}$$

In this equation, T_m and $T_{m,pore}$ are the melting temperatures of bulk liquid and liquid confined to the pore respectively; γ_{ws} and γ_{wl} are wall-solid and wall-liquid surface tensions; v_1 is the molar volume of the liquid; and h_m is the molar enthalpy of melting [13].

Figure 1.11 shows the melting temperature of water confined to cylindrical, silica nanopores versus the inverse radius of the pores [14]. Two types of silica nanopores are shown, MCM-41 and SBA-15, to get the largest temperature range. The homogeneous nucleation temperature is the dotted horizontal line. As can be seen, the melting temperature lowers dramatically as the radius of the nanopore is lowered. In fact, the melting temperature of water in a 4 Å and smaller radius pore is below the homogeneous nucleation temperature.
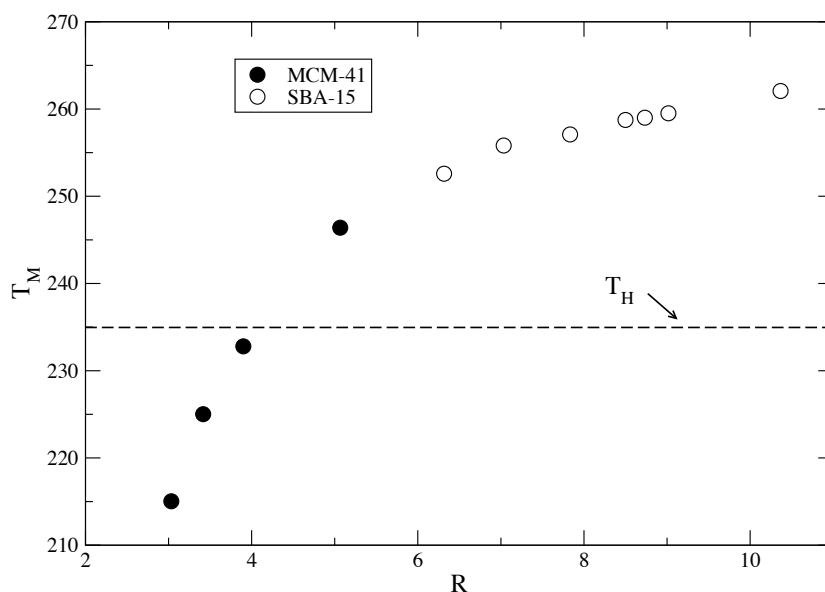
Figure 1.11: The melting temperature of confined water versus pore radius are shown. Data is collected from two confining systems: MCM-41 and SBA-15 and is taken from G.H. Findenegg, S. Jähnert, D. Akcakayiran, and A. Schreiber, ChemPhysChem, **9** 2651-2659. Copyright 2008 Wiley-VCH.

This implies that the "no-man's" land of the supercooled water phase diagram may be bypassed using nano-confinement, and it is indeed an area of high focus. In particular, the average dynamics of nano-confined water have been shown to have both Arrhenius and non-Arrhenius regimes.

Figure 1.12 shows the inverse diffusion coefficient of water confined in MCM-41 silica nanopores versus inverse temperature. As can be seen, when compared with figure 1.9, there are in fact two dynamic regimes. The first occurs for $T > 230K$ and is non-Arrhenius in nature. The second occurs for $T < 230K$ and is Arrhenius in nature. Why this change in dynamics occurs is still a matter of controversy [20].

1.4.2 MCM-41 Nanopores

Many different materials can be used to put water under heavy confinement. In general, the materials used can be classified into two groups: hard and soft confinement. Soft confinement involves combining water with a solute in order to simulate confinement. The materials used for soft confinement are sugars, salts, biomaterials, liquid crystals etc [19]. This thesis will not inves-
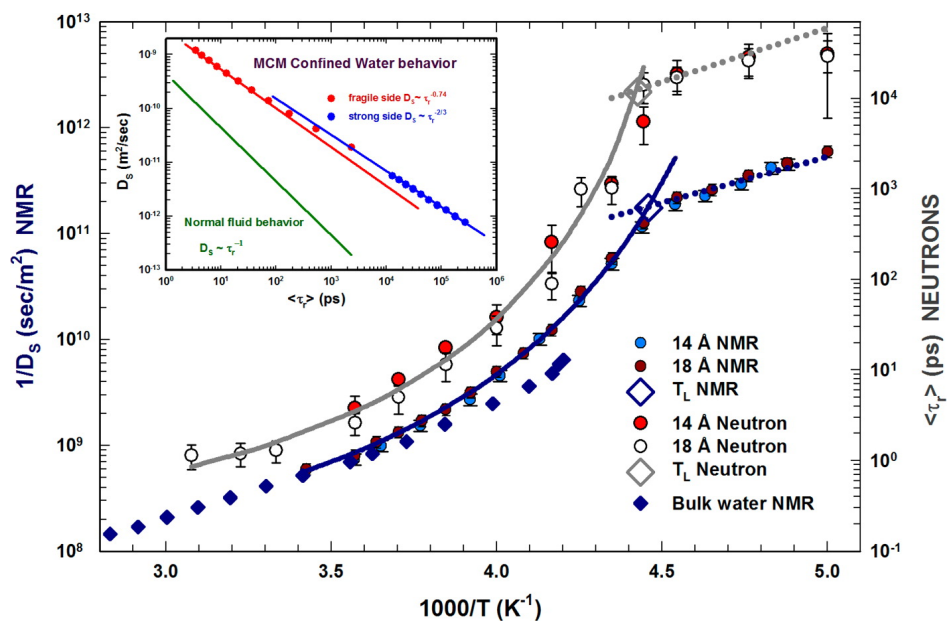
Figure 1.12: Arrhenius plot of several experimental studies of confined water systems. *Reprinted with permission from S. Cerveny, F. Mallamace, J. Swenson, M. Vogel, and L. Xu, Chemical Reviews 216 7608-7625 (2016). Copyright 2016 American Chemical Society.*

tigate soft confinement, and instead will focus on hard confinement. Hard confinement involves the confinement of water in rigid nanoporous structures. These structures vary in terms of material and geometry but are generally classified in terms of the length scale of their confinement [19].

As experimental techniques such as quasi-elastic neutron scattering (QENS) use macroscopic samples of the material to be used for hard confinement, it is useful that the material being used has regularity in its nanoporous structures. As a further restriction, materials that have minimal interaction with water at the surface of the nanopores are desired as water interaction with the pore surface would affect the overall behavior of the water within the pores and hinder comparison with water in the bulk. Two materials are known for these properties: SBA-15 and MCM-41, both of which being mesoporous silica [19]. MCM-41 has a simpler structure than SBA-15, and so this thesis has made MCM-41 the primary focus for generating results.

MCM-41 was developed by the Mobile corporation in 1983. It consists of cylindrical nanopores the radii of which may be controlled by the synthesis of the material. Figure 1.13 shows a picture
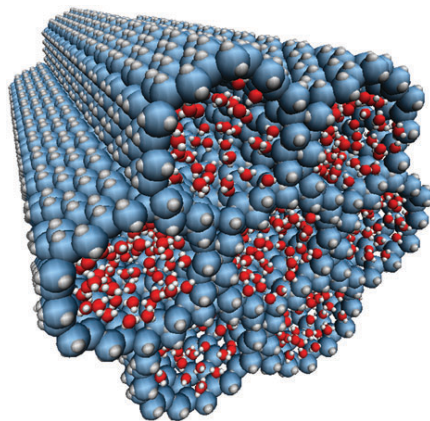
Figure 1.13: Structure of MCM-41 material. *Reprinted with permission from C. Bertrand, Y. Zhang, S.H. Chen, Phys. Chem. Chem. Phys.* **15**, *721 (2013). Copyright 2013 Wiley-VCH.*

of the general structure of MCM-41 hydrated with water. As can be seen, the structure consists of stacked cylindrical nanopores that, in general have the same radius [23].

1.4.3   Connection with Experiment

The focus of this thesis' study of confined supercooled water in MCM-41 nanopores will be the connection of molecular dynamics simulations with quasi-elastic neutron scattering (QENS) studies. QENS experimental studies measure the dynamic structure factor, $S(\mathbf{Q}, \omega)$ of the material being studied [5]. The dynamic structure factor is related to the previously mentioned self-intermediate scattering function (SISF) via a Fourier transform

$$S(\mathbf{Q}, \omega) = \frac{1}{2\pi} \int_{-\infty}^{\infty} F_S(\mathbf{Q}, t) e^{i\omega t} \, \mathrm{d}t \qquad (1.16)$$

Although direct comparison of a SISF calculated via a molecular dynamics simulation and a dynamic structure factor extracted from a QENS study is difficult due to the specifics of the experiment, a qualitative comparison may be performed.

The total self-intermediate scattering functions of water are a function of translational, rotational and vibrational motion. In general,

270

$$F_S(\mathbf{Q}, t) = F_S^T(\mathbf{Q}, t) F_S^R(\mathbf{Q}, t) F_S^V(\mathbf{Q}, t) \tag{1.17}$$

where T, R and V stand for translational, rotational, and vibrational respectively. QENS experiments cannot resolve vibrational motion [15], and so for the purposes of this thesis it can be assumed that $F_S^V(\mathbf{Q}, t) = 1$. However, there still remains the contributions from translational and rotational motion to the QENS spectra.

It is not possible for QENS experiments to separate the rotational and translational parts of the spectra, so it is often assumed that the rotational and translational motion is uncoupled, i.e.

$$F_S(\mathbf{Q}, t) \approx F_S^T(\mathbf{Q}, t) F_S^R(\mathbf{Q}, t). \tag{1.18}$$

In general, this assumption is not perfectly valid so it would be helpful to estimate the coupling of translational and rotational motion. Luckily, molecular dynamics simulations have access to translational and rotational motion separately, and so can provide a jumping-off point to measure the coupling of the two types of motion. Previous molecular dynamics studies of this system have used the connected SISF, defined as,

$$F_S^{con}(\mathbf{Q}, t) = F_S(\mathbf{Q}, t) - F_S^T(\mathbf{Q}, t) F_S^R(\mathbf{Q}, t), \tag{1.19}$$

to measure translational-rotational coupling.

Figure 1.14 shows the connected self-intermediate scattering function for water confined to MCM-41 nanopores of three different radii at a temperature of 300 K. Each figure is a different Q-value in the axial direction of the pore. As can be seen, the translational-rotational coupling contributes a small, but not negligible amount to the total SISF. The connected SISF rises to a maximum as time increases and decreases at large times. There is more coupling in the smaller pore sizes and the larger Q-value. How this function behaves with temperature is investigated in chapter 3.
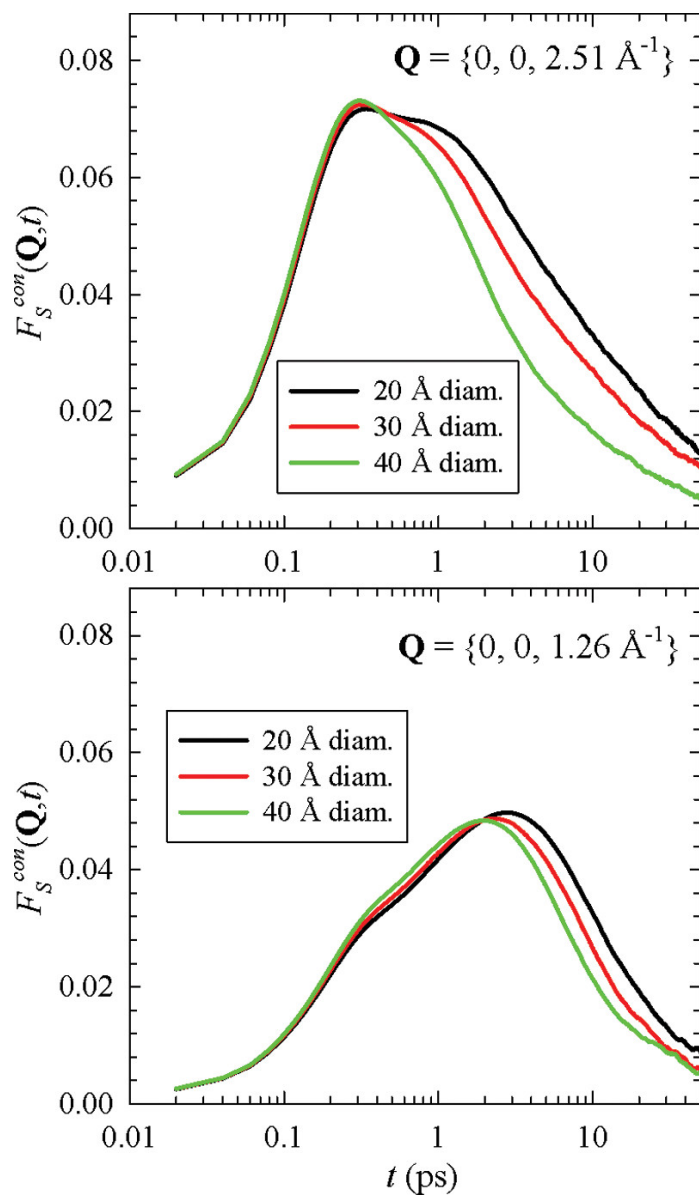
Figure 1.14: Connected self-intermediate scattering function for water confined in three sizes of model MCM-41 nanopores. The temperature is 300 K. Each panel shows a different Q-value with the inset showing the Q-vector. *Reprinted with permission from A.A. Milischuk, V. Krewald, and B.M. Ladanyi, J. Chem. Phys. 136, 224704 (2012).*

1.5   Creation of Ultra-Stable Glasses via Vapor Deposition

Glasses are ubiquitous in their use today. With so many types and creation techniques, what makes some glasses more advantageous to use than others? Kinetic stability, the glass' tendency to remain a glass, is a major source of advantageous properties of glasses. Glasses made through the process of vapor deposition have been shown to be ultra-stable. This section will discuss what makes ultra-stable vapor deposited glasses so advantageous and will provide evidence as to the source of this ultra-stability.

1.5.1   Vapor-Deposited Glasses: Creation and Properties

We will overview the creation and properties of vapor-deposited glasses in this section. In the process, particles are bled off of a coil, and journey across the vacuum, at a rate pre-determined by the coil, and settle on a substrate at the bottom of the chamber. The particles are built up, layer by layer, until a suitable thickness is achieved on top of the substrate. The choice of substrate, chamber temperature, and deposition rate are crucial to the final result, and may be tailored to create the desired product.

Glasses prepared in this manner have been shown to be ultra-stable, but what exactly does "ultra-stable" mean? From a intuitive standpoint, stability of a glass would be related to the glass' ability to remain a glass and not transition into the crystalline phase as time passes. Crystallization would inherently change the thermodynamic properties of the glass over time and a desirable property of a glass would be a high ability to resist crystalization. Glasses are often chosen for applications like optics for being very homogenous on macroscopic scales, and thus, a glass that slowly loses homogeneity over time due to crystallization would be an undesired property. Vapor-deposited glasses provide a means for creating ultra-stable glasses.

In addition to ultra-stability, vapor-deposited glasses have a number of other interesting and highly practical properties. Vapor-deposited glasses have been shown to have a higher density than glasses created by liquid cooling [16]. High densities glasses would require long time scales to
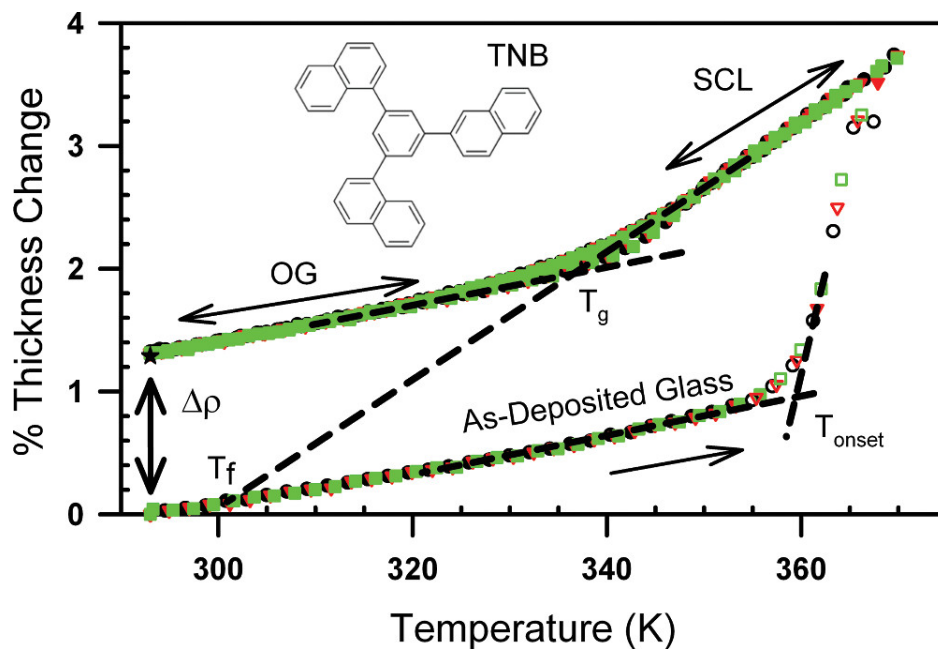
Figure 1.15: Molar volume of tris-naphthylbenzene (1,3-bis(1-naphthyl)-5-(2- naphthyl)benzene) versus temperature. *Reprinted with permission from M.D. Ediger, J. Chem. Phys.* **147**, *210901 (2017). Copyright 2017 American Physical Society.*

be created by simply cooling a liquid, and thus vapor-deposition is an ideal candidate for creating these types of glasses. This property is important for industrial and/or medical applications.

Figure 1.15 shows the results of the density of a vapor-deposited glass versus a glass created by ordinary liquid cooling [16]. As can be seen from the figure, the vapor-deposited substance exhibits a much higher density than the ordinary liquid-cooled substance even at temperatures above the glass transition. In order to achieve similar densities, the ordinary glass would have to be cooled to a far lower temperature. This would require far more time as the glass would need to be cooled at a much slower rate. Thus the vapor-deposited glass is a far easier method of achieving high density glasses.

Another property of vapor-deposited glasses that is in contrast to their liquid-cooled counterparts is their lower heat capacity. For processes like lithography, a glass with a low heat capacity can save energy during the process. Figure 1.16 shows the heat capacity of a conventional glass versus an ultra-stable vapor-deposited glass. As can be seen at a temperature of about 3 K, the heat capacities of the two glasses separate. At all temperatures below 3 K, the vapor deposited glass
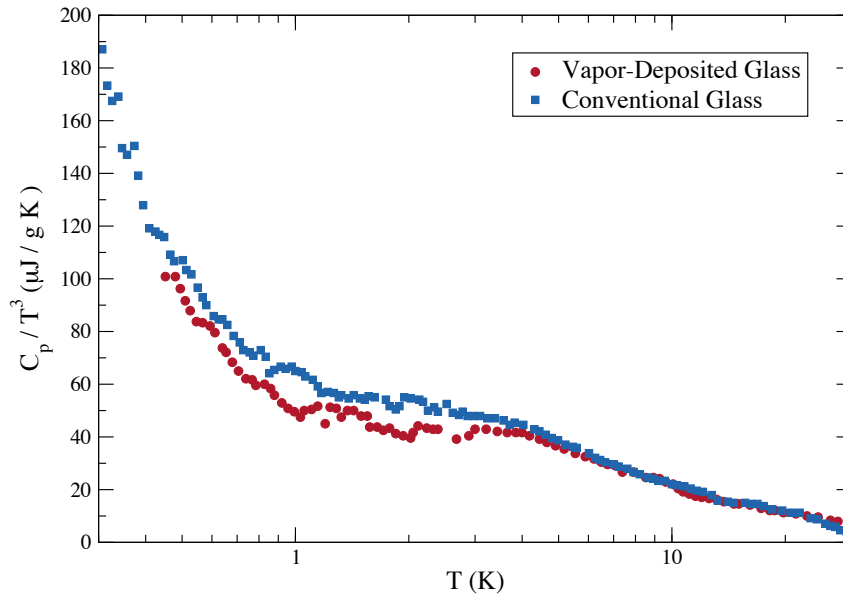
Figure 1.16: Heat capacity at constant pressure versus temperature for a vapor-deposited glass as opposed to a conventional glass created via liquid cooling. Data taken from Perez-Castaneda et al., Proc. Natl. Acad. Sci. U. S. A. **111**, 11275-11280 (2014). Copyright 2014 Authors.

has a lower heat capacity than the conventional glass created through liquid cooling. Thus vapor-deposited glasses are a method of creating glasses with lower heat capacity than those created via liquid cooling.

1.5.2 Explanation of Ultra-Stability in Vapor-Deposited Glasses

The stability, high density, and lower heat capacity of vapor-deposited glasses when compared to ordinary liquid-cooled glasses is an interesting scientific phenomenon. An explanation as to the source of these properties is needed. This section will provide an explanation for these properties, the evidence for this explanation, as well as areas of further understanding.

It was noted above that the rate of deposition is very important to the overall characteristics of the material created by vapor deposition. This is, in large part, due to the mobility of the particles that are on the surface of the deposited film. As intuition suggests, it is far easier to move around when you are on the surface of something as opposed to being surrounded by it. The same can be said for particles on the surface of the deposited film. Particles in a vapor-deposited glass,

having spent at least some of their time on the surface of the glass, have had the opportunity to explore more of the configurational space accessible to them. Thus, they have been able to settle into a lower potential energy state than those particles that were simply cooled down in the bulk. Particles in a glass are trapped for an enormous amount of time within cages made of their nearest neighbors. Being vapor-deposited at a slower rate allows these particles to choose their neighbors more carefully.
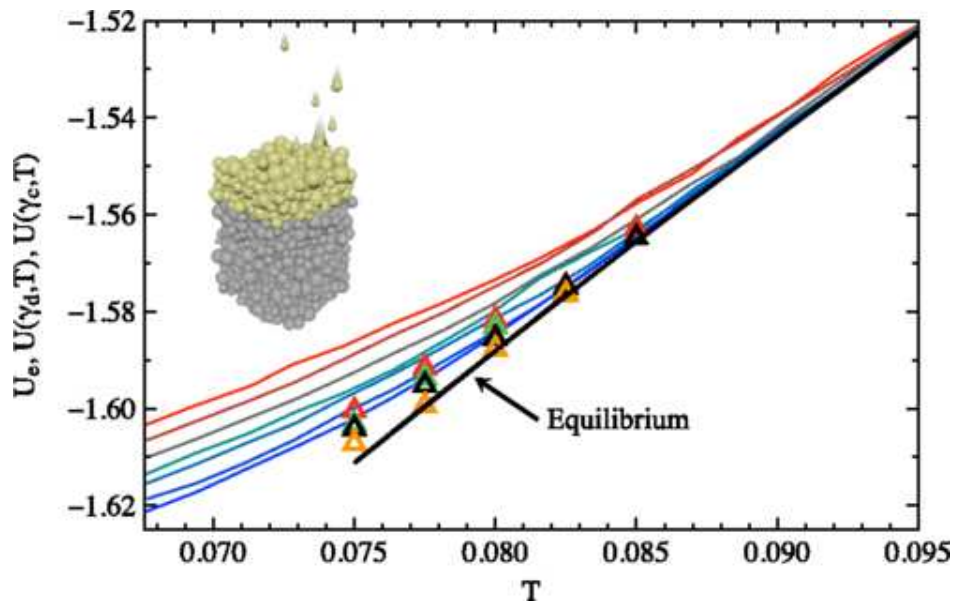
Figure 1.17: Potential energy versus temperature for liquid-cooled glasses and glassy films that were deposited at different rates. The solid lines represent liquid-cooled glasses with different cooling rates, and the open triangles are vapor deposited glasses at different deposition rates. The black line represents an equilibrium supercooled liquid. *Reprinted with permission from L. Berthier, P. Charbonneau, E. Flenner, and F. Zamponi Phys. Rev. Lett. 119, 188002 (2017). Copyright 2017 American Physical Society.*

Figure 1.17 shows the average potential energy of vapor-deposited glasses and liquid-cooled glasses vs. temperature [74]. The open triangles represent a vapor-deposited glass that was deposited at a different rate with the red triangles having the fastest rate of deposition and blue having the lowest rate of deposition. As can be seen, at all temperatures, the glass having the slowest deposition rate has the lowest potential energy. Thus, the deposition rate plays an important role in the stability of vapor-deposited glasses, and thus do the motion of the surface particles.

As further evidence that the surface particles are responsible for the ultra-stability of vapor-deposited glasses, we will examine the mobility of the surface particles. If the surface particles have a significantly higher mobility than those particles in the bulk of the film, this will lend credence to the idea that surface particles explore more of the available configurational space.
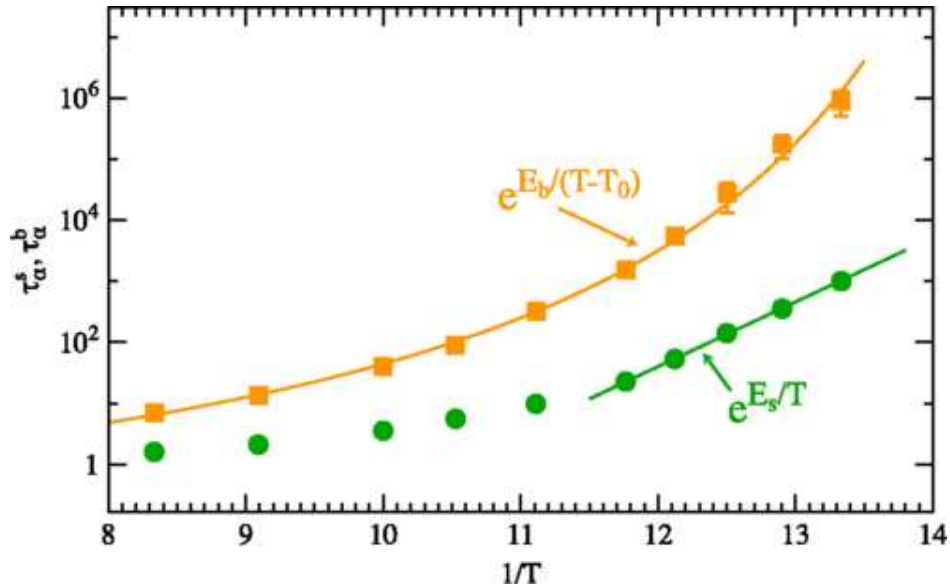
Figure 1.18: Arrhenius plot of the alpha relaxation time for particles that start in the bulk region of a glassy film (orange) and particles that start on the surface of a glassy film (green). *Reprinted with permission from L. Berthier, P. Charbonneau, E. Flenner, and F. Zamponi Phys. Rev. Lett. 119, 188002 (2017). Copyright 2017 American Physical Society.*

Figure 1.18 shows the relaxation time as a function of inverse temperature for a vapor-deposited glass [74]. The two curves shown are for particles that started within the bulk of the vapor-deposited film (orange), and particles that began on the surface of the vapor-deposited film. As can be seen, the particles that began on the surface of the film are more mobile than particles that began within the bulk region of the film at all temperatures. At the lowest temperature, the two regions differ in their relaxation times by almost four orders of magnitude. Thus, it can be concluded that the particles at the surface of a vapor-deposited film are much more mobile than their counterparts within the bulk of the film.

At this point, it becomes necessary to address the next steps within research of this area. The average nature of the the dynamics of the surface particles as opposed to the bulk particles has been examined and the contrast has been shown to be quite different. What remains to be seen is the nature of the single-particle dynamics of these regions. Do the particles on the surface behave dynamically very differently than those within the bulk, or do they behave similarly but on drastically different timescales? These are some of the questions that still remain unanswered, and will be given answers in Chapter 4.

1.6   Overview

This thesis will be divided into five chapters including this introduction. The second chapter will consist of the analysis of the methods used and the structure of confined supercooled water in hydrophilic MCM-41 nanopores of three sizes. This chapter will explore the techniques used for creating and hydrating the nanopores; the density of the water with the nanopore; the orientation of the water molecules within the pore; and the degree of tetrahedral ordering of the molecules within the pore.

The third chapter will delve into the dynamics of confined supercooled water in hydrophilic MCM-41 nanopores of three sizes. It will investigate the qualitative behavior of the total, translational rotational and connected self-intermediate scattering functions. This chapter will also investigate the mean squared displacements, alpha relaxation times and SISFs for water molecules that start in different regions of the pore. It will also quantify the temperature behavior of the alpha relaxation times and the diffusion coefficients.

The fourth chapter will focus on the single particle dynamics of a glassy film of Kob-Anderson particles. After providing an introduction to the material, this chapter will describe the creation of the glassy film as well as the details of the simulations run. Then, it will investigate the general properties of the film such as the self-intermediate scattering functions for particles that start in the bulk of the film and for particles that start at the surface of the film. The temperature behavior of the alpha relaxation times for particles that start in the bulk/surface regions will also be investigated.

The chapter will then investigate the single particle dynamics of the glassy film by calculating the probability of the logarithm of single particle displacements for particles that start in the bulk region of the film and for those particles that start on the surface of the film. The aim of this section will be to compare the dynamics of the two regions of the film to elucidate the underlying behavior.

The final chapter will provide the conclusions made upon completion of the studies of both systems. It will also identify directions that future studies could use as a basis for investigation.

Chapter 2

Supercooled Water Confined in Hydrophilic Silica Nanopores: Background, Methods and Structure

This chapter is based on the first paper [18] I completed in Professor Ladanyi's group. This paper was entitled "Self-intermediate scattering function analysis of supercooled water confined in hydrophillic silica nanopores" and was authored by Kuon, Milischuk, Ladanyi, and Flenner. I was the first author on this paper for modeling and analyzing the system that appears in the paper.

2.1 Background

Nano-confinement of water has biological and industrial applications, and so it is important to understand its effect on water. From a chemical and physical perspective, the dynamics of supercooled nano-confined water is of fundamental interest [19]. If the confining geometry is such that it restricts the formation of the crystalline phase, it is possible to supercool water below the homogeneous nucleation temperature [20, 21]. Thus, nano-confinement offers a method of studying the dynamics of amorphous water at a temperature that is not possible for water in the bulk. However, due to the influence of the confining geometry and the water-surface interactions, the structure and dynamics of the water may be influenced by the confinement [22].

If water's confining geometry is that of the approximately cylindrical nano-pores of MCM-41, the water seems to be less influenced by the presence of the confining wall than with other materials [19, 23]. Thus, confining water within MCM-41 is suitable for studying the dynamics of supercooled water, and many experimental and simulational studies of this system have been performed at various pore radii [24–27, 29–31, 33–35]. It has been shown that, in general, the translational and rotational dynamics for nano-confined water slow down relative to the bulk at a given temperature [22]. The temperature dependence of the relaxation time of nano-confined water has also received much attention due to an apparent fragile-to-strong crossover transition [28].

Anisotropic dynamics within the pore however, make interpreting experimental results complicated [26, 27] .

Quasi-elastic neutron scattering (QENS) is a tool frequently used to examine the dynamics of water confined in MCM-41 nanopores [28–31, 33, 35]. It is generally assumed in analyzing QENS results that the signal is a product of translational, rotational, and vibrational components [36]. To further simplify analysis, it is also frequently assumed that the vibrational component is too fast to be resolved using QENS [37], and so it is not included in the analysis. As a result, several different approximations have been developed for analyzing the rotational and translational contributions to the QENS signal [36]. A quantity that is related to the dynamic structure factor obtained from QENS studies, the self-intermediate scattering function (SISF), can be calculated by molecular dynamics simulations to examine the accuracy of these approximations. How the anisotropic dynamics change the SISF can also be examined by molecular dynamics simulations.

Milischuk, Krewald and Ladanyi [27] examined the time and wavevector $\mathbf{Q}$ dependence of the SISF, $F_S(\mathbf{Q}, t)$, of the water hydrogens for water confined in model MCM-41 nanopores of various radii at 300 K to aid in the interpretation of QENS studies. In this study, they examined the dependence of the SISF on the momentum transfer $\mathbf{Q}$ and the pore diameter. How the SISF was influenced by the water molecules next to the silica surface, and the extent of the rotational-translational coupling in the SISF was also examined. Their conclusions stated that there was a strong dependence of the SISF on the pore size due to the decreased mobility next to the silica surface. They also concluded that the relaxation time of the SISF depends on the direction of $\mathbf{Q}$.

For the interpretation of QENS signals in the supercooled regime to be consistent, the approximations that are used to analyze the data need to be weakly temperature dependent, i.e., the approximations should accurately represent the data at all temperatures.. In this work we analyze the temperature dependence of the SISF for water hydrogens for the different pore sizes. The temperature range that we use spans 300 K to 210 K, which is in the midly supercooled regime for the SPC/E model of water. This is done for pore sizes of 40, 30, and 20 Å. The temperature dependence is also investigated for the anisotropic dynamics and the rotational-translational coupling.

We conclude that the rotational-translational coupling increases slightly with decreasing temperatures and that the dynamics, while displaying a large slow down, becoming only slightly more anisotropic.

This chapter is organized in the following manner. In Sec. 2.2, the molecular models and simulation methods that were used in the study are described. Included in this is a description of the procedure used to generate and hydrate the nanopores. Some difficulties that arose in the pore hydration process are also explained, as it was discovered that the process was taking a large amount of time to reach equilibrium. In sec. 2.3, we analyze the structure of the liquid using several methods. We examine the water density as a function of radial distance and how it is affected by the pore size and the temperature decrease. We also perform this analysis for two other important structural properties of water: the angular probabilities and the tetrahedral order parameter. The angular probabilities are determined with respect to the pore surface normal.

In the final section, section 2.4, we examine the mean squared displacements (MSDs) of the water molecules confined to the pores. We examine the MSDs in two directions: the axial (z) direction, and the radial (r) direction. We also investigate how the MSDs behave as they vary with pore size and temperature.

2.2 Methods

2.2.1 Pore Construction

Supercooled water was simulated using the simple point charge/extended (SPC/E) model of water, and the procedure used follows earlier studies [26, 27]. We studied three pore radii: 40, 30, and 20 Å..

The pores were generated using the procedure developed by Gulmen and Thompson [38]. In this procedure, a resist is created and is modeled as a set of repulsive beads positioned in an orthorhombic box in the shape of a cylinder of the desired radius. For clarity, the cylinder is created by placing the repulsive beads uniformly on a set of circles of radius r_{BE}. The number of beads are $N_{BE} = (z) \times (xy) = (\# \, \text{stacks}) \times (\# \, \text{beads per stack})$. The circles were stacked on

top of one another with a separation of 2.5 Å. A given number of SiO_2 groups are then placed in the box around the arrangement of the repulsive beads. The diameter of each pore, the number of SiO_2 molecules in each pore, and the values of r_{BE}, are given in Table 2.1

Table 2.1: Parameters used in the construction of the silica nanopores

d (Å)	# SiO_2	N_{BE}	$N_{BE} = (z) \times (xy)$	r_{BE}/Å
20	2932	56	7×8	3.0
30	2604	120	10×12	8.0
40	2121	256	16×16	13.5

The SiO_2 groups were arranged within the box according to the β-crystoballite structure. This structure is shown in 2.1. The Si and O atoms interacted with the repulsive beads as a C_{12}/r^{12} repulsion. The parameter C_{12} was chosen such that, upon equilibration of the system, interactions between the pore atoms on the surface and the repulsive beads were less than k_BT with $T = 300K$. This was done to minimize the affect of the beads' removal on the pore atoms. In this portion of the construction, the potential for the SiO_2 molecules is given by,

$$u(r) = \frac{q_\alpha q_\beta}{r} + A \exp(-br) - \frac{c}{r^6}.$$

(2.1)

This potential is called the van Beest-Kramer-vanSanten potential [32].

2.2.2 Pore Hydration

Once the pores were created, they were hydrated using two-box Gibbs ensemble Monte Carlo simulations using the TOWHEE simulation software [41–43]. The first box contained the empty pore to be filled. The second box contained water at a temperature of 300 K and a pressure of 4 kPa. The pressure was chosen to be slightly higher than the 3.6 kPa vapor pressure of SPC/E water at 300 K. During the simulation, the volume of the first box was kept constant, while the volume of the second box was allowed to fluctuate. The number of water molecules in both boxes remained
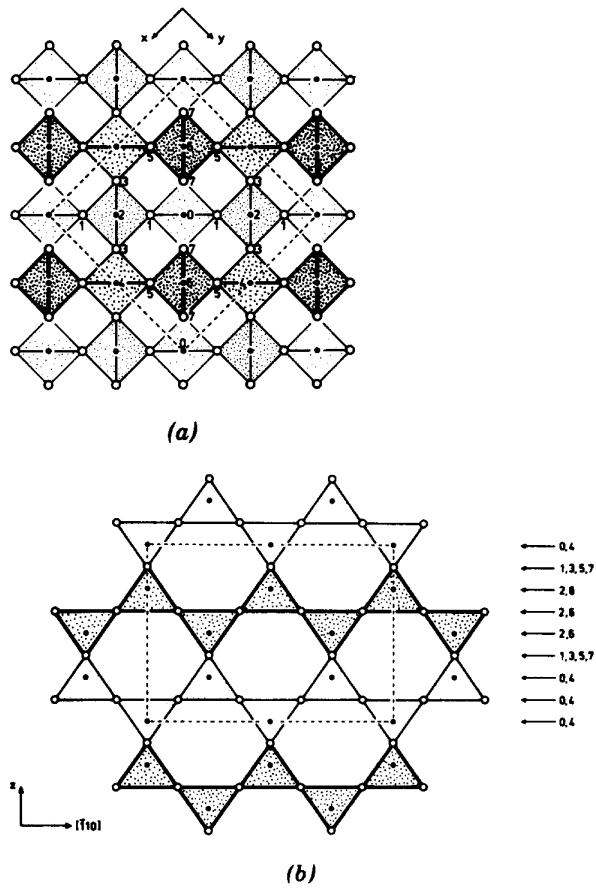
Figure 2.1: The ideal C9 cubic structure of β-crystobalite. (a) shows the projection on (001) and (b) shows the projection (110). The small filled circles are Si-atoms and the large, open circles are O-atoms (reproduced from Hatch 1991).

constant, but molecules could be deleted from one box and placed into the other. Translational, rotational, molecule insertion, and molecule deletion moves were performed on the water molecules until a plateau was observed in the number of water molecules within the box containing the pore. After approximately 15,000 Monte Carlo cycles, where a move is attempted on every molecule, a plateau was observed. Once the Monte Carlo simulations were complete, all water molecules in the first box outside of $R + 5$ Å were removed from the box, where R is the radius of the pore. These water molecules resided within voids in the silica matrix and their placement would not be physical due these voids having no entrance or exit. The final configurations were then used as initial configurations in molecular dynamics simulations.

The method described above gives a density of water molecules in the pore that is close to experimental measurements and is close to the density used in previous studies [22, 34]. Despite this, we examined the procedure to determine the sensitivity of the results on variations in the parameter used. Although the procedure produced consistent results, we found that the water molecules in the second box had condensed into small clusters and that the number of water molecules within the pore continued to increase despite a large simulation time, indicating that the water box/filled pore system was not in equilibrium.
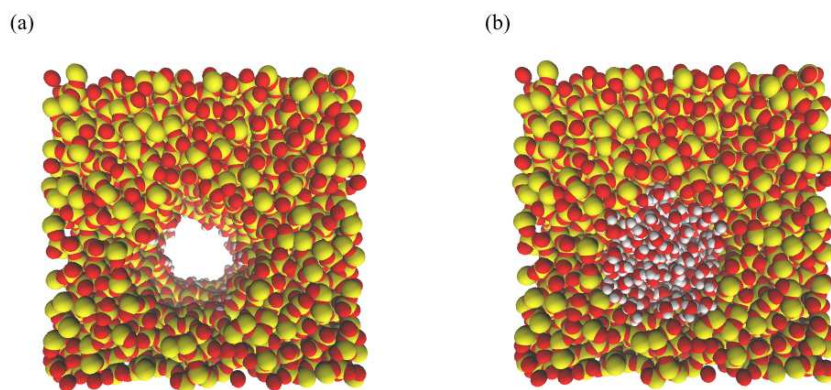
Figure 2.2: Renderings of: (a), the empty 20 Å pore, and (b), a hydrated 20 Å pore

Figure 2.2 and figure 2.3 show the pore box and water box, respectively. In both figures, (a) shows the state of the system at the start of the Monte Carlo simulation, while (b) shows the state
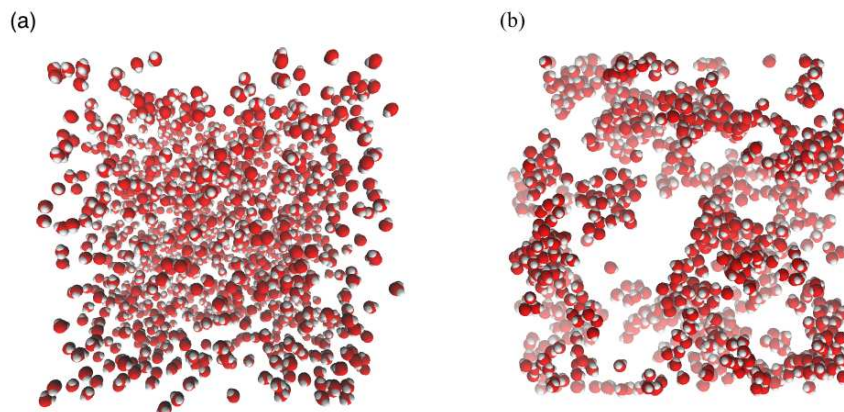
Figure 2.3: Renderings of: (a), the water-filled second box corresponding to the empty 20 Å pore, and (b), the water-filled second box. These boxes correspond to the above figure showing the empty and hydrated 20 Å pore.

of the system when the pore is approaching full hydration. The pore size is 20 Å. In figure 2.3 it can be clearly seen that the water molecules are distributed relatively uniformly throughout the box at the beginning of the simulation. However, when the pore is almost hydrated, (b) shows that the molecule have indeed condensed into small clusters. The presence of these clusters seems to hinder the system from reaching equilibrium at a reasonable rate and instead the amount of waters within the pore slowly increases and it is unclear how long this process would take.

In light of this, we attempted to hydrate the pore with the second box having water equilibrated at 300 K and 4 kPa, but the first box contained a previously hydrated pore [44–46]. The Monte Carlo simulations were run as previously described. In this case, it was found that the number of molecules within the pore decreased slightly. However, this decrease occurred at a rate of approximately 15 molecules per 35,000 Monte Carlo cycles. Again, equilibrium was approached very slowly.

An attempt was also made to hydrate the pore with the second box containing water at a temperature of 300 K and at ambient pressure (101 kPa). Again, the first box contained an already hydrated pore. In this case, the number of molecules in the pore decreased as in the previous analysis, but at a much faster rate. However, it was again unclear how long the Monte Carlo simulations would need to be run in order to reach equilibrium.

Table 2.2: Potential parameters for the atomic species used in this study

Interaction Site	q/e	ϵ (kJ/mol)	σ ()
O_w	-0.8476	0.650	3.166
H_w	0.4238	...	...
Si	1.28	...	...
O_{Si}	-0.64	1.912	2.700
O_{OH}	-0.74	1.912	3.000
H_{OH}	0.42	...	...

From these simulations, we conclude that the Monte Carlo simulation time needed to hydrate the pore to equilibrium would take a prohibitively long time. It is suggested that further work be undertaken to examine the dynamics of the system to determine if small changes in the hydration procedure significantly change the dynamics of the system. In order to make contact with previous work, we used previously hydrated pores using the original method described above.

2.2.3 Model and Simulation Details

The simulations performed in this study were performed at temperatures of 250 K, 240 K, 230 K, 220 K, and 210 K using the NVT ensemble with a Nosè-Hoover thermostat and a relaxation constant of 50 ps. The simulations were run using the DL_POLY_2 simulation package. The initial condition for the next lowest temperature was an equilibrium condition for the next highest temperature. The system was equilibrated for at least 10 ns and at least four production runs of length 10 ns were run. These lengths of time were chosen to be approximately 100 times the relaxation time of the system.

The interaction potential between particles i and j was of Lennard-Jones plus Coulomb type, and is defined as

$$U(r_{ij}) = 4\epsilon_{ij}\left[\left(\frac{\sigma_{ij}}{r_{ij}}\right)^{12} - \left(\frac{\sigma_{ij}}{r_{ij}}\right)^{6}\right] + \frac{q_iq_j}{4\pi\epsilon r_{ij}}. \tag{2.2}$$

Lorenz-Berthelot combining rules were used for the LJ parameters [48], and are defined as

$$\epsilon_{ij} = \sqrt{\epsilon_i\epsilon_j} \tag{2.3}$$

$$\sigma_{ij} = \frac{\sigma_i + \sigma_j}{2}. \tag{2.4}$$

The simple point-charge/extended (SPC/E) model [49] was used to model the water molecules, with the LJ parameters given by Bròdka and Zerda [52]. The partial charges were given by Gulmen and Thompson [53]. These parameters are given in Table 2.2, where atoms without Lennard-Jones sites are marked with by ellipses.

2.3 Water Structure

How the confinement, pore size, and temperature affect the structure of the water will be explored in this section. Several structural quantities will be analyzed in this section, including the radial density profile; the probability distribution of the water molecules' orientation relative to the pore surface; the radial distribution function corrected for exclusion effects from the presence of the pore, and the tetrahedral order parameter.

2.3.1 Radial Density Profile

This subsection will study the radial density profile. Previous simulations have demonstrated a variation in the density profile near the pore surface. The water dynamics can be influenced by both the pore surface and the variation of the density profile. We will be interested in how the radial density profile varies with temperature and pore size.

The radial density profile is defined as

$$n_W(\rho) = \sum_{i=1}^{N_W} m_i \left\langle \delta(\mathbf{r} - \mathbf{r}_i^{CM}) \right\rangle, \tag{2.5}$$

where $\mathbf{r}_i^{CM}$ is the water molecule center of mass, m_i is the mass of the water molecules, N_W is the number of water molecules, and $\rho^2 = x^2 + y^2$ is the radial distance from the center of the pore.

Figure 2.4 shows the radial density profile for waters in all three pore sizes and at four temperatures. Near the center of the pore, the radial density profile is uniform and approximately constant. The density in this region has a value of ~ 0.9 g/cc. The density value in this region is consistent
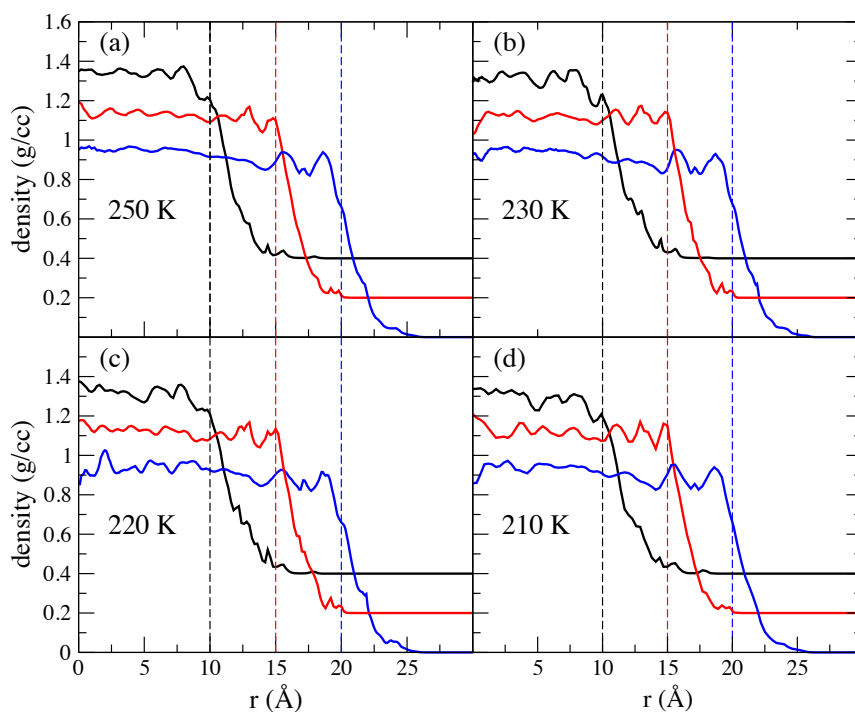
Figure 2.4: Radial density profile of the center of mass of the water molecules confined in the 40 Å pore (black line), the 30 Å pore (red line), and the 20 Å pore (blue line) for (a) $T = 250$K, (b) 230K, (c) 220K, and (d) 210K. The dashed lines indicated the radius of the pore. The 30 Å pore is offset by 0.2 g/cc and 20 Å pore is offset by 0.4 g/cc.

with previous simulations of 40 Å diameter pores. There are one to two peaks present near the pore wall. This is indicative of non-uniform water structure next to the pore wall. Close to the pore wall, the density rapidly decays to zero, but there are a non-zero number of particles outside of the defined pore radius. This is due to the roughness of the silica matrix.

Given the behavior of the radial density profile, the pore may then be divided into two regions: the core region and the shell region. The core region is defined as the region in the center of the pore wherein the density is approximately constant and uniform. For a pore of diameter d, the core region is defined to be $0 \leq \rho < d/2 - 6$ Å and the shell region to be $d/2 - 6$ Å $\leq \rho$. This definition is used to remain consistent with previous studies of the system [27]. It may be more appropriate due to the curvature of the interface, however, to compare the core regions of the different pore sizes. The percentages of the water molecules in the core region of the 40 Å, 30 Å, and 20 Å pores are 50.2%, 29.1%, and 11.4% respectively.

2.3.2 Angular Probabilities

Since water molecules are not spherical, how the molecules are oriented with respect to the pore surface can give an understanding as to how the molecules are affected by the presence of the pore wall. To quantify this, we calculated the probability that the average dot product of the inward-facing unit normal vector of the pore surface with the dipole vector of the water molecule has a value of $\cos \theta$. In other words,

$$\hat{\mathbf{u}} \cdot \hat{\mathbf{n}} = \cos \theta, \tag{2.6}$$

where $\hat{\mathbf{u}}$ is the unit vector along the water molecule's electric dipole moment.

Figure 2.5 shows the probability that this dot product has a value $\cos \theta$ at (a) 300 K, (b) 250 K, (c) 230 K, and (d) 210 K for water molecules that are within the core region (blue) and the shell region (red). These probabilities are calculated for water molecules within the 40 Å pore. The other pore sizes show similar behavior at these temperatures.

The probability for water molecules in the core region to have a value $\cos \theta$ is approximately uniform at all temperatures. This is expected given that molecules in this region are far enough

43
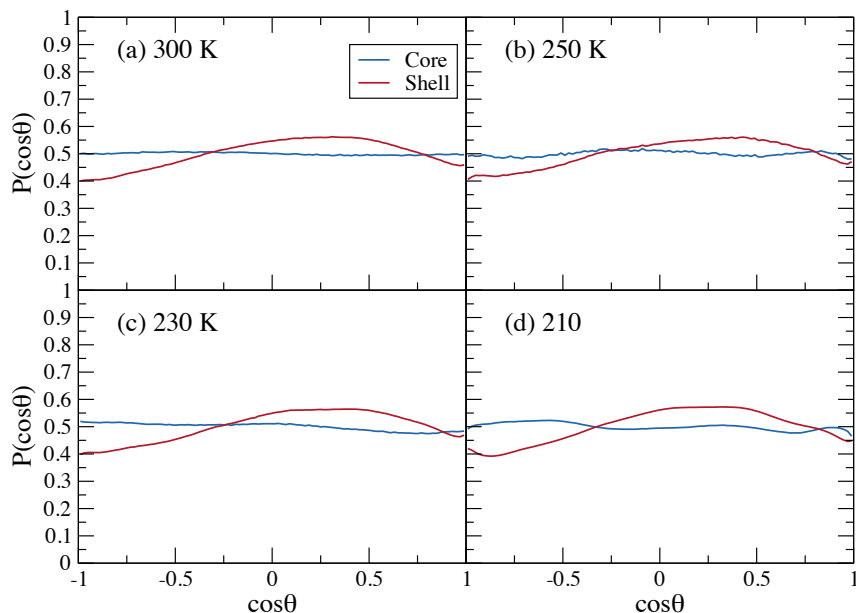
Figure 2.5: Probability that the dipole vector of a water molecule has an orientation of $\cos\theta$ with respect to the pore surface normal. The pore size is 40 Å. Panel (a) has a temperature of 300 K, (b) is 250 K, (c) is 230 K, (d) is 210 K

away from the pore surface that the surface has little affect on their orientation. Thus there is no preferential angle of the unit dipole moment vector with respect to the pore wall. The shell region, however, has a peak at a value of $\cos\theta \approx 0.3$ which corresponds to a θ value of $72.54°$. This implies that molecules in the shell region tend to align themselves such that the vector along the OH-bond is parallel to the pore wall. This behavior is seen at all temperatures, and does not seem to become more or less pronounced at lower or higher temperatures. Thus, we conclude that water molecules within the core region have an orientational structure that is similar to bulk water, and thus are affected very little by the presence of the nanopore wall.

2.3.3 Tetrahedral Order Parameter

Another structural quantity of importance, particularly for water, is the degree to which water molecules and their nearest neighbors form a tetrahedral network. The tetrahedral order is important due to the geometry of ice being a tetrahedron formed between the oxygen atoms of water

molecules. As this is a study of supercooled water, the formation of ice within the pore would be detrimental to the results of the study.

The tetrahedral parameter is defined as,

$$q = 1 - \frac{3}{8}\sum_{j=1}^{3}\sum_{k=j+1}^{4}\left(\cos\psi_{jk} + \frac{1}{3}\right)^2, \tag{2.7}$$

where ψ_{jk} is the angle formed by the vectors that point from a given water molecule to its nearest neighbors j and k (≤ 4) [57]. Since for a perfect tetrahedral network, $\cos\psi_{jk} = -\frac{1}{3}$, the value of q for a perfect tetrahedral network is one. Thus, if all water within the pore had crystallized into a tetrahedral structure, the average value of the tetrahedral order parameter would be very close to one.
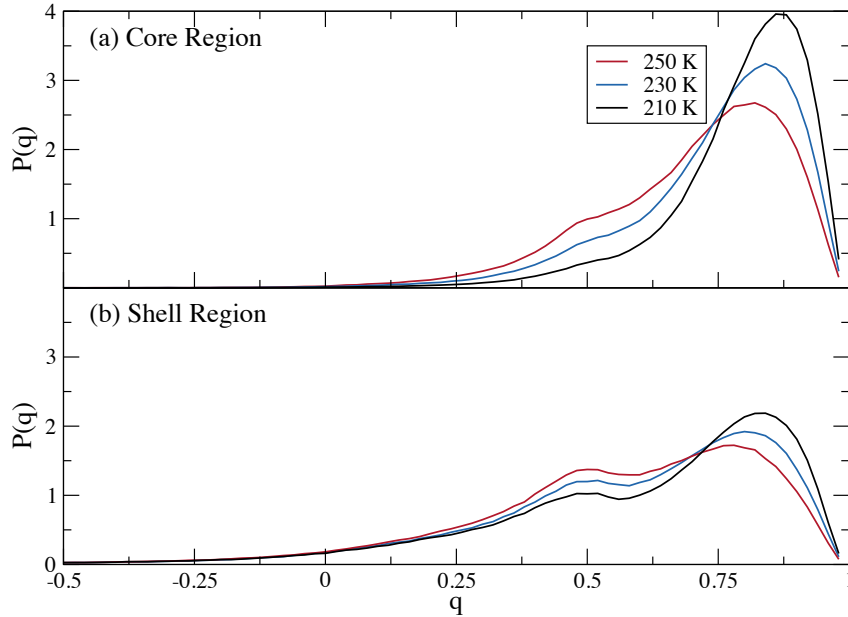
Figure 2.6: Distribution of the tetrahedral order parameter at temperatures of 250 K, 230 K, and 210 K for (a) the core region and (b) the shell region. The pore size is 40 Å.

Figure 2.6 shows the tetrahedral order parameter at temperatures of 250 K, 230 K, and 210 K in the 40 Å pore. Only one pore size is shown due to the other two pore sizes having very

similar behavior. Panel (a) shows the parameter for molecules within the core region of the pore, and panel (b) shows the parameter for molecules within the shell region. The curves for both regions have two peaks, with the first peak being more pronounced within the shell region. The first peak occurs at a value of $q \approx 0.5$, and this value does not change as the temperature is lowered. This value corresponds to a water molecule whose nearest neighbors have an average ψ_{jk} value of $82.06°$. We conclude that the first peak is more pronounced within the shell region due to the water interactions with pore wall. As the temperature is lowered , the first peak lowers in height and is almost nonexistent at 210 K for water molecules in the core region.

The second peak moves to the right and grows in height as the temperature is lowered. The second peak is also much more pronounced within the core region than in the shell region. The fact that the second peak is moving closer to a q-value of one implies that the water molecules in both regions have a more tetrahedral network. This is expected due to the hydrogen bonds formed between water molecules having a larger affect on the water structure at lower temperatures. However, neither region has an average q-value close to one. Thus, we can conclude that the water contained in the nanopore has not frozen, but is moving toward having a more tetrahedral network.

2.4   Water Mean Squared Displacement

In this section, we will discuss the dependence on temperature of the water molecules' mean-squared displacement. In QENS, the dynamics are examined on a length scale proportional to the inverse of the wavevector, **Q**. Thus, a small value of **Q** corresponds to a large length scale, whereas a large value of **Q** corresponds to a small length scale. The water mean-squared displacement can be examined to determine the dynamic behavior of the water molecules at long times and large displacements. We calculate mean-squared displacements (MSD) for the water center of masses in both the radial (ρ) direction and the axial (z) direction. This is due to the displacements of the water molecules being hindered in the (ρ)-direction.

The axial MSD is not hindered by the pore wall, and so it is linear at long times. The expression for the axial MSD is

$$\langle \Delta z^2(t) \rangle = \langle (z(t) - z(0))^2 \rangle = 2D_z t. \tag{2.8}$$

The MSD in the radial direction is hindered by the pore wall. If the pore is approximated as a smooth cylinder, then at long times the radial MSD will approach the square of the pore radius. For non-interacting particles in a smooth cylinder, the radial MSD may be solved for exactly using the diffusion equation in cylindrical coordinates. This was solved by Bròdka and gives for the MSD [52],

$$\langle (\boldsymbol{\rho}(t) - \boldsymbol{\rho}(0))^2 \rangle = R^2 \left[1 - \sum_{n=1}^{\infty} \frac{8}{x_{1n}'^2 (x_{1n}'^2 - 1)} e^{\frac{-x_{1n}'^2}{R^2} D_\rho t} \right]. \tag{2.9}$$

In this expression, the x_{1n} are the zeros of the derivative of the Bessel function $J_1(x)$, D_ρ is the radial diffusion coefficient, and R is the radius of the pore. However, the pore wall is rough and is only approximately a smooth cylinder.
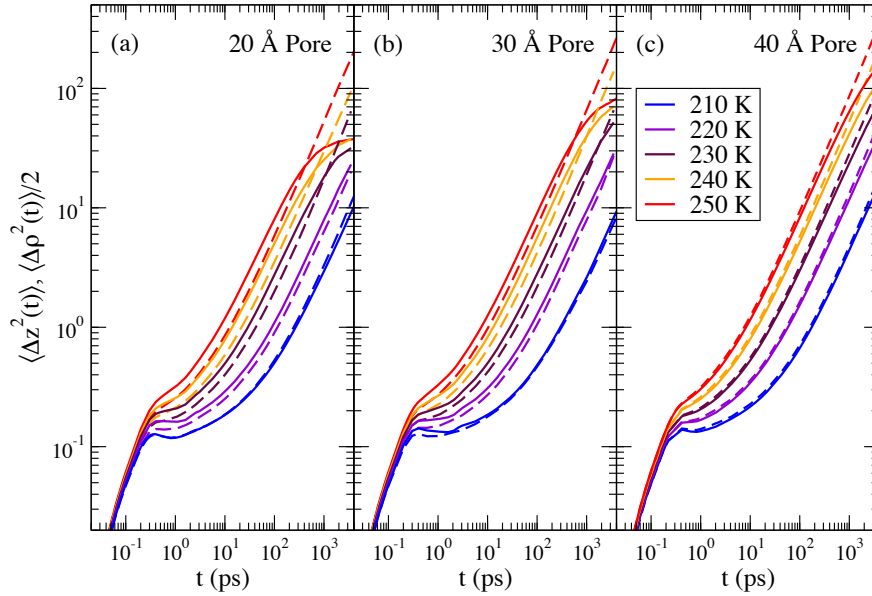
Figure 2.7: The axial (dashed lines) and radial (solid lines) MSDs for all the water molecules at all temperatures for (a) the 20 Å pore, (b) the 30 Å pore, and (c) the 40 Å pore. The saturation of the radial component at long times is visible at the higher temperatures.

Figure 2.7 shows the axial and $1/2$ the radial MSD (it is halved to compare the radial and axial MSDs) are for (a) the 20 Å pore, (b) the 30 Å pore, and (c) the 40 Å pore. These MSDs are shown

for all temperatures. At lower temperatures, a plateau can be seen emerging at intermediate times. This plateau is temperature-dependent and, while it persists for a longer time at lower temperatures, it occurs at a larger MSD at higher temperatures. While the radial and axial MSDs are similar in the ballistic time regime, they begin to deviate from one another at intermediate times, with the radial MSD being slightly larger than the axial in this time regime, particularly in the 20 Å and 30 Å pore. This occurs at all temperatures except for 210 K. After the plateau, both the radial and axial MSDs enter a regime wherein both are approximately linear. The radial MSD, however, at long times, approaches its asymptotic value discussed above while the axial MSD remains linear. We would like to note, however, that the asymptotic value of the radial MSD is slightly larger than the radius we assigned to the pore. This is due to the roughness of the pore matrix, and the pore itself not being perfectly cylindrical.

The 20 Å and 30 Å pores exhibit an appreciable slowing down of the radial MSD relative to the axial MSD at 250 K. However, as the temperature is lowered, this relative difference between the two components decreases, and is nearly zero at 210 K. We attribute this slowing behavior in the axial MSD to the rough pore walls. The roughness of the walls hinders particle motion more in the axial direction than in the radial direction. This does not explain, however, the nearly vanishing difference between the radial and axial MSDs at 210 K. The nearly vanishing difference suggests instead that there is a change in water dynamics at the lower temperatures. We recommend that future studies investigate water displacements next to the pore wall for this reason. There is a small difference between the short and intermediate times at all temperatures in the 40 Å pore.

Since we wish to examine the mobility of the water as a function of distance from the pore wall, we now examine the axial MSDs for particles that, at $t = 0$, begin in the core region of the pore or the shell region of the pore. The axial MSDs for these regions are shown in Figure 2.8. The dotted-dashed lines are MSDs for particles that began in the core region; the dashed lines show MSDs for particles that began in the shell region; and the solid lines show MSDs for all water molecules. At time t, the water molecules in the core and shell MSDs can be at any position within the pore. At short times, all three curves coincide, implying that the dynamics in both regions are
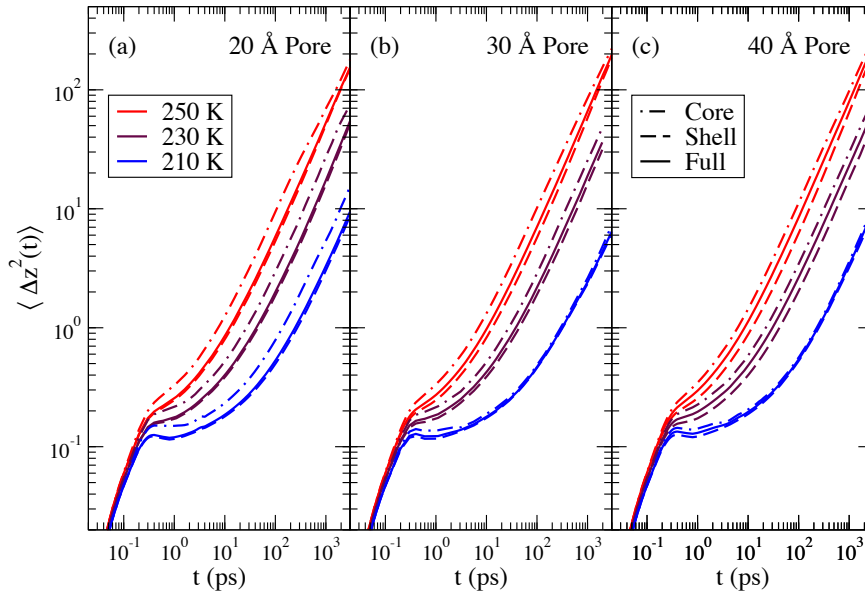
Figure 2.8: $\Delta z^2(t)$ for water molecules that start in the core (dot-dashed), in the shell (dashed), and for all the water molecules (solid) for (a) the 20 Å pore, (b) the 30 Å pore, and (c) the 40 Å pore. Temperatures of 250 K, 230 K, and 210 K are shown.

identical on these timescales. Thus, the effect of the water-substrate interaction is negligible at short times.

On the timescale of the simulations, water molecules that began within the core region are more mobile than those that start in the shell region. This occurs for all pore sizes and temperatures except for those in the 40 and 30 Å pores at 210 K. In these cases, the mobility is not dependent upon the starting position of the water molecules. Quasi-elastic neutron scattering (QENS) probes length scales proportional to $\mathbf{Q}^{-1}$, and the range of $\mathbf{Q}$ is between 0.2 Å^{-1} and 3.0 Å^{-1}. On the length scales probed by QENS, we find that the MSDs show that the dynamics of the water are heterogeneous.

Chapter 3

Supercooled Water Confined in Hydrophilic Silica Nanopores: The Self-Intermediate Scattering Functions

This chapter is based on the first paper [18] I completed in Professor Ladanyi's group. This paper was entitled "Self-intermediate scattering function analysis of supercooled water confined in hydrophillic silica nanopores" and was authored by Kuon, Milischuk, Ladanyi, and Flenner. I was the first author on this paper for modeling and analyzing the system that appears in the paper.

3.1   Introduction

In Quasi-Elastic Neutron Scattering (QENS), one measures the double differential cross-section of the atomic species in the system with respect to solid angle Ω and frequency ω. The frequency ω is related to the change in energy of the scattered neutron via the relation $E = \hbar\omega$. The full double differential cross-section is a sum of coherent and incoherent parts, and each atomic species within a system has a unique coherent and incoherent total scattering cross-section. Table 3.1 shows the

Table 3.1: Incoherent and Coherent Scattering Cross-Sections of Hydrogen and Oxygen Atoms

...	O	H
σ_{coh} (barns)	4.232(6)	1.7583(10)
σ_{inc} (barns)	0.000	80.27(6)

coherent and incoherent cross-sections of oxygen atoms and hydrogen atoms. As can be seen, hydrogen atoms have a large total incoherent cross-section that dwarfs the coherent contributions from both atomic species. Thus, the QENS signal for confined water can be assumed to be primar-

ily due to incoherent neutron scattering off of hydrogen atoms, and so all other terms can be taken to be negligible.

The incoherent double differential cross-section is directly proportional to the single particle dynamic structure factor, $S_S(\mathbf{Q}, \omega)$ via the following relation,

$$\frac{d^2\sigma_{\text{inc}}}{d\Omega d\omega} = \frac{\sigma_{\text{inc}}}{4\pi} \frac{k_f}{k_i} S_S(\mathbf{Q}, \omega). \tag{3.1}$$

In this equation, k_i and k_f are the magnitudes of the initial and final momenta of the neutrons and $\mathbf{Q} = \mathbf{k}_f - \mathbf{k}_i$. The function $S_S(\mathbf{Q}, \omega)$ is unique to the sample and, therefore, is the quantity used to analyze the dynamics of the sample. However, in molecular simulation it is not possible to calculate $S_S(\mathbf{Q}, \omega)$ directly. Instead, the self-intermediate scattering function, $F_S(\mathbf{Q}, t)$, is calculated. This function is related to $S_S(\mathbf{Q}, \omega)$ via a frequency Fourier transform

$$S_S(\mathbf{Q}, \omega) = \frac{1}{2\pi} \int_{-\infty}^{\infty} F_S(\mathbf{Q}, t) e^{i\omega t} \, dt, \tag{3.2}$$

where

$$F_S(\mathbf{Q}, t) = \frac{1}{N_H} \sum_{j=1}^{N_H} \langle \exp\left[i\mathbf{Q} \cdot (\mathbf{r}_j(0) - \mathbf{r}_j(t))\right] \rangle. \tag{3.3}$$

In equation 3.3, N_H is the number of hydrogen atoms and the index j runs over all hydrogen atoms. We are summing only over the hydrogen atoms in equation 3.3 due to the dominance of the hydrogen atom's incoherent total scattering cross-section. Thus, calculating the self-intermediate scattering function allows molecular simulation to make contact with QENS studies.

The frequency range accessible by QENS cannot resolve vibrational motion within the OH-bonds of the water molecules, and thus a rigid model of water may be used in molecular simulations to lower the computation time of the simulations [37]. In a rigid water molecule, the position of the hydrogen atom may be written as,

$$\mathbf{r}_i = \mathbf{r}_i^{\text{CM}} + \mathbf{b}_i^n, \tag{3.4}$$

where $\mathbf{r}_i^{\mathrm{CM}}$ is the molecular center of mass and $\mathbf{b}_i^n$ is the vector pointing from the molecular center of mass to the nth hydrogen atom of the water molecule. Given that the SPC/E model of water is a rigid model, the vector $\mathbf{b}_i^n$ can only change through rotational motion. Thus, the self-intermediate scattering function becomes

$$
\begin{aligned}
F_S(\mathbf{Q}, t) &= \frac{1}{N_H} \sum_{j=1}^{N_H} \left\langle e^{[i\mathbf{Q}\cdot(\mathbf{r}_j(0)-\mathbf{r}_j(t))]} \right\rangle = \\
&\frac{1}{N_H} \sum_{j=1}^{N_W} \sum_{n=1}^{2} \left\langle e^{[i\mathbf{Q}\cdot(\mathbf{r}_j^{\mathrm{CM}}(0)-\mathbf{r}_j^{\mathrm{CM}}(t))]} e^{[i\mathbf{Q}\cdot(\mathbf{b}_j^n(0)-\mathbf{b}_j^n(t))]} \right\rangle.
\end{aligned}
\tag{3.5}
$$

The product approximation is frequently used to analyze data in QENS experiments. In this approximation, it is assumed that the rotational and translational motion of the molecules are decoupled. Hence, the self-intermediate scattering function may be expressed as a product of the rotational and translational components of the function, i.e. [36]

$$
F_S(\mathbf{Q}, t) \cong F_S^T(\mathbf{Q}, t) F_S^R(\mathbf{Q}, t).
\tag{3.6}
$$

The translational and rotational components are defined as follows,

$$
F_S^T(\mathbf{Q}, t) = \frac{1}{N_W} \sum_{j=1}^{N_W} \left\langle e^{[i\mathbf{Q}\cdot(\mathbf{r}_j^{\mathrm{CM}}(0)-\mathbf{r}_j^{\mathrm{CM}}(t))]} \right\rangle,
\tag{3.7}
$$

and

$$
F_S^R(\mathbf{Q}, t) = \frac{1}{N_W N_H} \sum_{j=1}^{N_W} \sum_{n=1}^{2} \left\langle e^{[i\mathbf{Q}\cdot(\mathbf{b}_j^n(0)-\mathbf{b}_j^n(t))]} \right\rangle.
\tag{3.8}
$$

The momentum transfer, $\mathbf{Q}$, is examined in the axial direction and the radial direction; the values of $\mathbf{Q}$ are chosen to lie within the range accessible to QENS experiments. This range is defined in chapter 2, and ranges from 0.2 Å^{-1} to 3.0 Å^{-1}.

3.2 Self-Intermediate Scattering Functions

The temperature dependence of the total self-intermediate scattering functions will be examined in this section. It was shown in previous works that $F_S(\mathbf{Q}, t)$ is dependent on the direction of $\mathbf{Q}$ and that the relaxation time is inversely proportional to the pore size [33]. The dynamics of the water molecules exhibited an overall slowing down with smaller pore size and there were an increased fraction of water molecules within the shell region in the smaller pores.

In Figure 3.1 we show the total self-intermediate scattering function in all three pore sizes for four values of $Q = |\mathbf{Q}|$. We show all five temperatures for each Q-value. Results are shown for the axial direction (solid) and the radial direction, (dashed). It is expected that the average of $F_S(\mathbf{Q}, t)$ over $\mathbf{Q}$ would lie between $F_S(Q_z, t)$ and $F_S(Q_{xy}, t)$. Future work should examine this expectation. After an initial decay at small times, representative of ballistic motion, a plateau develops at intermediate times. This plateau is indicative of the water molecules being trapped in a cage of their nearest neighbors. With decreasing temperature, the water molecules take an increasingly long amount of time to escape from their cages. Thus, the plateau height persists for a longer time and occurs at a higher value as the temperature is lowered. The decay is non-exponential in all cases at the end of the plateau; however, this decay is very slow and does not fit a stretched exponential well. When $\mathbf{Q}$ is perpendicular to the pore wall, $F_S(\mathbf{Q}, t)$ decays to a constant value due to the bound of the pore wall and the elastic incoherent structure factor in the rotational motion. We now will look at the limits and general shape of the translational and rotational self-intermediate scattering functions.

3.2.1 Rotational and Translational Self-Intermediate Scattering Functions

This section will examine the rotational scattering function, $F_S^R(\mathbf{Q}, t)$, as defined in equation 3.8. First, we will examine how the function varies with Q-value, temperature and pore size; and identify major characteristics of the function. Then, we will examine the applicability of the Rayleigh expansion for determining the behavior of $F_S^R(\mathbf{Q}, t)$ and the rotational correlation functions that calculate the Rayleigh expansion.
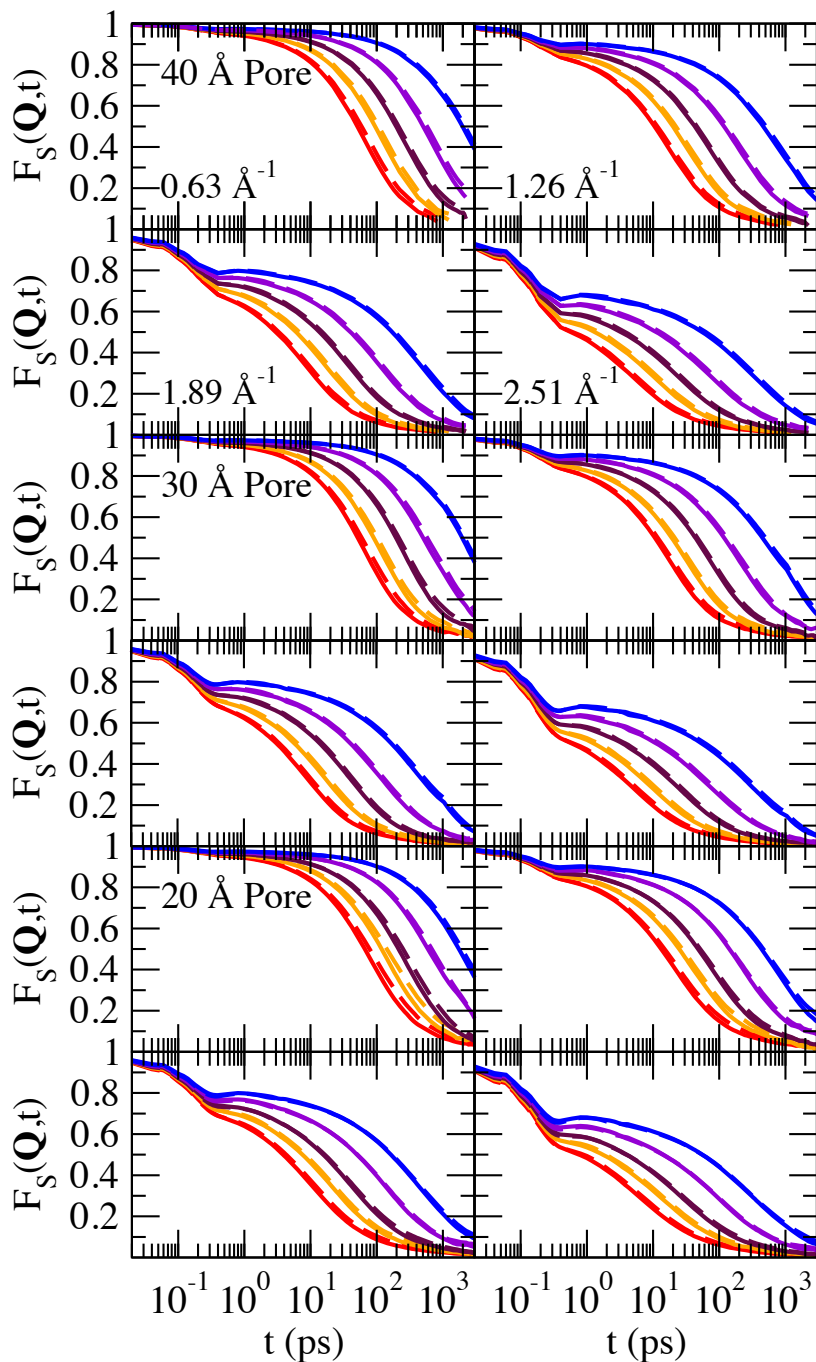
Figure 3.1: The total self-intermediate scattering functions for all three pores at the four Q-values used in this study. The dashed line results are for **Q** in the radial direction while the solid lines are for **Q** in the axial direction. The temperatures are 250 K (red lines), 240 K (orange lines), 230 K (maroon lines), 220 K (purple lines), and 210 K (blue lines).
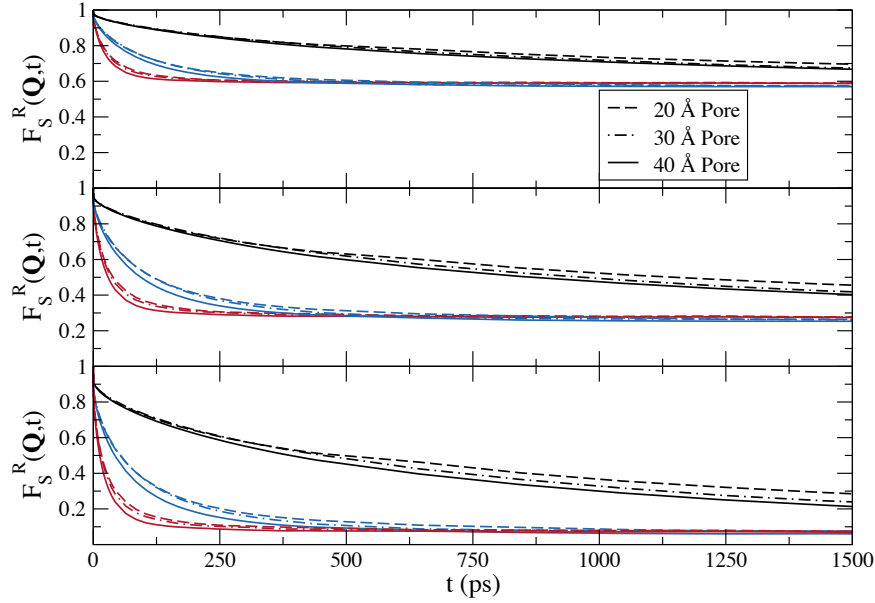
Figure 3.2: The rotational self-intermediate scattering functions for all three pores with Q-values of (a) 1.26 Å^{-1}, (b) 1.89 Å^{-1} and (c) 2.51 Å^{-1}. . The temperatures are 250 K (red lines), 230 K (blue lines), and 210 K (black lines).

Using the definition given in equation 3.8, we calculated the rotational SISF for pore water molecules. The results are shown in Figure 3.2. The figure has three plots: (a) having a Q-value of 1.26 Å^{-1}, (b) having a Q-value of 1.89 Å^{-1}, and (c) having a Q-value of 2.51 Å^{-1}. Each plot has curves for all three pore sizes, and is calculated at temperatures of 250 K, 230 K, and 210 K.

Figure 3.3 shows the temperature dependence of $F_S^R(\mathbf{Q}, t)$ in all three pores at a Q-value of 1.89 Å^{-1}. The temperatures shown are 250 K, 230 K, and 210 K. We chose the wavevector to be along the axial direction (dashed lines) and the radial direction (dashed-dotted lines). There is no significant difference between the two directions. However the radial direction has a slightly longer decay time.

If a fluid is isotropic, $F_S^R(\mathbf{Q}, t)$ may be expressed in terms of the Rayleigh expansion [56].

$$F_S^R(\mathbf{Q}, t) = [j_0(Qb)]^2 + \sum_{l=1}^{\infty} (2l + 1) [j_l(Qb)]^2 C_l(t), \qquad (3.9)$$

where
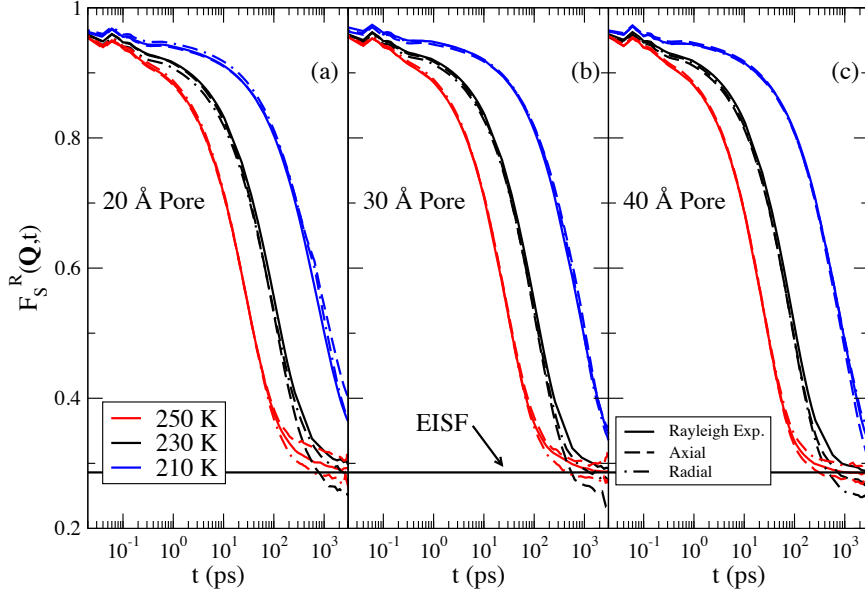
Figure 3.3: The rotational self-intermediate scattering functions, $F_S^R(\mathbf{Q}, t)$, for $\mathbf{Q}$ in the radial (dot-dashed) and axial (dashed) directions for $T = 250$ K (red), 230 K (black), and 210 K (blue) listed from left to right. Panel (a) shows results the 20 Å pore, (b) is the 30 Å pore, and (c) is the 40 Å pore. The Rayleigh expansion at each temperature is also shown in each panel as the solid line, and the EISF is shown as a horizontal black dashed line.

$$C_l(t) = \left\langle P_l[\hat{\mathbf{b}}(0) \cdot \hat{\mathbf{b}}(t)] \right\rangle = \langle P_l[\cos\theta(t)] \rangle, \qquad (3.10)$$

$P_l(x)$ are Legendre polynomials of order l, and $\hat{\mathbf{b}}$ are the unit vectors along $\mathbf{b}$. $\mathbf{b}$ is the vector point from the center of mass of the water molecule to one of the hydrogen atoms. Additional terms may be added to take into account anisotropy due to the confining wall of the pore [27]. In this work, we will only consider the Rayleigh expansion as this allows for the separation of the time-dependent and Q-dependent terms.

In Figure 3.4 we show the temperature dependence of the rotational correlation functions, $C_l(t)$, at $l = 1$, $l = 2$ and $l = 3$. These curves are shown for each pore size and temperature. At the highest temperatures, the decay of $C_l(t)$ is slower for the smaller pores, but this difference decreases as the temperature is lowered. The rotational correlation functions are not as influenced by pore size as are the total self-intermediate scattering functions. This is to be expected given the motion influenced by the pore wall is translational motion.
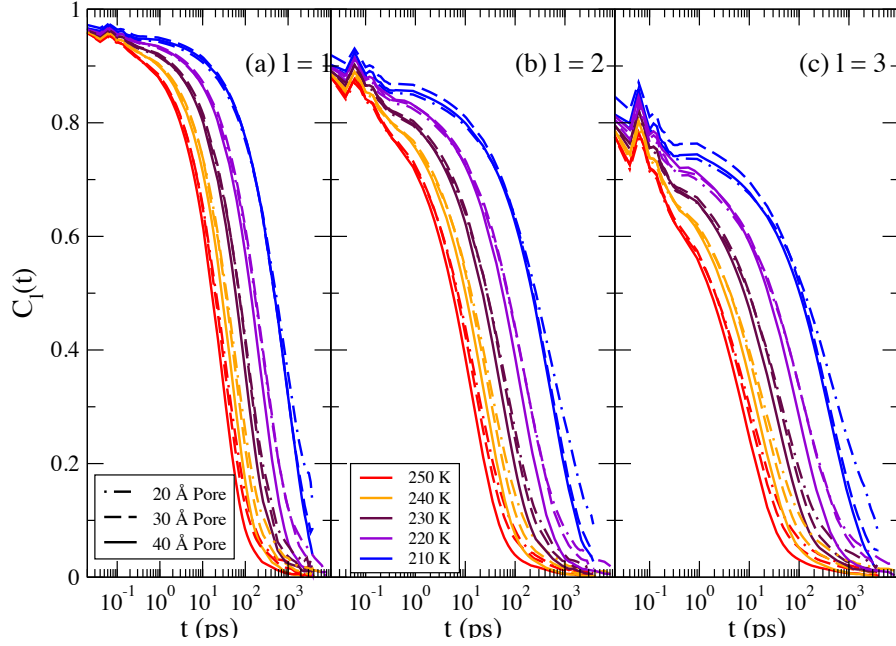
Figure 3.4: The rotational correlation function $C_l(t)$ for (a) $l = 1$, (b) $l = 2$, and (c) $l = 3$ for the 20 Å pore (dotted-dashed line), the 30 Å pore (dashed line), and the 20 Å pore (solid line), respectively, for each temperature.

In Figure 3.3 we show the accuracy of the Rayleigh expansion at a Q-value of 1.26 Å^{-1} for temperatures of 250 K, 230 K, and 210 K. Plot (a) shows the 20 Å pore, (b) shows the 30 Å pore, and (c) shows the 40 Å pore. The solid curves in Figure 3.3 show the Rayleigh expansion up to third order. The dashed lines are $F_S^R(\mathbf{Q}, t)$ with $\mathbf{Q}$ in the axial direction and the dashed-dotted lines are $\mathbf{Q}$ in the radial direction. The solid horizontal line is the Elastic Incoherent Structure Factor, which is defined as

$$\text{EISF} = F_S^R(\mathbf{Q}, t \to \infty) = [j_0(Qb)]^2. \tag{3.11}$$

The second equality is to note that the EISF was calculated using 3.9. The Rayleigh approximation is an excellent approximation for $F_S^R(\mathbf{Q}, t)$ at all temperatures and pore sizes. Thus, we can conclude that $F_S^R(\mathbf{Q}, t)$ is not as dramatically affected by the pore size as is $F_S(\mathbf{Q}, t)$, and the Rayleigh expansion is a good approximation despite the non-uniformity of the system.

Using the definition given in Equation 3.7, we calculated the translational self-intermediate scattering function, $F_S^T(\mathbf{Q}, t)$ for pore waters at all pore sizes and all temperatures. Figure 3.5
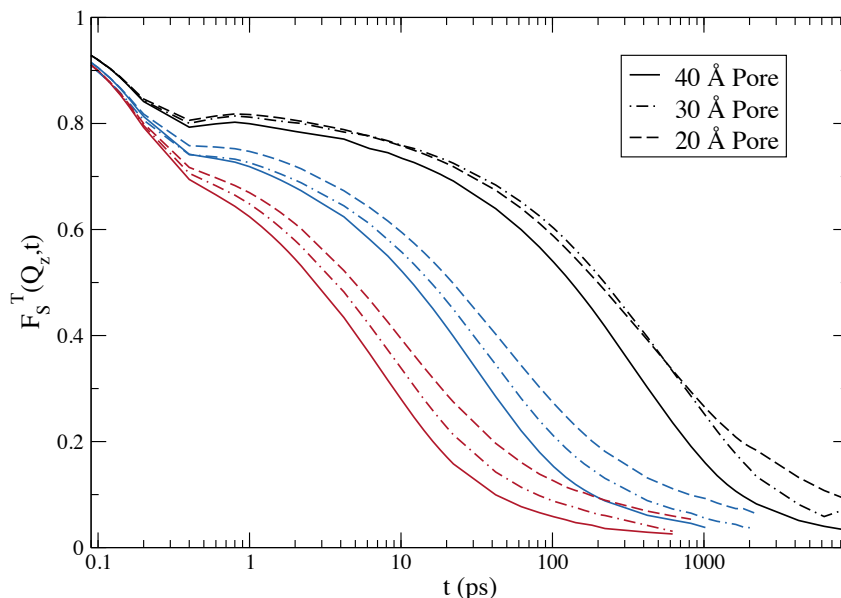
Figure 3.5: The translational self-intermediate scattering functions for all three pores with a Q-value of 1.89 Å^{-1}. The temperatures are 250 K (red lines), 230 K (blue lines), and 210 K (black lines).

shows the translational SISF for a Q-value of 1.89 Å^{-1} in all pore sizes and temperatures of 250 K, 230 K and 210 K. At all temperatures there is a much larger difference between the translational SISFs with respect to pore size as opposed to the rotational SISFs. This can be expected as the translational self-intermediate scattering functions decay over a much larger time scale than the rotational self-intermediate scattering functions. Thus, water molecules may move across the pore and be stopped by the side of the pore.

3.2.2 Relaxation Times of the Total Self-Intermediate Scattering Functions

In order to quantify the decay time of the total SISF, we define the alpha relaxation time $\tau_\alpha(\mathbf{Q})$ through $F_S(\mathbf{Q}, \tau_\alpha(\mathbf{Q})) = e^{-1}$. We note that $\tau_\alpha(\mathbf{Q})$ depends on the direction and magnitude of $\mathbf{Q}$. However, our results will show only $\mathbf{Q}$ in the axial direction. This is due to the scattering functions not fully decaying to zero in the radial direction, and the fact that $\tau_\alpha(Q_z)$ and $\tau_\alpha(Q_{xy})$ are approximately equal.

In figure 3.6 we show the relaxation time as a function of Q_z for each pore size and temperatures of 250 K, 230 K, and 210 K. There is at least a 1.5 order of magnitude slowdown for each Q-value.
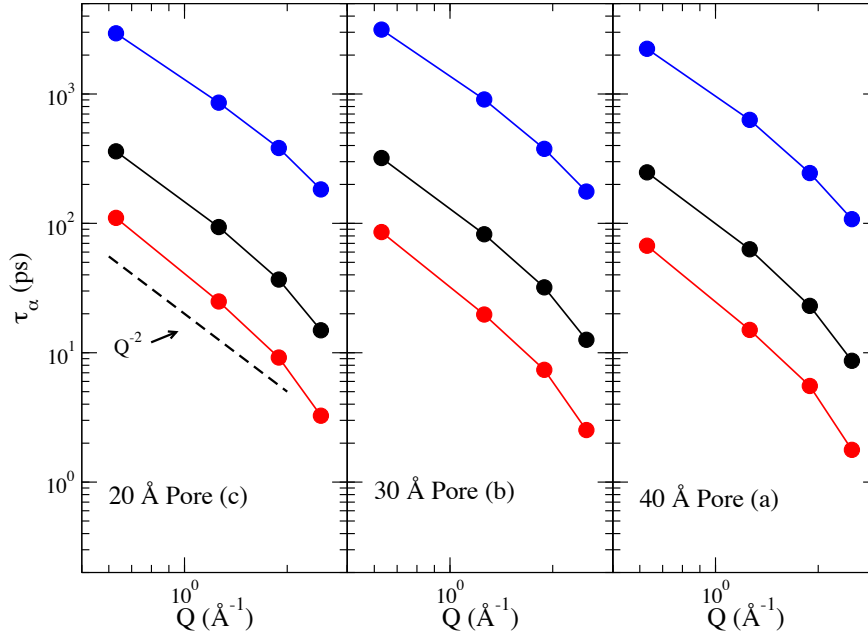
Figure 3.6: The relaxation time $\tau_\alpha(Q_z)$ calculated for (a) the 20 Å pore, (b) the 30 Å pore, and (c) the 40 Å pore for temperature of 250 K (blue), 230 K (black), and 210 K (red).

We show the Q_z^{-2} dependence for reference to the result for Fickian diffusion. Ultimately, the two smallest wavevectors are consistent with what is seen for Fickian diffusion. However, as Q_z is increased, the relaxation time decreases at a faster rate than that seen in Fickian diffusion. We also find that the relaxation time as a function of Q_{xy} is slightly larger than that of Q_z, but, within the error of the calculation, both directions have the same dependence on the magnitude of **Q**.

In Figure 3.7 we show the full temperature dependence of the relaxation time, τ_α at a Q-value of 1.89 Å^{-1} calculated for the total self-intermediate scattering function. For each pore we find that the relaxation time increases as the temperature decreases. Furthermore, except for the temperature of 210 K, the relaxation times are larger for smaller pore sizes. At 210 K, the 30 Å pore has a slower relaxation time than the 20 Å pore. We find that the same trend is satisfied for the inverse diffusion coefficient, but that the difference between the 20 and 30 Å pore at 210 K is not as pronounced.

The cause of this non-monotonic temperature dependence of the relaxation time and the inverse diffusion coefficient on the pore size is unknown. We investigated a few different hypotheses in an attempt to determine the cause. One hypothesis was that the slower relaxation times at 210 K in
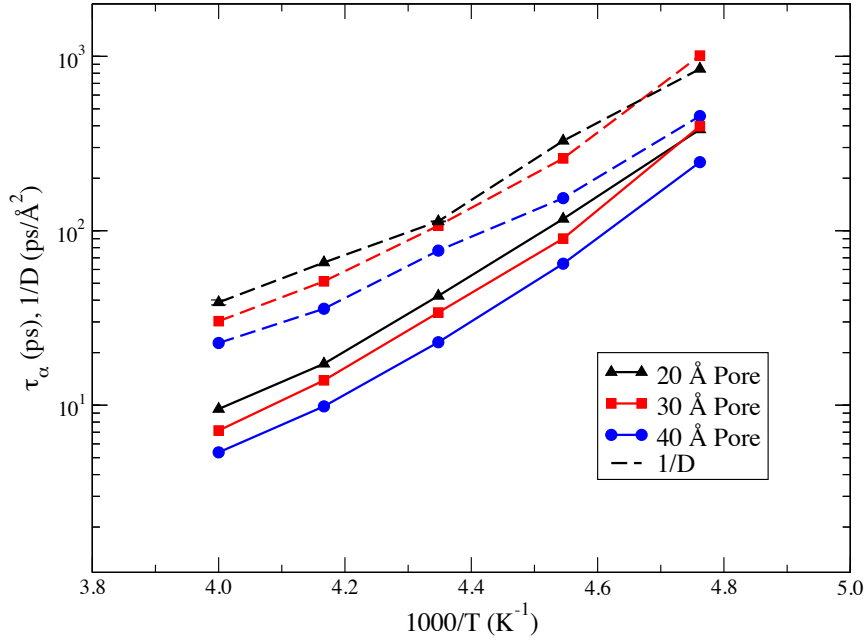
Figure 3.7: Temperature dependence of τ_α relaxation times (τ_α) in all pores at $Q = 1.89$ Å^{-1}. The temperature dependence of the inverse diffusion coefficient (1/D) in all pore sizes is also plotted.

the 20 and 30 Å pores was due to the curvature of the pore wall. Future studies should investigate this hypothesis. Another hypothesis was that freezing was occurring within the pores and that this was the cause of the phenomenon. We tested this by calculating the tetrahedral order parameter as shown in Chapter 2. As stated in chapter 2, we found no evidence for the presence of ice within any of the pore sizes, however, the difference in height between the 20 and 30 Å pores in the tetrahedral order parameter at 210 K was too small to come to any conclusions regarding the difference in dynamics.

3.2.3 Translational-Rotational Coupling

This section will examine the product approximation given in equation 3.6, and the translational-rotational coupling of the water's motion. As stated in the introduction, the product approximation is often used in QENS experiments. In previous works [27], it was suggested that the translational-rotational coupling was weak at 300 K, and we examine the temperature dependence of the coupling. We examine the pore size dependence of the connected scattering function, $F_S^C(\mathbf{Q}, t)$,

which is a measure of the accuracy of the product approximation and the amount of rotational-translational coupling.

To examine the accuracy of the product approximation, we examined the connected scattering function, which is defined as,

$$F_S^C(\mathbf{Q}, t) = F_S(\mathbf{Q}, t) - F_S^T(\mathbf{Q}, t) F_S^R(\mathbf{Q}, t), \tag{3.12}$$

where $F_S^T(\mathbf{Q}, t)$ and $F_S^R(\mathbf{Q}, t)$ are the translational and rotational scattering functions respectively.
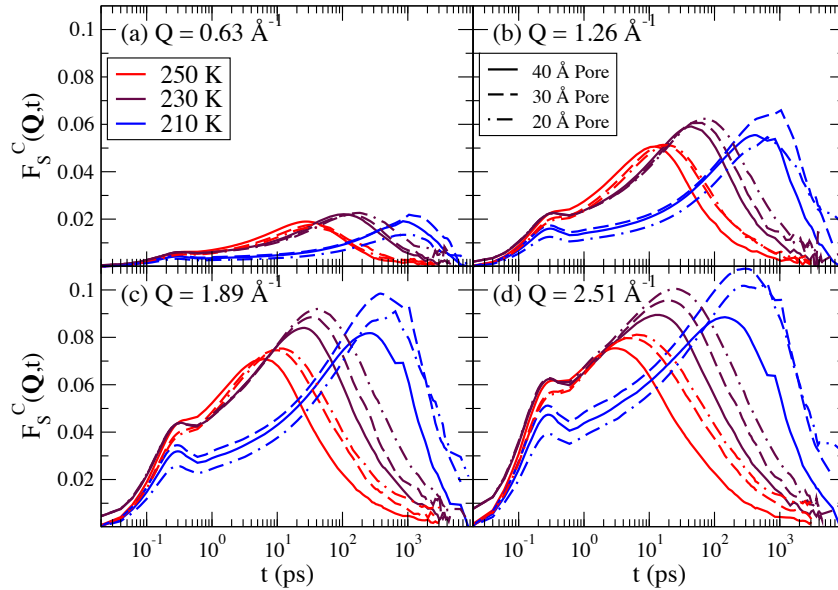
Figure 3.8: Connected portion of $F_S(\mathbf{Q}, t)$ for each pore, and temperatures of 250 K, 230 K, and 210 K. Plot (a) has a Q-value of 0.63 Å^{-1}, (b) 1.26 Å^{-1}, (c) 1.89 Å^{-1}, and (d) 2.51 Å^{-1}. The product approximation is more accurate for smaller wavevectors, but is weakly dependent on temperature and pore size.

The connected scattering functions are shown in Figure 3.8. Four plots are shown: plot (a) has a Q-value of 0.63 Å^{-1}, (b) 1.26 Å^{-1}, (c) 1.89 Å^{-1}, and (d) 2.51 Å^{-1}. In each of the four plots, $F_S^C(A, t)$ is plotted for all three pore sizes at temperatures of 250 K, 230 K and 210 K. There are two peaks visible in $F_S^C(A, t)$ at all temperatures, Q-values and pore sizes. The initial peak occurs between 0.28 and 0.31 ps while the final peak's position is temperature-dependent and occurs at

61

longer times as the temperature is lowered. The position of the larger peak $\tau_{\text{peak}}(Q)$ is weakly dependent on $\mathbf{Q}$ and occurs on a similar timescale as that of $\tau_\alpha(Q)$. However, it does not scale the same as a function of Q.

3.3 Water Intermediate Scattering Functions in Different Interfacial Regions

We examined $F_S(\mathbf{Q}, t)$ for molecules starting within the two different interfacial regions. We define the core region to be the region from $0 \leq \rho < d/2 - 6$ Å, and the shell region to be from $d/2 - 6$ Å$\leq \rho$. We note that previous studies have divided the pore into three sections, with the third section being outside the pore radius [27]. We divide the pore waters into two regions as with the mean squared displacements: core and shell waters. We use the same definition in Section 2.4.
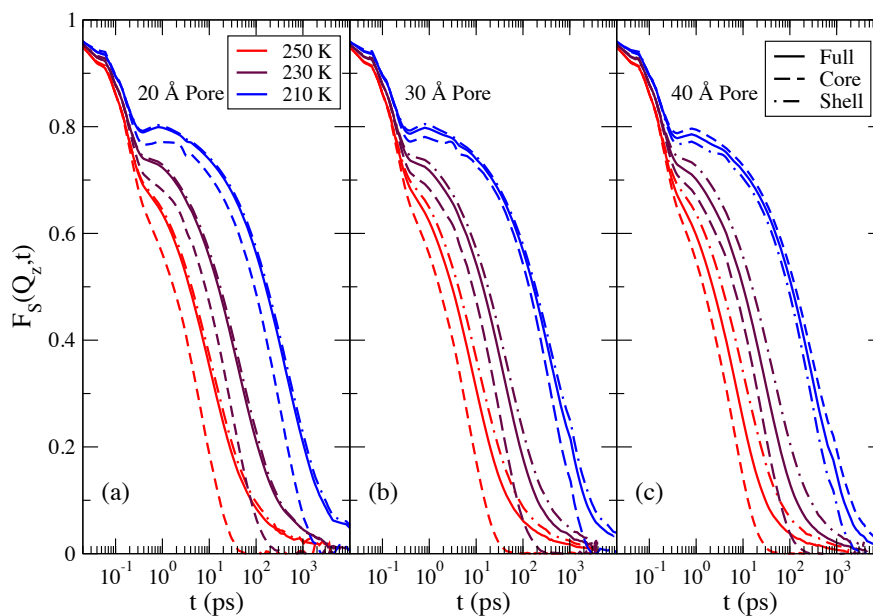
Figure 3.9: $F_S(\mathbf{Q}, t)$ where $\mathbf{Q}$ is in the axial direction for the three pore sizes. Shown are the full scattering function (solid lines), the scattering function calculated using the shell waters (dot-dashed), and the scattering function calculated using the core waters (dashed). For each pore the temperatures of 250 K, 230 K, and 210 K, listed from left to right, are shown.

In Figure 3.9 we show the full self-intermediate scattering function. We also show the self-intermediate scattering functions calculated for water molecules that start within the core region at $t = 0$, and for those water molecules that start within the shell region at $t = 0$. We show these curves for each pore and for temperatures of $T =$250 K, 230 K, and 210 K. The value of $\mathbf{Q}$ has been chosen to be along the axial direction. For each pore size, a plateau develops at intermediate times as the temperature is lowered. At long times, there is a slow decay in the full self-intermediate scattering function and in the shell self-intermediate scattering function. This is attributed to the low mobility of water molecules in the vicinity of the pore surface and for those water molecules within the pore matrix. Some of these water molecules only move a molecular diameter over the course of the simulation.

Water molecules that began within the core region, however, do not exhibit this slow decay at long times. In the smaller pores, a larger fraction of the water molecules begin in the shell region, and thus the full and shell self-intermediate scattering functions are close to each other. The full and shell functions are almost on top of each other in the 20 Å pore.

Chapter 4

Comparison of single particle dynamics at the center and on the surface of equilibrium glassy films

This chapter is based on the paper I completed in Professor Szamel's group. This paper was entitled 'Comparison of single particle dynamics at the center and on the surface of equilibrium glassy films'" and was authored by Kuon, Flenner, and Szamel. I was the first author on this paper for modeling and analyzing the system that appears in the paper.

4.1   Introduction

When molecules are vapor deposited onto a substrate to create glasses, the resulting glasses, providing the substrate is at about 85% of the glass transition temperature, can have higher kinetic stability than those created by cooling a bulk liquid [60–62]. These glasses also have a variety of other interesting properties when compared to glasses that have been created via quenching. These properties include lower heat capacities [63] and higher densities [59]. Because of these properties, vapor-deposited glasses have a wide variety of applications. Some of these include drug delivery [65], lithography [64] and protective coatings [66]. Because of the large number of applications and the general scientific interest in the glass transition, it is important to understand the microscopic mechanisms that give rise to these properties [67].

The mobility of particles at the surface of a vapor-deposited film is much larger than the mobility of particles in the bulk. It is this feature that allows for these films to create stable glasses. [61,68–78]. Because the surface particles are highly mobile, they are able to efficiently explore the potential energy landscape. Thus, they are able to find lower energy states than particles in the bulk region of the film. While a highly mobile surface being important for the creation of stable, vapor deposited glasses is clear, it remains to be seen whether the displacements of particles at the surface mirror the displacements of particles in the bulk or if they are different.

As they are supercooled, particles in the bulk can be divided into groups of particles that move slower or faster than what is expected from a Gaussian distribution [79]. As the dynamics slow, these dynamically heterogeneous regions increase in size [80–88] . It is believed that the increase in these dynamically heterogeneous regions is an essential property of glassy dynamics [80]. The spatial extent of the dynamically heterogeneous regions and strength of the heterogeneity are also related to the relative degree of slow-down of the dynamics of various classes of glass formers. Thus, it is natural to ask what happens to the dynamics at the surface of the film. The dynamics of the bulk change dramatically and it would be natural to wonder if the dynamics of the particles on the surface change dramatically, and if they occur on the same timescales as the bulk.

In this study we investigate the emerging heterogeneous dynamics at the surface of a supported, supercooled liquid film, and how these dynamics compare to a bulk-like region within the film. We start our analysis by examining the self-intermediate scattering functions. We use these functions to measure the average dynamics of particles that start at the surface of the film and those that start in the bulk-like region of the film. Then, we examine the single particle dynamics of equilibrium films. This is done for particles originally at the surface, and for particles originally in the bulk-like region of the film. We come to the conclusion that the dynamics in the bulk-like region are approximately three orders of magnitude slower than the dynamics at the surface. However, the distributions of the single particle displacements for particles that originate at the surface are similar to the distributions for particles that originate in the bulk-like region.

This chapter is organized in the following way. In Section 4.2, we describe the film creation technique and the simulations used in the study. We then examine the temperature-dependent properties of the film. We calculate the density profiles in the axial direction of the film (perpendicular to the substrate) as well as the alpha relaxation times. We examine how both properties depend on temperature with the relaxation times being calculated at the surface and in the bulk-like region. We also performed simulations of a bulk liquid and compare the alpha relaxation times in the bulk-like region of the film with the average relaxation times of the bulk liquid.

65

In Section 4.3.2 we examine the single particle displacements and how they depend on temperature for particles that originate at the surface and those that originate in the bulk-like region. We compare the surface and the bulk in two ways: when the two regions are at the same temperature, and when the two regions have a similar relaxation times.

4.2 Simulations

The simulations were done using the binary Lennard-Jones mixture introduced by Kob and Andersen [103–105]. This mixture will henceforth be referred to as the Kob-Andersen mixture. The interaction potential is the Lennard-Jones potential defined as

$$U_{\alpha\beta}(r) = 4\epsilon_{\alpha\beta} \left[\left(\frac{\sigma_{\alpha\beta}}{r} \right)^{12} - \left(\frac{\sigma_{\alpha\beta}}{r} \right)^{6} \right] \tag{4.1}$$

where α and β denotes the particle type A or B. The potential was cut off at 2.5 σ_{AA}. The parameters are $\epsilon_{AA} = 1.0$, $\sigma_{AA} = 1.0$, $\epsilon_{AB} = 1.5\sigma_{AA}$, $\sigma_{AB} = 0.88\sigma_{AA}$, $\epsilon_{BB} = 0.5\epsilon_{AA}$, and $\sigma_{BB} = 0.8\sigma_{AA}$. The ratio of A particles to B particles is 80:20 and all the particles have the same mass. We present our results in units where ϵ_{AA} is the unit for energy, σ_{AA} is the unit for distance, ϵ_{AA}/k_A is the unit for temperature, $\epsilon_{AA}/\sigma_{AA}$ is the unit for pressure and $\sqrt{m_A\sigma^2/\epsilon_{AA}}$ is the unit for time. The system of coordinates was chosen such that the z-axis was perpendicular to the substrate. The simulations were performed using the HOOMD-blue package [106]. The simulation timestep was 0.003 and all simulations were run on an NVIDIA K40c GPU (graphics processing unit).

4.2.1 Creating the Film

To create the film we first made a substrate from Kob-Andersen particles and subsequently deposited more KA particles on to the substrate. We made the substrate by simulating a 1000 KA particle bulk system in the NVT ensemble with a density of $N/V \approx 1.18$ which corresponds to a box length of 9.46322. This system was then cooled at a rate of $\dot{T} = 1 \times 10^{-8}$ to a temperature of $T = 0.3$. This configuration was then placed at the bottom of a box with side lengths $l_x = l_y =$

$9.46322\sigma_{AA}$ and $l_z = 67.46322\sigma_{AA}$. The substrate particles were tethered in place by particles whose equations of motion were not integrated over during the course of the simulations. These particles tethered the substrate particles in place via the harmonic potential

$$V(r) = \frac{1}{2}kr^2. \tag{4.2}$$

where r is the distance between the substrate particle and the non-integrated particle and $k = 1000$. The substrate particle positions and velocities were updated using a Nosè-Hoover NVT integration routine.

Periodic boundary conditions were used for all three cartesian axes, but particles were prevented from leaving the box in the axial direction by a repulsive wall. The repulsive wall was placed near the top of the box to repel particles that may have evaporated from the film surface. The potential functional form used to define this repulsive wall was a Yukawa potential. The Kob-Andersen particles were introduced one at a time to the system in groups of five. First, four A particles were introduced, followed by one B particle to keep the ratio consistent. The particles were introduced near the repulsive wall. The particles were given a velocity that was randomly sampled from a Maxwell-Boltzmann distribution defined as

$$f(v) = 4\pi v^2 \left(\frac{m}{2\pi k_B T}\right)^{3/2} e^{\frac{-mv^2}{2k_B T}}, \tag{4.3}$$

where $T = 1.0$. The newly introduced particles' equations of motion were integrated in the constant energy ensemble so that their velocity remained constant. During this process, the particles exchanged energy with the substrate and this process was repeated until a total of 4000 particles were introduced. The following algorithm illustrates this process.

After creating the film, we encountered a complication in the analysis due to a finite-size effect in the form of shear modes in the system. When the self-intermediate scattering functions were calculated, oscillations in the plateau value of the function were observed to be larger than

67

Algorithm 1 Vapor Deposition Algorithm

1: **for** ncycles $= 1,800$ **do**
2:     **for** n $= 1,5$ **do**
3:         **if** n $\neq 5$ **then**
4:             Create Particle A
5:         **else**
6:             Create Particle B
7:         **end if**
8:         x $= l_x \times$ rand$(-0.5, 0.5)$ ▷ Assign Positions
9:         y $= l_y \times$ rand$(-0.5, 0.5)$
10:        z $= 0.5 \times l_z - 2.5$
11:        $v_x = v_y = 0.0$ ▷ Assign Velocities
12:        $v_z = -v(T)$
13:        Run NVE Simulation for $\gamma\, dt$ Steps
14:    **end for**
15: **end for**

---

expected. The complications are attributed to the small aspect ratio of the system. To solve this issue, we quadrupled the system size by replicating the system in the x and y directions.

Figure 4.1 shows the self-intermediate scattering function (equation 4.4) calculated for A-particles with **k** in the parallel (xy) direction. The film was divided in the perpendicular (z) direction into one σ_{AA} thick regions and the self-intermediate scattering function for each region was calculated for A-particles that started in that particular region. Figure 4.1(a) shows the self-intermediate scattering functions before the system was quadrupled in size. Figure 4.1(b) shows the self-intermediate scattering functions after the system was enlarged. Curves with a longer decay are closer to the substrate. From the figure, it is clear that quadrupling the system size has a dramatic effect on the qualitative behavior and average dynamics of the self-intermediate scattering functions for the different regions of the film. Immediately visible are large oscillations in the self-intermediate scattering functions at intermediate times in 4.1(a) as compared to 4.1(b), which have small to no oscillations at intermediate times. The system size also has a dramatic effects on the average dynamics. This is especially apparent for the faster decaying self-intermediate scattering functions. These faster decaying functions correspond to the regions closer to the surface of the film, an area of significant importance to this work. The shear modes in the smaller substrate
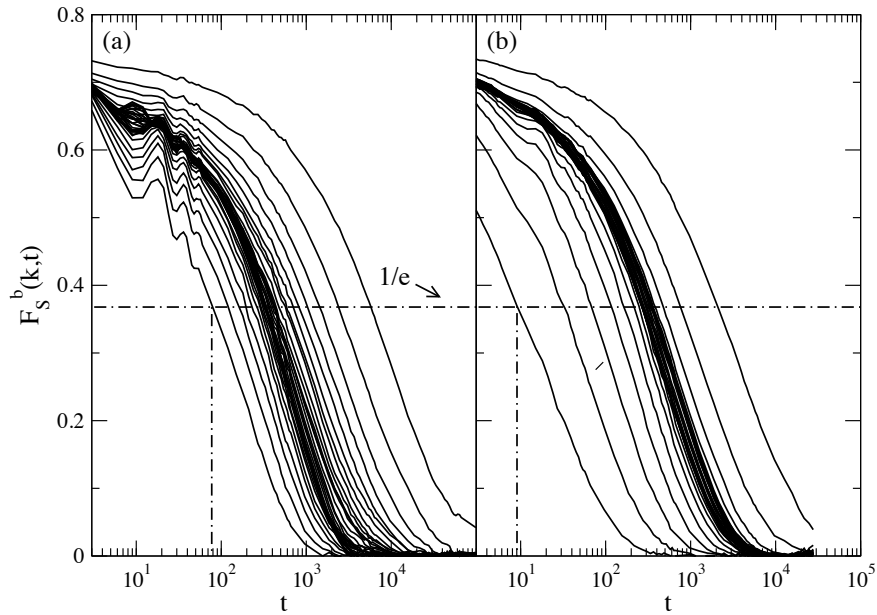
Figure 4.1: Plot of the self-intermediate scattering function calculated using the A-particles for **k** in the parallel (xy) directions. The temperature is 0.37. The film is divided into regions of size one σ_{AA} and each curve is calculated for A-particles that start in a particular region. Plot (a) shows the self-intermediate scattering function before the system was quadrupled in size while plot (b) shows the function after the system was quadrupled in size.

69

have the effect of slowing the average dynamics of particles that start in the regions close to the surface. To highlight this effect, a horizontal line is drawn in both plots indicating the height at which the self-intermediate scattering function has decayed to a value of 1/e, the usual definition of the alpha relaxation time. A vertical line is then drawn on both plots that shows at what time the fastest decaying curve reaches a value of 1/e. For the small system, this value is approximately 80 time units, while for the large system this value has decreased by almost an order of magnitude, being approximately 9 time units. Thus, this finite size effect must be taken account if reliable results are to be obtained.

When the film was complete it was composed of 16000 particles; the height was approximately $40\sigma_{AA}$; and the film had a box length in the x and y-directions of $l = 18.92644$. We then simulated the film at a temperature of 0.5 for approximately $100\tau_{\alpha}$ to remove any composition or density effects that may have occurred during the deposition process. Figure 4.2 shows a snapshot of the
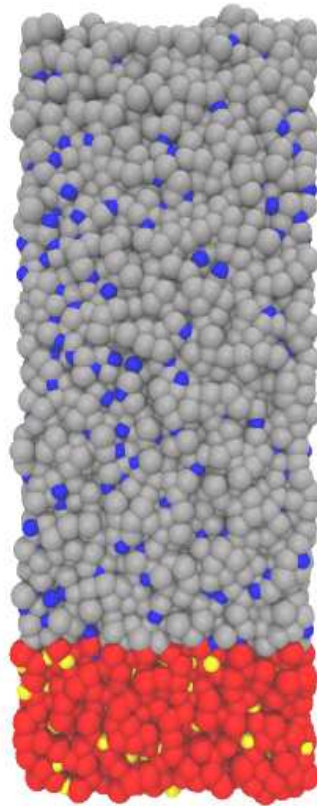
Figure 4.2: Snapshot graphic of the film and substrate. Particles in gray and blue constitute A and B particles in the film while red and yellow particles constitute A and B particles in the substrate.

system.

4.2.2   Equilibrium Simulations

Both the NVT and NPT simulations were performed using a Nosè-Hoover thermostat and barostat. The thermostat and barostat had coupling constants of 0.2 and 2.0, respectively.

The film was simulated in the NVT ensemble. At each temperature, we equilibrated the system for at least $100\tau_\alpha$, and ran production runs for another $100\tau_\alpha$. The initial condition was the simulated system at the next highest temperature. Our temperature range went from $T = 0.5$ to $T = 0.35$. Also performed were 1000 particle bulk simulations in the NVT and NPT ensemble. These bulk simulations were run the same way that the film simulations were run. However, the repulsive wall and substrate are not present.

4.3   Results

4.3.1   General Properties of the Film

This subsection examines the average density and dynamics of the film and how they depend on the temperature. First, we show that there is a mild increase of the density with decreasing temperature. We then define the surface region of the film using the density profile of the film; then we define the bulk-like region of the film using the dependence of the relaxation time on the distance from the substrate. We also analyze the self-intermediate scattering functions for particles that start in the surface region and for those that start in the bulk-like region. This analysis allows us to calculate the relaxation times for the bulk-like and surface regions. We then use this to examine the average relaxation time versus temperature of the film. Our findings indicate that the average relaxation time at the lowest temperature, for particles that start in the bulk-like region, is approximately three orders of magnitude larger than those that start in the surface region.
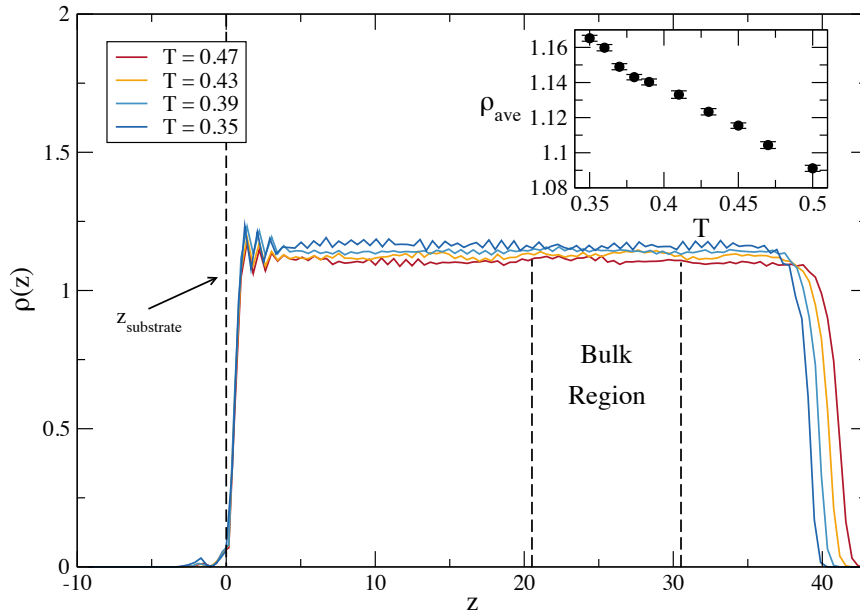
Figure 4.3: Density of the film as a function of z for temperatures of $T = 0.47$, 0.43, 0.39 and 0.35. The inset shows the average density of the center of the film as a function of temperature. The position of the substrate is defined as $z = 0$. The bulk region of the film is also indicated.

Density and Self-Intermediate Scattering Functions

Figure 4.3 shows the density profile in the z-direction with z being the perpendicular distance from the substrate. We define $z = 0$ to be the substrate surface. Figure 4.3 shows the density profile at four temperatures: $T = 0.47$, 0.43, 0.39, and 0.35. The small peaks that occur for $z < 0$ are the few particles that have moved into the substrate during the simulations. Adjacent to the substrate are several increasingly small peaks that indicate layering of the particles next to the substrate. Beyond this region the density is nearly constant until the edge of the film where the density drops abruptly. The density drops over a distance of roughly σ_{AA}.

As seen in the figure, the film width decreases with decreasing temperature, and, correspondingly, the density in the center is inversely proportional to temperature. The temperature dependence of the density in the center of the film is shown in Figure 4.3. We find that the average density increases by $\approx 10\%$ between $T = 0.5$ and $T = 0.35$. To be consistent, we define the edge of the film to be the point z at which the density drops to half of its average value in the center, a definition used in a previous work [75]. We then define the surface region to be all particles that

lie within σ_{AA} of the film edge. The bulk region is defined as the $10\sigma_{AA}$ region in shown in Figure 4.3.

To study the average dynamics, we calculate the self-intermediate scattering function.

$$F_S(\mathbf{k}, t) = \left\langle \sum_{n=1}^{N_A} \exp i\mathbf{k} \cdot [\mathbf{r}_n(t) - \mathbf{r}_n(0)] \right\rangle. \tag{4.4}$$

In the above equation, the sum is over the A-particles. The value of $\mathbf{k}$ is chosen to be the position of the first peak in the A-particles' structure factor, and has a value of 7.25. The film is isotropic in the x and y-directions, but not in the z-direction, and thus $F_S(\mathbf{k}; t)$ is dependent on both magnitude and direction of $\mathbf{k}$. In light of this, we calculate $F_S(\mathbf{k}; t)$ for two directions: perpendicular and parallel to the substrate.
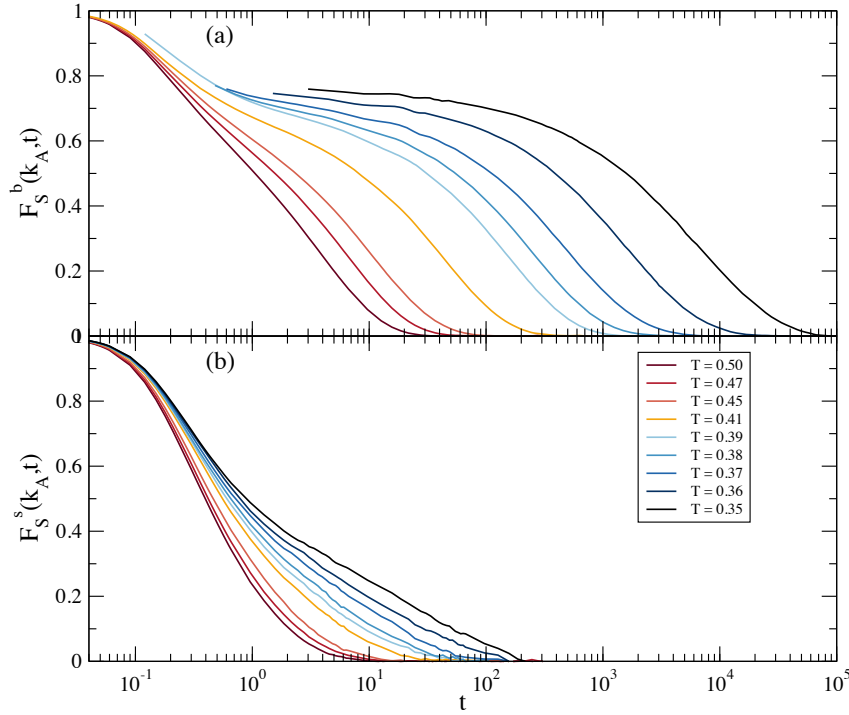
Figure 4.4: Self-intermediate scattering functions for the bulk-like (a) and surface (b) region of the film are shown at all simulated temperatures.

$F_S(\mathbf{k}; t)$ was calculated for particles that start in the bulk region at $t = 0$, and for particles that start in the surface layer at $t = 0$. We will denote these functions as $F_S^{b,s}(\mathbf{k}; t)$. In Figure 4.4(a)

73

is $F_S^b(\mathbf{k}; t)$, with $\mathbf{k}$ parallel to the substrate. The characteristic features of supercooled liquids are visible. The initial fast decay at short times is indicative of ballistic motion. Below temperatures of 0.41, a plateau at intermediate times develops that persists for longer times as the temperature is lowered. Additionally, the height of this plateau increases slightly as temperature decreases, which may be connected to the increasing density described above. This plateau implies transient localization of the particles. The particles are increasingly localized as the temperature is lowered, indicated by the increase in the length of the plateau. After enough time has passed, the particles escape from their transient cages and $F_S^b(\mathbf{k}; t)$ decays to zero.

In Figure 4.4(b) we show $F_S(\mathbf{k}; t)$ for particles that start in the surface region, with $\mathbf{k}$ being parallel to the substrate. We do not observe the characteristic features of glassy behavior for particles starting at the surface, despite an increase in the relaxation time of almost two orders of magnitude. Notably, there is no plateau at intermediate times that is observed for particles starting in the bulk region. This is similar to what is found two-dimensional glass forming systems [89–92]. Although the scattering function decays much faster than what is observed in the bulk region, the decay is very non-exponential. The non-exponential decay implies that the dynamics are not diffusive on the time scale probed by $F_S^s(\mathbf{k}; t)$.

Next, the film's relaxation as a function of distance from the substrate was examined. The film was divided into one σ_{AA} sized regions and $F_S(\mathbf{k}; t)$ was calculated with $\mathbf{k}$ parallel and perpendicular to the substrate. This was done for particles that started in the particular region. In Figure 4.5, $F_S(\mathbf{k}; t)$ for these regions are shown for the intermediate temperature of $T = 0.41$. The curves are colored based on the three regions defined below. Dotted and solid lines are for $\mathbf{k}$ in the perpendicular and parallel directions respectively. For curves colored blue, the curve shapes are dominated by a plateau at intermediate times that decreases in length and height as z is increased. After approximately $5\sigma_{AA}$, the shape of the curve stops changing as quickly and for multiple layers remains approximately the same shape, indicating the bulk-like region. At approximately $32\sigma_{AA}$, the shape of the curve begins to change again as the surface of the film is approached. The plateau again decreases in length and width before disappearing entirely at approximately $38\sigma_{AA}$.
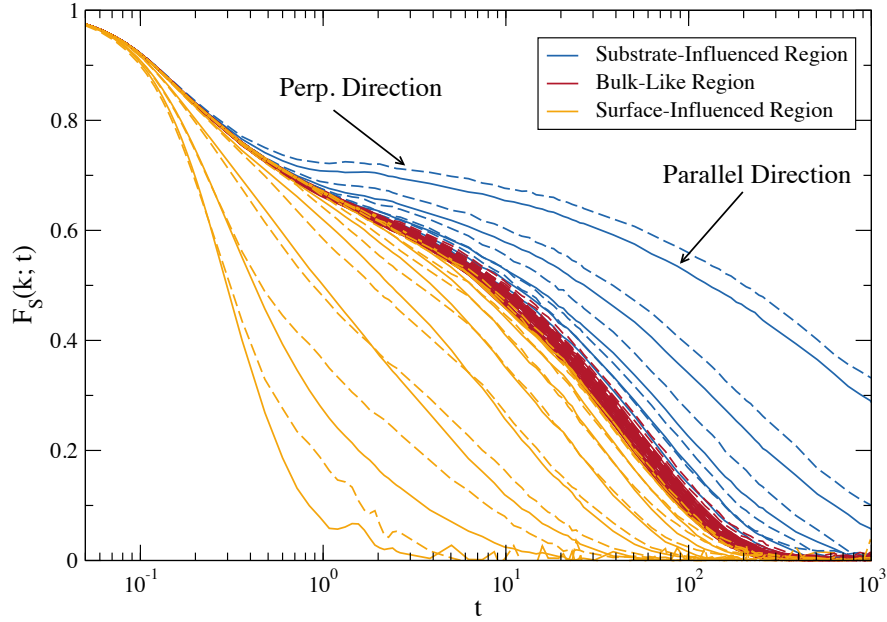
Figure 4.5: Self-Intermediate scattering functions of the film as a function of z for a temperature of 0.41. Particle motion in the parallel and perpendicular directions is represented, respecetively, by solid and dotted lines. The curves are colored by the three regions defined in the text.

Alpha Relaxation Times

Next, the alpha relaxation times were calculated for the surface and bulk-like regions for all temperatures and are defined by the relation $F_S(\mathbf{k}, \tau_\alpha) = 0.2$. This is true for all figures except Figure 4.10. It is calculated for $\mathbf{k}$ parallel and perpendicular to the substrate. For Figure 4.10 the relaxation time is defined through $F_S(\mathbf{k}, \tau_\alpha) = 1/e$.

To properly quantify the relaxation time of the bulk-like region of the film, we compared the relaxation times with simulations of 1000 particles and periodic boundary conditions in all directions. We refer to these simulations as bulk simulations. Two sets of bulk simulations were performed. The first used the condition of constant pressure, P, where the pressure was calculated from the pressure at the center of the film. The second set used a condition of constant volume. The volume V was chosen to be equal to the average volume of the simulations at constant pressure.

The value of the pressure in the constant pressure simulations was determined by dividing the film into bins of width δz, and calculating the components of the pressure tensor using the virial

definition [93]

$$P_{\alpha\beta}(z) = \rho(z)k_B T - \frac{1}{2A}\left[\sum_{i=1}^{N}\sum_{j\neq i}\frac{r_{ij\alpha}r_{ij\beta}}{r_{ij}}u'(r_{ij})\right]. \qquad (4.5)$$

In this equation, the i and j indices run over the particles; the α and β indices denote the cartesian coordinates x,y and z, $\mathbf{r}_{ij}$ is the vector pointing from particle i to particle j with r_{ij} being its magnitude; and $u(r_{ij})$ is the interparticle potential energy. The second term is zero if particle i is not within the interval $[z, z+\delta z]$. If particle j is also within the interval $[z, z+\delta z]$, the second term is simply the value given by term 2 in 4.5. If particle j is outside the interval, the second term in 4.5 is divided by two.
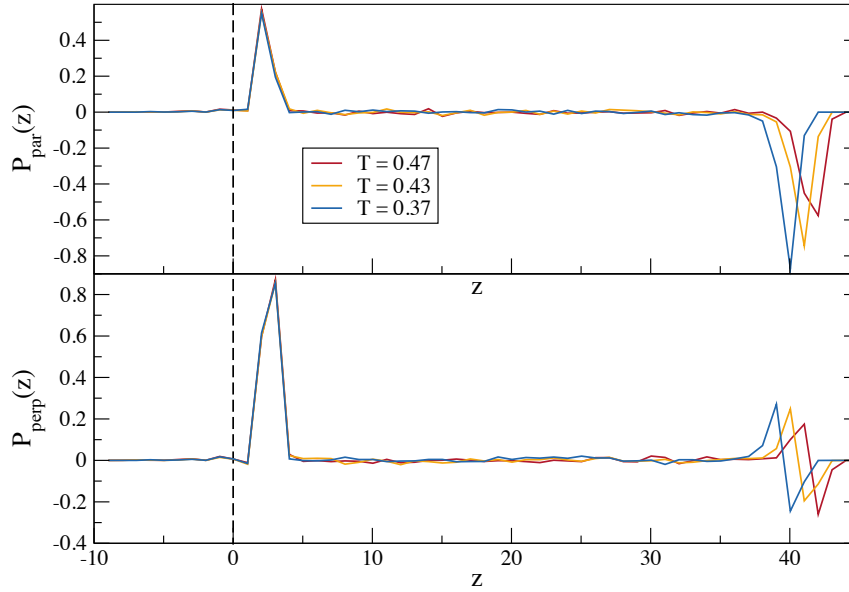
Figure 4.6: The parallel and perpendicular component of the pressure tensor is shown as a function of z for film temperatures of $T = 0.47$, 0.43 and 0.37. The parallel component is the average of P_{xx} and P_{yy} while the perpendicular component is simply P_{zz}. The position of the substrate is defined as $z = 0$.

Figure 4.6 shows the parallel and perpendicular components of the pressure tensor as a function of z at film temperatures of $T = 0.47$, 0.43, and 0.37. The parallel component of the pressure tensor is the average of the components P_{xx} and P_{yy}, while the perpendicular component is the component P_{zz}. The pressure profiles can be divided into three regions: (1) a region influenced by the substrate; (2) a uniform region in the center of the film; and (3) a region influenced by

the edge of the film. Region (1) is approximately $5\sigma_{AA}$ in width and displays a large spike in the pressure. This is indicative of the pressure due to the presence of the substrate. The perpendicular component of the tensor is larger than the parallel component. Region (2) has a uniform value of $P_{par} = P_{perp} = 0$. Thus, the NPT simulations were performed at a constant pressure of $P = 0$. Region (3) is quite different qualitatively for the parallel and perpendicular component, and has a width of approximately $10\sigma_{AA}$. The width of region (2) decreases with decreasing temperature. The parallel component displays a large negative spike in its value before decaying to zero at the very edge of the film. This negative spike becomes larger as the temperature is lowered and occurs at a lower z-value. The perpendicular component has two spikes in this region: an initial positive spike, indicative of the presence of the lower film layers, followed by a negative spike before the perpendicular component of the pressure tensor decays to zero at the edge of the film. This is indicative of the surface tension of the film. The initial spike gets larger with decreasing temperature.
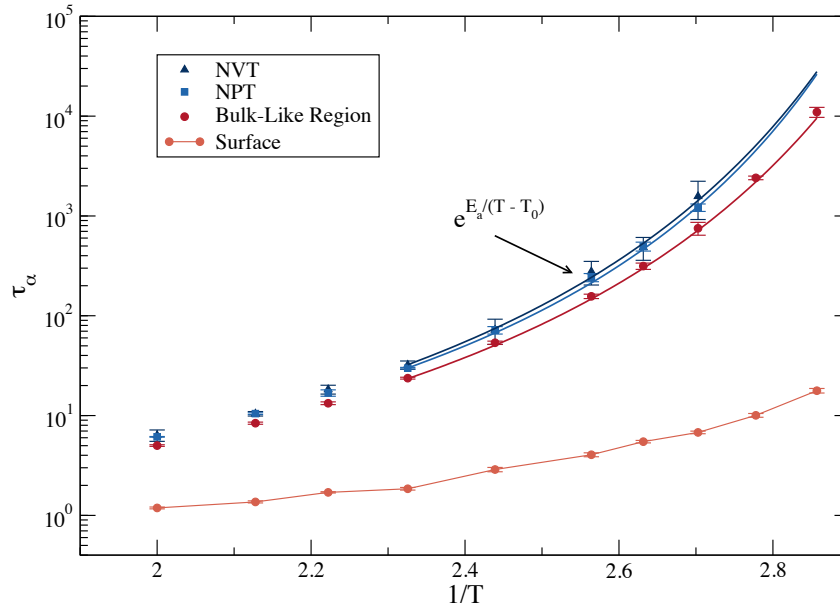
Figure 4.7: The alpha relaxation times as function of inverse temperature are shown for bulk NVT simulations (dark blue line), bulk NPT simulations (blue line), the bulk-like region of the film (red line), and the surface layer of the film (orange).The NVT, NPT and bulk-like regions are fit with a Vogel-Fulcher fit and the fits gave T_0 values of 0.291 ± 0.007, 0.295 ± 0.002 and 0.287 ± 0.0007 for NVT, NPT and bulk-like region respectively.

In Figure 4.7 the temperature dependence of the relaxation time is shown for the bulk region (red circles), and the surface region (orange circles). The surface region's relaxation time increases slower with decreasing temperature than does the bulk region's. The bulk relaxation time is approximately five times greater than the surface region at $T = 0.5$, but at $T = 0.35$ the bulk region's relaxation time is almost three orders of magnitude larger than the surface region's relaxation time. The NVT (dark blue triangles) simulations and the NPT (blue squares) simulations give, with error bars, the same results for the relaxation time in Figure 4.7. We find that the relaxation times for the bulk simulations are longer than the relaxation times for the bulk-like region of the film.

To further quantify the temperature dependence, we fit the relaxation times of the bulk simulations and the bulk-like region of the film with a Vogel-Fulcher equation

$$\tau_\alpha = \tau_0 e^{\left(\frac{E_b}{(T-T_0)}\right)}. \tag{4.6}$$

We find that $T_0 = 0.291 \pm 0.007$ for the NVT simulations, $T_0 = 0.295 \pm 0.002$ for the NPT simulations, and $T_0 = 0.287 \pm 0.0007$ for the film. Statistically, we can therefore say that T_0 is the same for the NVT and NPT simulations, but is slightly lower for the film. Lyubimov, Ediger and de Pablo found an optimum substrate value of $T_0 = 0.3$ for their vapor deposition simulations. This is very close to our film's fitted T_0 value.

We also calculated the ratios $\tau_\alpha^{NPT}/\tau_\alpha^{film}$ and $\tau_\alpha^{NVT}/\tau_\alpha^{film}$. These ratios are shown in Figure 4.8 with the NPT ratio being red squares and the NVT ratio being blue diamonds. In this figure it can be seen that the NPT ratio and the NVT ratio have the same temperature dependence within error bars. We find that this ratio increases slightly with decreasing temperature, having a value of 1.5 when $T = 0.5$ and a value of ≈ 1.75 at $T = 0.35$. This serves to further quantify that the relaxation times in the bulk-like region of the film are slightly lower than the bulk simulations.

The temperature dependence of the relaxation times is different for particles that start in the surface layer than for particles that start in the bulk region. To quantify this, the ratio $\tau_\alpha^b/\tau_\alpha^s$ was calculated and its temperature dependence is shown in Figure 4.9. The value of this ratio is shown on the figure at the highest temperature, $T = 0.5$, where it has a value of 4.2123 and the lowest

78
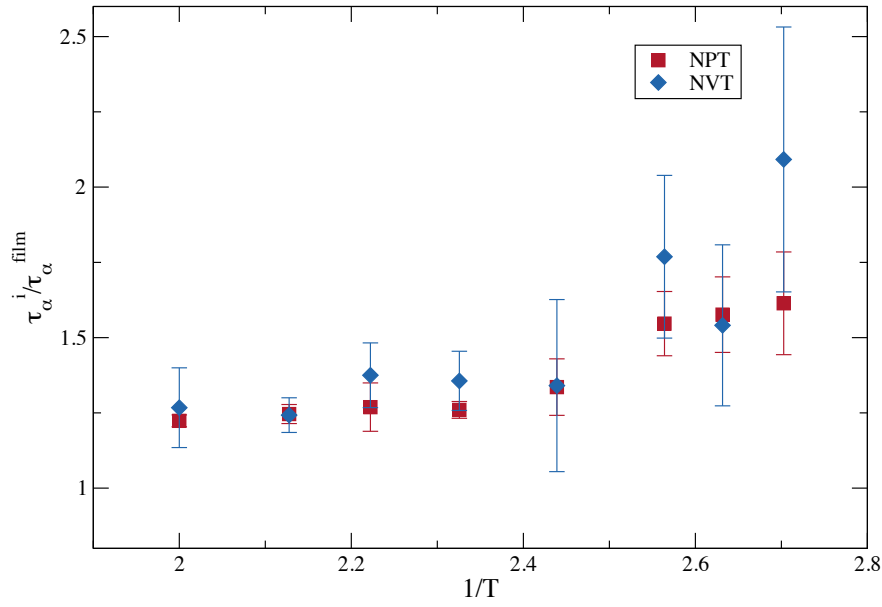
Figure 4.8: The ratios $\tau_\alpha^i/\tau_\alpha^{film}$ are shown where i = NPT, NVT. The NPT and NVT ratios are the red squares and blue diamonds respectively.
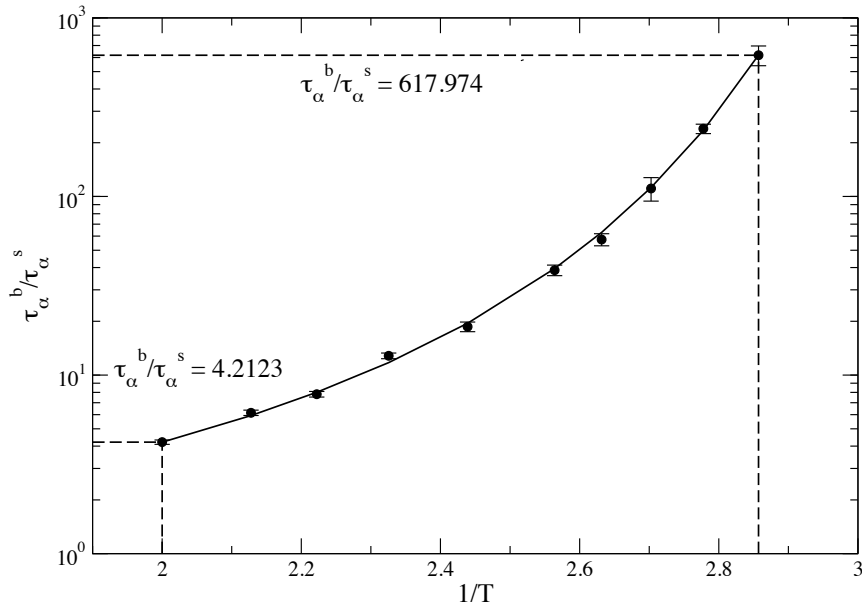
Figure 4.9: The ratio $\tau_\alpha^b/\tau_\alpha^s$ versus inverse temperature is shown. The value of the ratio at the highest temperature ($1/T = 2.0$), and the lowest temperature ($1/T = 2.85$) are referred to by the dashed lines.

temperature, $T = 0.35$, where it has a value of 617.974. The dramatic increase in this ratio as the temperature is lowered indicates that the self-intermediate scattering function in the bulk region decays much slower than the function in the surface layer as the temperature is lowered. This effect can be seen in the shapes of the curves in Figure 4.4.
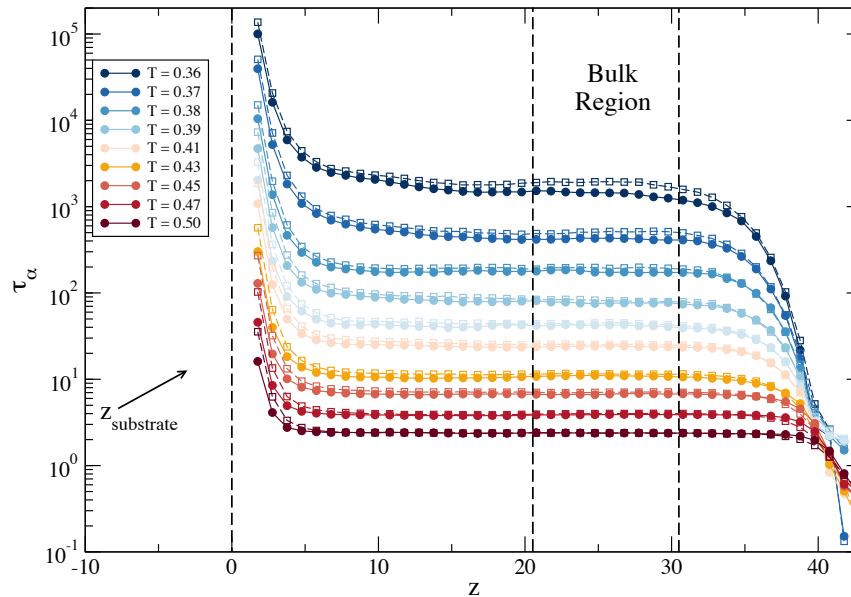
Figure 4.10: Relaxation times of the film as a function of z for all temperatures. Particle motion in the parallel and perpendicular directions is represented by solid and open data points respectively. The position of the substrate is defined as $z = 0$.

In Figure 4.10 the alpha relaxation time as a function of z is shown for the A-particles for both **k** parallel (empty circles) and **k** perpendicular (filled circles) to the substrate. The position of the substrate is shown as a vertical dashed line. The z-dependence of the alpha relaxation time can be divided into three different regions: (1) a region influenced by the substrate; (2) a bulk-like region; and (3) a region influenced by the surface. The relaxation times in region (1) are large compared with center of the film, but they quickly decrease over approximately $5\sigma_{AA}$.

In the center of the film, the relaxation time as a function of z is nearly constant until the edge of the film is reached. For temperatures less than 0.38, the relaxation time slowly decays to its plateau value over approximately $15\sigma_{AA}$. Near the surface, the final decay of the relaxation time

occurs at approximately $32\sigma_{AA}$ from the substrate, and falls quickly to a minimum value. The position of this minimum value is dependent on the edge of the film, which is, in turn, dependent on the temperature, as shown above. The relaxation time profiles were used to define the bulk-like region, which is the statistically uniform region in the center of the film. This region is shown in Figure 4.10.

4.3.2 Comparison of Particle Displacements at the Surface and Within the Bulk

We examined in the previous section the average dynamics of the film by analyzing the self-intermediate scattering functions. The temperature dependence of τ_α was found to be different for particles that started at the surface than for those that started in the bulk-like region. The temperature range used in this work does not indicate the emergence of a plateau for $F_S^s(\mathbf{k}; t)$, while a plateau clearly emerges for $F_S^b(\mathbf{k}; t)$. However, it is noted that both regions display a non-exponential decay, indicative of heterogeneous dynamics. To better understand the single particle motion that gives rise to these heterogeneous dynamics, single particle displacements will now be examined.

To obtain additional information on the dynamics, the distribution of the particles' displacements in real space at a set time separation is investigated via the self-van Hove correlation function [5]

$$G_s(\delta \mathbf{r}; t) = \left\langle \frac{1}{N} \sum_{i=1}^{N} \delta \left(\delta \mathbf{r} + \mathbf{r}_i(0) - \mathbf{r}_i(t) \right) \right\rangle. \tag{4.7}$$

The self-van Hove correlation function gives the probability that a particle has moved a distance $\delta \mathbf{r}$ in a time t. $G_S(\delta \mathbf{r}; t)$ is a Gaussian distribution for diffusive motion. Gaussian behavior can be better seen by examining the probability of the logarithm of single particle displacements $P\left[\log_{10}(\delta \mathbf{r}); t\right]$ [96–99]. Two-dimensional motion parallel to the substrate is the principle motion of concern, so the two-dimensional version of $P\left[\log_{10}(\delta \mathbf{r}); t\right]$, $P\left[\log_{10}(\delta r_{xy}); t\right]$ is used, where $\delta r_{xy} = \sqrt{[x(t) - x(0)]^2 + [y(t) - y(0)]^2}$. $P\left[\log_{10}(\delta r_{xy}); t\right]$ can be obtained from the two-dimensional self-van Hove function via

$$P\left[\log_{10}\left(\delta r_{xy}\right); t\right] = 2\pi \ln(10)\delta r_{xy}^2 G_s(\delta r_{xy}; t). \tag{4.8}$$

The distribution of the logarithm of single particle displacements is a useful tool since the shape of the distribution does not depend on time and the peak height is equal to $2\ln(10)e^{-1} \approx 1.69$ for a Gaussian self-van Hove function. This function can then be used to identify some features of glassy dynamics, namely hopping-like motion, as well as non-Gaussian displacements [96–99].
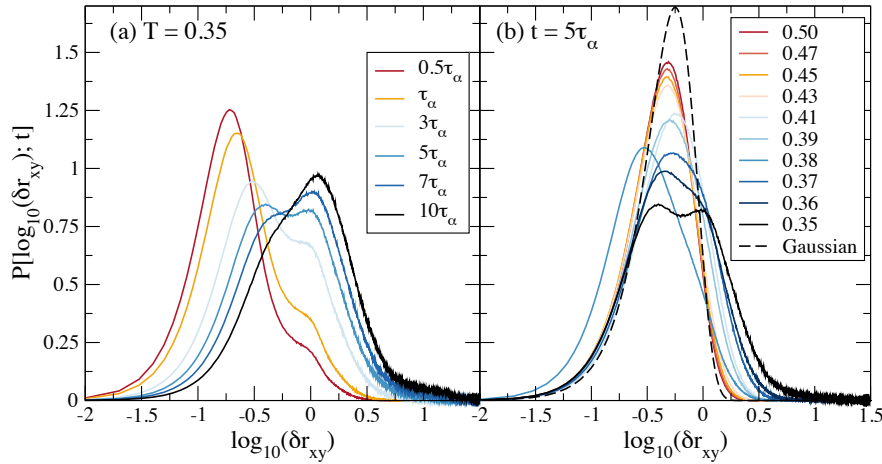
Figure 4.11: The behavior of the probability of the logarithm of displacements as it varies with: (a) time separation (in multiples of τ_α^b) and (b) temperature (all temperatures shown). Both figures show the probability of the logarithm of the displacements in the bulk-like region of the film. A Gaussian distribution calculated using the mean squared displacement at $T = 0.5$ is shown for comparison.

In figure 4.11, $P\left[\log_{10}(\delta r_{xy}); t\right]$ is shown for the bulk-like region of the film for its dependence on: (a) time at the lowest temperature of $T = 0.35$ and (b) temperature at a time separation of $5\tau_\alpha^b$. A Gaussian distribution is not followed by any of the curves in figure 4.11 since all of the peak heights are less than 1.69.

At the lowest temperature of $T = 0.35$, a shoulder begins to emerge in $P\left[\log_{10}(\delta r_{xy}); t\right]$ at a time separation of $0.5\tau_\alpha^b$. This indicates already defined fast and slow populations. With increasing time separation, the first peak moves to the right and decreases in size, while the shoulder grows and moves to the right as well. There are two clearly defined peaks at a time separation of $5\tau_\alpha^b$. Even at

a time separation of $10\tau_\alpha^b$ the particle displacements do not constitute motion described by Fickian diffusion and are not Gaussian in their distribution. The displacements imply the hopping-like motion observed frequently in simulation [99–101, 107] and experiments [108–110] on supercooled liquids.

In figure 4.11(b), $P\left[\log_{10}(\delta r_{xy}); t\right]$ is shown as it depends on temperature at a fixed time separation of $5\tau_\alpha^b$. This time separation was chosen since two peaks can be clearly seen for $T = 0.35$. It can be seen, as the temperature is decreased, the dynamics become increasingly heterogeneous.

Thus, the characteristics of the hopping-like motion, associated with dynamic heterogeneities of bulk supercooled liquids, are seen in the center of the film. How the particle displacements change for particles that start at the surface of the film will now be compared with those displacements for particles that start in the bulk-like region. This comparison will be done for displacements as a function of temperature and for displacements as a function of time separation.

This comparison is done in two different ways. First, the displacements of particles starting in the surface and bulk regions are compared when the two regions are at the same temperature. Due to the higher mobility of the surface, the surface particles move much farther than the bulk particles at a fixed time separation. Therefore, this comparison will be performed at the same multiples of the bulk relaxation time and of the surface relaxation time. Next, the distributions for particles that start in the bulk-like region and in the surface region are compared when the two regions have approximately the same alpha relaxation time $\tau_\alpha^{s,b}$. This requires the two regions to be at different temperatures. The relaxation time is defined through $F_s^{s,b}(\mathbf{k}, \tau_\alpha^{s,b}) = 0.2$, as in figure 4.7.

In figure 4.12, $P\left[\log_{10}(\delta r_{xy}); t\right]$ is shown at temperatures of $T = 0.37$, 0.36 and 0.35 for particles that start in the bulk-like region and for particles that start in the surface region. The temperature decreases from bottom plots to top plots. The time separation increases from left plots to right plots as can be seen in the figure.

At time separations of $\tau_\alpha^{s,b}$, the distributions of the bulk-like region and surface layer are qualitatively similar in shape at $T = 0.37$. The bulk curve is shifted slightly to the left due to the average displacement of those particles being smaller on this time scale. The distribution for the
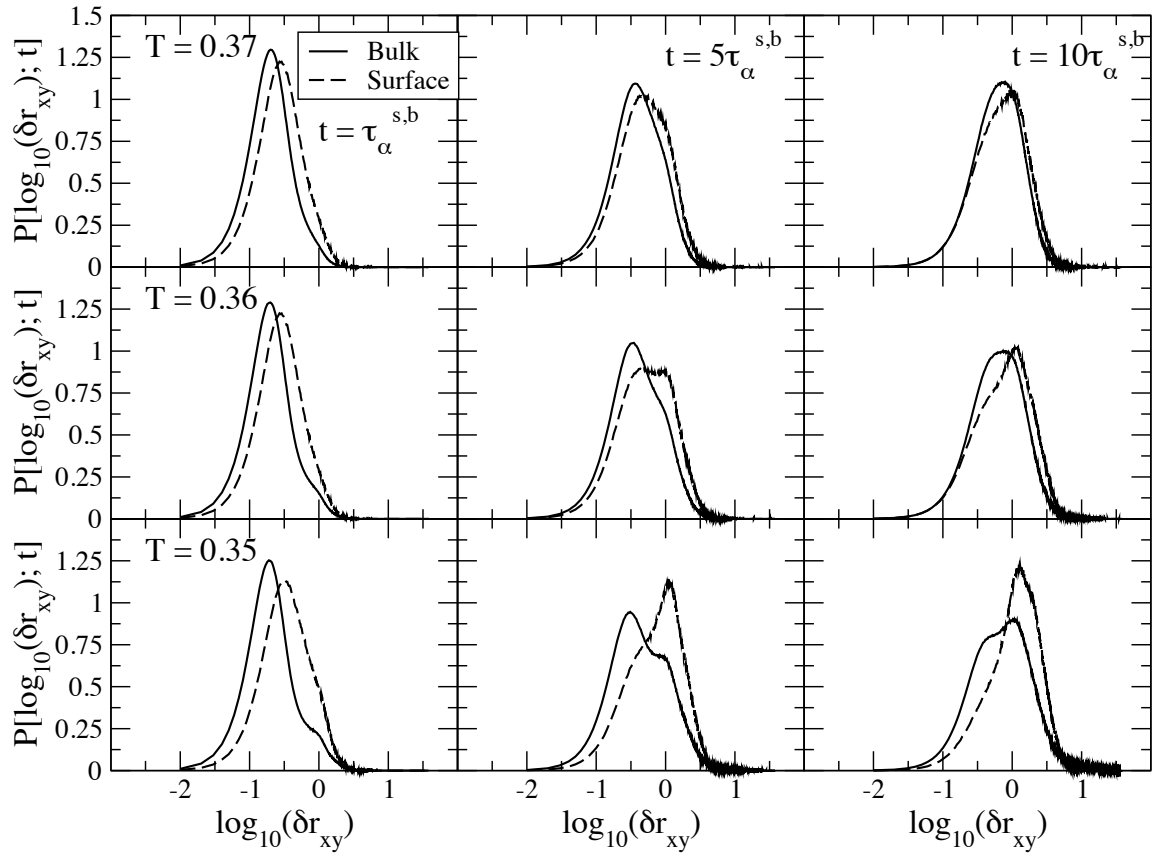
Figure 4.12: Comparison of the surface (dashed line) and bulk (solid line) $P[\log_{10}(\delta r_{xy}); t]$ at the same temperature. The time separation increases with each figure from left to right and displays values of $\tau_\alpha^{s,b}$, $5\tau_\alpha^{s,b}$, and $10\tau_\alpha^{s,b}$. The temperature increases in each figure from top to bottom and has values of $T = 0.35$, 0.36 and 0.37.

surface particles is slightly wider than the bulk curve. A shoulder appears at $\log_{10}(\delta_{xy}) = 0$ for lower temperatures, which indicates a displacement of one A-particle diameter. The shoulder is present both at $T = 0.36$ and $T = 0.35$ and is more pronounced at the lower temperature. This shoulder indicates a small fraction of particles in the bulk region having faster dynamics.

At time separations of $5\tau_{\alpha}^{s,b}$, the curves of both regions have qualitatively similar shapes and heights at $T = 0.37$. A shoulder appears in both the surface and bulk-like regions at $T = 0.36$. This is again indicative of faster dynamics from a small fraction of the particles. The peaks for the faster and slower particles are approximately the same height in the bulk region. The faster particle distributions still have the higher height in the surface region. The majority of the particles in the surface layer have faster displacements at $T = 0.35$, with only a small fraction of slower particles still present. At $T = 0.35$ in the bulk region, the peaks indicating the faster and slower particles have separated. This implies that the regions of faster and slower particles are becoming more distinct. Although the surface dynamics are two orders of magnitude faster than the bulk region's, the particle displacements are remarkably similar to those found in the bulk, albeit on vastly different time scales.

At time separations of $10\tau_{\alpha}^{s,b}$, the bulk and surface regions have similar displacements at $T = 0.37$. However, neither region has displacements that have a Gaussian distribution. At $T = 0.36$, the displacements in both regions are still similar, and the heights of both peaks are nearly identical. At $T = 0.35$, one peak is visible for the particles in the surface region, while the bulk region has two peaks. When comparing $T = 0.35$ at different time separations, however, the time evolution of the particle displacements are similar with the faster surface particles approaching a Gaussian distribution for a smaller time separation.

Figure 4.13 shows a different comparison than the one shown in figure 4.12. Here the hypothesis is examined that the distributions of particle displacements in the bulk and surface regions will be similar if they are compared when both regions have approximately the same alpha relaxation time. In this case, the displacements are very different.
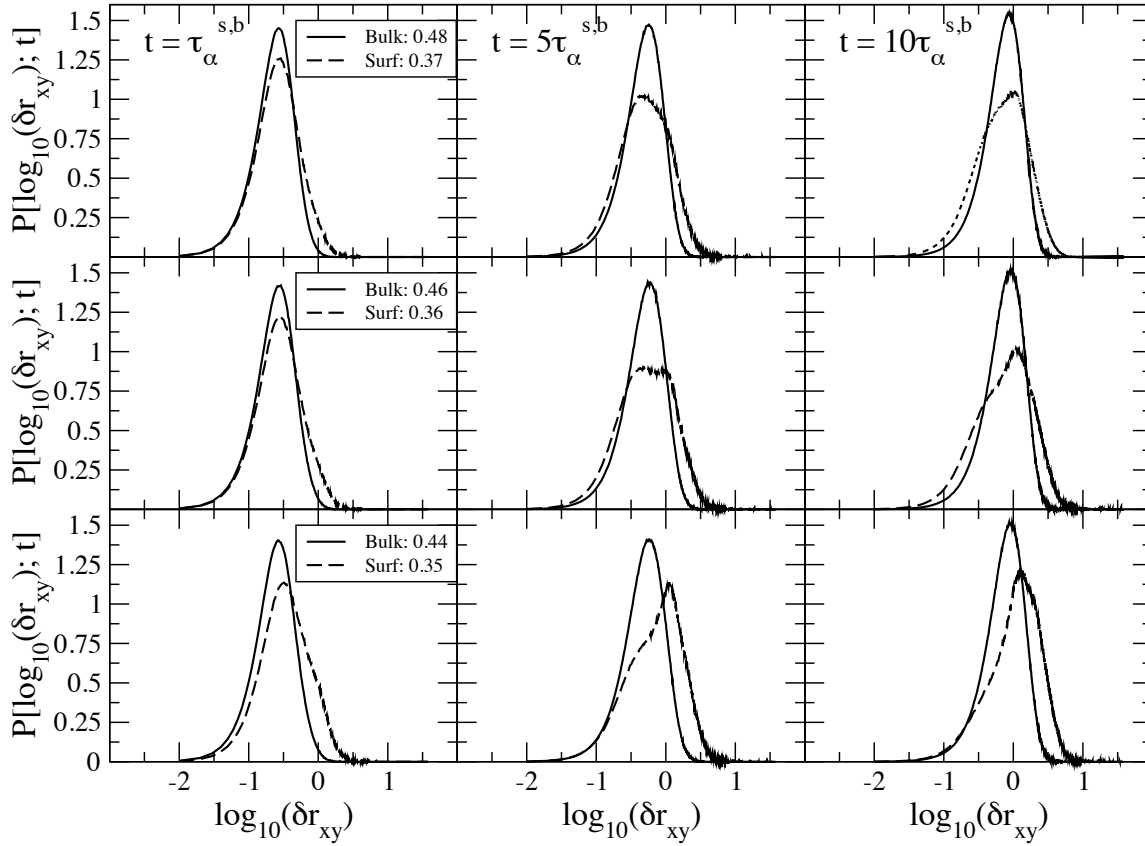
Figure 4.13: Comparison of the surface (dashed line) and bulk (solid line) $P[\log_{10}(\delta r_{xy}); t]$ at the same relaxation time. The time separation increases with each figure from left to right and displays values of $\tau_\alpha^{s,b}$, $5\tau_\alpha^{s,b}$, and $10\tau_\alpha^{s,b}$. The temperature increases in each figure from top to bottom and has values of $T = 0.35$, 0.36 and 0.37 for the bulk-like region of the film and $T = 0.42$, 0.43, and 0.47 for the surface layer.

Figure 4.13's layout is similar to figure 4.12's in that temperature increases from bottom panels to top panels, and the time separation increases from left panel to right panel. The surface layer's relaxation times were compared to the bulk region's relaxation times. It was concluded that the following temperature pairs have approximately the same surface and bulk relaxation times, respectively: 1) 0.35 and 0.42; 2) 0.36 and 0.32; and 3) 0.37 and 0.47. The displacements of the lower temperature surface layer were compared with the displacements of the higher temperature bulk layers.

At time separations of $\tau_\alpha^{s,b}$, the behavior of the bulk region's particle displacements is qualitatively similar to the behavior of the surface region's. However, the surface region at the lower temperature has a lower peak than the bulk region does at the higher temperature. Also, there is a distinct shoulder that appears in the surface region at the lower temperature that is not present in the bulk region. The widths of the curves in the surface layer are larger than the bulk region's for all temperature pairs, implying that the surface region at lower temperature undergoes larger displacements than the bulk region at higher temperatures. The larger displacements are evident due to $F_S^s(\mathbf{k}; t)$ having a faster initial decay than $F_S^b(\mathbf{k}; t)$.

The different dynamics between the two regions is very apparent for time separations of $5\tau_\alpha^{s,b}$. The distributions of particle displacements in the bulk region and the surface region have qualitatively different shapes. There is a wider spread of displacements in the surface region, but the displacements skew to the right when compared with the bulk region at higher temperatures. When the temperature is lowered, the shape and position of the distribution of the bulk region remains approximately the same. The surface region's distribution, however, undergoes distinct changes. At $T = 0.36$ there are two distinct peaks in the surface region's curve. However, there is not much change in the bulk region's curve when compared to its curve at $T = 0.48$. Even though the relaxation times for the two regions are similar, the distribution of displacements for the two regions at this timescale are very different. The two peaks in $P[\log_{10}(\delta r_{xy}); t]$ are still present in the surface region at $T = 0.35$, but more of the particles have larger displacements. This implies that the

87

difference between the bulk region's dynamics and the surface region's dynamics gets larger when the temperature is lowered and the two regions have similar relaxation times.

The displacements for particles starting in the surface region and particles starting in the bulk region are again different for time separations of $10\tau_\alpha^{s,b}$. This difference increases as the temperature is lowered, as was the case for $t = 5\tau_\alpha^{s,b}$. The height of $P[\log_{10}(\delta r_{xy}); t]$ in the bulk region has increased at all three temperatures. The curve of the surface region has a quantitatively similar shape at $T = 0.37$ and $T = 0.36$. The distributions are skewed to the right and there is evidence of hopping motion. At $T = 0.35$ the shoulder that was seen at the higher temperatures is no longer present.

Given this, we conclude that the temperature strongly influences the distribution of displacements in both regions. However, there is not a strong correlation between the dynamics of the two regions and the relaxation time. The hopping-like motion seen in simulations and experiments is not only present when the dynamics are slow.

As a further note, it is important to take into account the influence of particles that have left the surface layer within the time separation of the distribution. If the evidence above is to be trusted, these particles should have a negligible affect on the overall dynamics of the surface layer. To test that this was this case, the perpendicular mean squared displacement, $\langle \delta z^2 \rangle$, was calculated at the highest temperature, $T = 0.5$, and the lowest temperatures, $T = 0.35$. The perpendicular mean squared displacement is shown in figure 4.14.

At a time separation of $5\tau_\alpha$, it can be seen that $\sqrt{\langle \delta z^2 \rangle} \approx 0.7\sigma_{AA}$ at $T = 0.5$ and $\sqrt{\langle \delta z^2 \rangle} \approx 0.5\sigma_{AA}$ at $T = 0.35$. Thus, it can be concluded that the influence of particles that have left the surface layer within time separations of $5\tau_\alpha^s$ have little affect on the single particle dynamics of the surface layer given the surface layer's thickness of one σ_{AA}.
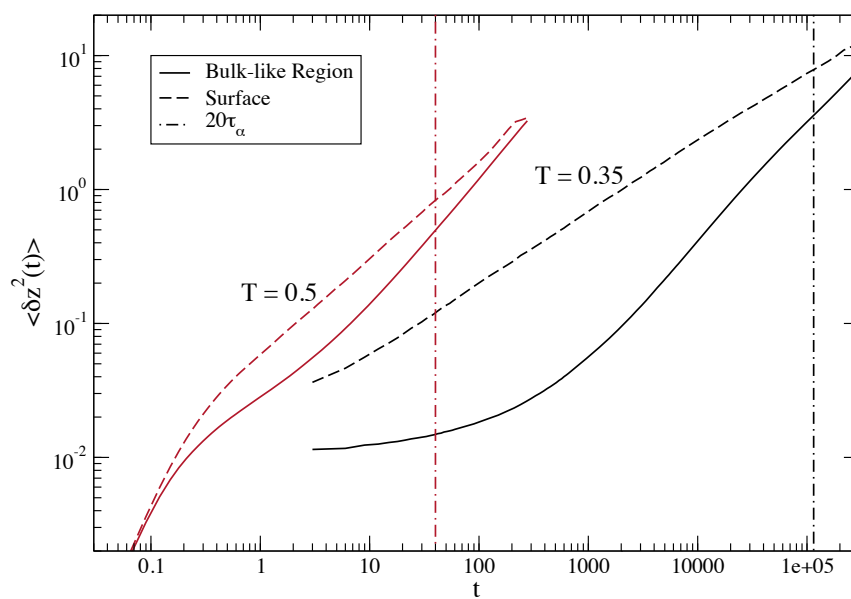
Figure 4.14: The mean squared displacements in the axial direction for particles that start in the bulk-like region (solid lines) and particles that start in the surface region (dashed-dotted lines). These are shown at temperatures of 0.5 (red) and 0.35 (black).

Chapter 5

Conclusions and Future Work

5.1   Confined Water in Silica Nanopores

In Chapters 2 and 3, we investigated the structure and dynamics of supercooled, SPC/E water confined in model MCM-41, hydrophilic, silica nanopores. To this end we calculated the self-intermediate scattering functions for water molecules confined: within pores of three sizes, and over a temperature range of 210 - 250 K. This temperature range allowed for the exploration of mildly supercooled water within the pores. We found that the density and the dynamics of the water within the pores was anisotropic, and so we studied the mean squared displacements and self-intermediate scattering functions as a function of the water molecules' starting point. The water molecules could start in two regions: the core region, and the shell region. The core region was near the center of the pore, while the shell region was close to the nanopore wall.

The water confined within the nanopores showed properties that are consistent with what is typically seen of supercooled liquids. In both the mean squared displacement and the self-intermediate scattering function a plateau developed at intermediate times for molecules that started either in the core or the shell region. The initial decay from the plateau of the self-intermediate scattering function is well described by a stretched exponential. At very long times, however, the decay becomes very slow and is poorly described by a stretched exponential. This is due to the dynamics being dependent on the starting positions of the water molecules.

For temperatures T $\leq$ 220 K, there is an overall slowing of the dynamics in the smaller pores. This occurs for molecules that start in the core region as well as those that start in the shell region. Since this occurred in the smaller pores, we conclude that, even with no large variations in the density of water molecules within the pore, the dynamics of the water molecules are affected by confinement. At the lowest temperature of 210 K, it was found that the 30 Å pore had slower dynamics than the 20 Å pore, which was not expected. This was found in both the diffusion coef-

ficients of the mean squared displacements and the alpha relaxation times of the self-intermediate scattering functions. To attempt to explain this behavior, it was hypothesized that the water within the nanopores was not at its equilibrium density. This was investigated in a lengthy study in which two-box Gibbs Monte Carlo simulations were used to attempt to find the water's equilibrium density. It was found that it was very difficult to determine whether the density of water molecules within the pore was at its equilibrium value. It is suggested that future work examine this problem and further investigate the methods used to hydrate the nanopores. Since the density of the water within the pores has been shown to change with temperature, it is necessary to investigate this issue [50]. We also suggest a study that investigates the self-intermediate scattering functions as a function of density.

A second explanation of the slower dynamics within the 30 Å pore than the 20 Å pore at 210 K is the presence of ice within the water confined in the 30 Å pore. To determine if this was the case, a tetrahedral order parameter was calculated as an attempt to determine if there was ice present in the system. It was found that the peak height of the parameter was slightly higher in the 30 Å pore than the 20 Å pore at 210 K. This is indicative of more tetrahedral order within the 30 Å pore, but is inconclusive as to the presence of ice. It is unknown whether this higher tetrahedral order affected the dynamics of the water within the pores. It is suggested that future studies explore this behavior.

We also calculated the temperature dependence of the translational-rotational decoupling approximation. We found that this quantity had little temperature dependence. Therefore, using the decoupling approximation in quasi-elastic neutron studies will result in very temperature independent interpretation of the results. Despite the water-pore system being anisotropic, it was found that the Rayleigh approximation was still an accurate description of the rotational self-intermediate scattering function. This was true for all temperatures.

5.2   Comparison of single particle dynamics at the center and on the surface of equilibrium glassy films

In Chapter 4, the single particle and average dynamics of a model supported glass-forming liquid film were examined via molecular simulation. The self-intermediate scattering functions were calculated for a region in the center of the film that had uniform, bulk-like properties, and for a surface layer defined to be one particle diameter from the edge of the liquid film. These functions were calculated at all temperatures. The self-intermediate scattering functions for particles that started in the bulk-like region of the film were found to be much more stretched than their counterparts that started with the surface region. The alpha relaxation times for the bulk-like region and surface layers were then calculated for all temperatures and compared with bulk NPT and NVT simulations. The NPT simulations had a pressure value equal to the pressure found in the bulk-like region and the NVT simulations had a volume equal to the average volume obtained from the NPT simulations. It was found that, while the NPT and NVT alpha relaxation times had, statistically, the same temperature dependence, the bulk-like region had alpha relaxation times that were statistically lower than the bulk simulations. To quantify results of the self-intermediate scattering functions being much more stretched in shape than the surface scattering functions, the ratio $\tau_\alpha^b/\tau_\alpha^s$ was calculated at all temperatures. It was found that this ratio increased exponentially with decreasing temperature, implying the result inferred by the shapes of the self-intermediate scattering functions.

Despite the conclusion that the average dynamics and self-intermediate scattering functions of the bulk-like region of the film and the surface layer of the film were quite different, it was found that the single particle displacements at a given time separation were quite similar when the bulk-like region and surface region were compared at the same temperature and same multiple of the bulk-like and surface layer relaxation time. The probability of the logarithm of displacements in the bulk-like region of the film displayed the characteristic two peak structure of supercooled liquids, implying hopping-like motion of the particles. The probability of the logarithm of displacements

in the surface layer also displayed a two peak structure and was remarkably similar to the bulk-like region's curve despite being . This was in spite of the large difference seen in the shape of the self-intermediate scattering functions. However, the two peak structure of the surface layer was shifted to larger displacement values and the two peaks were not as well localized when compared at the same multiple of the bulk-like relaxation time. This shift to a larger displacement value of the two peaks is reflected in the shape of the self-intermediate scattering functions.

When the dynamics of the single particle displacements were compared at temperatures such that the bulk-like region and surface layer had the same relaxation time, the resulting single particle displacements were quite different. The bulk-like region that had the same relaxation time as the surface layer was at a higher temperature, and the single particle displacement distribution displayed a single peak. Thus, the bulk-like region at this higher temperature did not display evidence of hopping-like motion of the particles. The surface layer single particle displacements, however, were calculated at low temperature, and displayed a two peak structure indicating hopping-like motion of the particles.

Thus, it can be concluded that the evolution of the distribution of single particle displacements is largely controlled by the temperature, and not by the population having a large relaxation time. This is an interesting conclusion given that, when the bulk-like region and the surface layer's single particle displacements have the same temperature dependence, the two regions are evolving on a vastly different timescale. The shape of the surface layer's self-intermediate scattering functions was not stretched like the bulk-like region, seemingly contradicting the above result; however, it was found that this was due to the two peak structure of the single particle displacements being shifted to large average displacement values.

An avenue for future work could be an investigation of the nature of the hopping-like behavior in the bulk-like region and the surface layer. The two peak structure of single particle displacements could be due to particles jumping between adjacent adsorption sites, rather than 3-dimensional cages of their nearest neighbors. This could provide a connection between the physics of surface diffusion and the physics of the diffusion of supercooled liquids.

Bibliography

[1] D. Frenkel and B. Smit, *Understanding Molecular Simulation: From Algorithms to Applications*. San Diego: Academic Press, 2002.

[2] M. Tuckerman, *Statistical Mechanics: Theory and Molecular Simulation*. Oxford: Oxford University Press, 2010.

[3] M.P. Allen and D.J. Tildesley, *Computer Simulation of Liquids*. Oxford: Oxford University Press, 1987.

[4] B. Guillot, "A reappraisal of what we have learnt during three decades of computer simulations on water", *J. Molec. Liquids* **101**, 219 (2002)

[5] J.P. Hansen and J.R. MacDonald, *Theory of Simple Liquids*. San Diego: Academic Press Inc., 1986.

[6] S. Iarlori, P. Carnevali, F. Ercolessi, and E. Tosatti, "Structure and correlations of a liquid metal surface: Gold". *Surface Science* **211**, 55 (1989).

[7] L.G. Pettersson and A. Nilsson, "The structure of water; from ambient to deeply supercooled", *J. Non-Cryst. Liquids* **407**, 399 (2015).

[8] A. K. Soper, "The radial distribution functions of water and ice from 220 to 673 K and at pressures up to 400 MPa", *J. Chem Phys.*,**258**, 121 (2000).

[9] S.A. Arrhenius, "About the heat of dissociation and the effect of temperature on the degree of dissociation of electrolytes". *Z. Phys. Chem* **4**, 96 (1889).

[10] H. Vogel, "The Law of Viscosity with Temperature", *Z. Phys.* **22**, 645 (1921).

[11] G. Tammann and G. Hesse, "The dependence of the viscosity on the temperature of supercooled liquids", *Z. Anorg. Allg. Chemic* **156**, 245 (1926).

[12] G. S. Fulcher, "Analysis of recent measurements of the viscosity of glasses", **J. Am. Ceram. Soc. 8**, 339 (1925).

[13] C. L. Jackson and G. B. McKenna, "The melting behavior of organic materials confined in porous solids", *J. Chem. Phys.* **93**, 9002âĂŞ9011 (1990).

[14] G.H. Findenegg, S. Jähnert, D. Akcakayiran, and A. Schreiber, "Freezing and Melting of Water Confined in Silica Nanopores", *ChemPhysChem* **9**, 2651 (2008).

[15] S. W. Lovesey, *Theory of Neutron Scattering from Condensed Matter* Oxford: Oxford University Press, (1984).

[16] M.D. Ediger, "Perspective: Highly stable vapor-deposited glasses", *J. Chem. Phys.* **147**, 210901 (2017).

[17] M. Thiesen, "Untersuchungen *ü*ber die Zustandsgleichung", *Annalen der Physik* **24** 467 (1885).

[18] N. Kuon, A.A. Milischuk, B.M. Ladanyi and E. Flenner, "Self-intermediate scattering function analysis of supercooled water confined in silica nanopores", *Journal of Chemical Physics*, vol. 146, 214501 (2017)

[19] S. Cerveny, F. Mallamace, J. Swenson, M. Vogel, and L. Xu, "Confined Water as Model of Supercooled Water" Chem. Rev. **116**, 7608 (2016).

[20] K. Amann-Winkel, R. Böhmer, F. Fujara, C. Gainaru, B. Geil, and T. Loerting, "Colloquium: WaterâĂŹs controversial glass transitions" Rev. Mod. Phys. **88**, 011002 (2016).

[21] C. A. Angell, "Supercooled Water", Ann. Rev. Phys. Chem. **34**, 593 (1983).

[22] S. Takahara, M. Nakano, S. Kittaka, Y. Kuroda, T. Mori, H. Hamano, and T. Yamaguchi, "Neutron Scattering Study on Dynamics of Water Molecules in MCM-41" J. Phys. Chem. B **103**, 5814 (1999).

[23] J.S. Beck, J.C. Vartuli, W.J. Roth, M.E. Leonowicz, C.T. Kresge, K.D. Schmitt, C.T.W. Chu, D.H. Olson, E.W. Sheppard, S.B. McCullen, J.B. Higgins, and J.L. Schlenker, "A New Family of Mesoporous Molecular Sieves Prepared with Liquid Crystal Templates" J. Am. Chem. Soc. **114**, 10834 (1992).

[24] P.C. Burris, D. Laage, and W.H. Thompson, "Simulations of the infrared, Raman, and 2D-IR photon echo spectra of water in nanoscale silica pores" J. Chem. Phys. **144**, 194709 (2016).

[25] D.T. Limmer and D. Chandler, "Phase diagram of supercooled water confined to hydrophilic nanopores" J. Chem. Phys. **137**, 044509 (2012).

[26] A.A. Milischuk and B.M. Ladanyi, "Structure and dynamics of water confined in silica nanopores" J. Chem. Phys. **135**, 174709 (2011).

[27] A.A. Milischuk, V. Krewald, and B.M. Ladanyi, "Water dynamics in silica nanopores: the self-intermediate scattering functions." J. Chem. Phys. **136**, 224704 (2012).

[28] A. Faraone, L. Liu, C-Y Mou, C-W Yen, S-H Chen, "Fragile-to-strong liquid transition in deeply supercooled confined water." J. Chem. Phys. **121**, 10843, (2004).

[29] Z. Wang, K-H Liu, L. Harriger, J.B. Leao, and S-H Chen, "Density of hydrophobically confined deeply cooled water investigated by small angle X-ray scattering" J. Chem. Phys. **141**, 014501 (2014).

[30] L. Liu, S-H Chen, A. Faraone, C-W Yen, and C-Y Mou, "Pressure dependence of fragile-to-strong transition and a possible second critical point in supercooled confined water." Phys. Rev. Lett. **95**, 117802 (2005).

[31] A. Faraone, L. Liu, C. Mou, P. Shih, J.R. Copley, and S. Chen, "Translational and rotational dynamics of water in mesoporous silica materials: MCM-41-S and MCM-48-S" J. Chem. Phys. **119**, 3963 (2003).

[32] B.W.H. van Beest, G.J. Kramer, and R.A. van Santen, "Force fields for silicas and aluminophosphates based on ab initio calculations" *Phys. Rev. Lett.* **64**, 1955 (1990).

[33] C.E Bertrand, Y. Zhang, and S-H Chen, Phys. Chem. Chem. Phys. **15**, 721 (2012).

[34] P. Gallo, M. Rovere, and E. Spohr, "Glass transition and layering effects in confined water: A computer simulation study" J. Chem. Phys. **113**, 11324 (2000).

[35] P. Gallo, M. Rovere, and S-H Chen, "Water confined in MCM-41: a mode coupling theory analysis" J. Phys. Condens. Matter **24**, 064109 (2012).

[36] D. Di Cola, A. Deriu, M. Sampoli, and A. Torcini, "Proton dynamics in supercooled water by molecular dynamics simulations and quasielastic neutron scattering" J. Chem. Phys. **104**, 4223 (1996).

[37] M. Bée, *Quasielastic Neutron Scattering* (Hilger, Bristol 1988).

[38] T.S. Gulmen and W.H. Thompson, "Model silica pores with controllable surface chemistry for molecular dynamics simulations" MRS Proceedings **899**, 0899 (2005).

[39] R.S. Luo and J. Jonas, "Raman scattering study of liquid ethylene glycol confined to nanoporous silica glasses" J. Raman Spectrosc. **32**, 975 (2001).

[40] Y. Hiramara, T. Takahaski, M. Hino, and T. Sato, "Polarizability anisotropy relaxation in nanoconfinement: Molecular simulation study of water in cylindrical silica pores" J. Colloid Interface Sci. **184**, 349 (1996).

[41] A. Z. Panagiotopoulos, "Direct determination of phase coexistence properties of fluids by Monte Carlo simulation in a new ensemble" Mol. Phys. 61 813-826 (1987).

[42] A. Z. Panagiotopoulos; N. Quirke; M. Stapleton; D. J. Tildesley, "Phase equilibria by simulation in the Gibbs ensemble" Mol. Phys. 63 527-545 (1988).

[43] M. G. Martin, "MCCCS Towhee: a tool for Monte Carlo molecular simulation" Mol. Simulat. 39 1212-1222 (2013).

[44] G. C. Boulougouris, I.G. Economou, and D.N. Theodorou, "Engineering a Molecular Model for Water Phase Equilibrium over a Wide Temperature Range" J. Phys. Chem. B **102**,1029 (1998).

[45] J.R.Errington, K. Kiyohara,K.E.Gubbins,and A. Z. Panagiotopoulos, "Monte Carlo simulation of high-pressure phase equilibria in aqueous systems" Fluid Phase Equilib. **150**, 33 (1998).

[46] J. Vorholz, V. I. Harismiadis, B. Rumpf, A. Z. Panagiotopoulos, and G. Maurer, "Vapor+liquid equilibrium of water, carbon dioxide, and the binary system, water+carbon dioxide, from molecular simulation" Fluid Phase Equilib. **170**,203 (2000).

[47] W. Smith and T.R. Forester, "DL_POLY_2.0: a general-purpose parallel molecular dynamics simulation package." J. Molec. Graphics **14**, 136 (1996).

[48] M.P. Allen and D.J. Tildesley *Computer Simulation of Liquids*. (Oxford University Press, New York, 1987).

[49] H. J. C. Berendsen, J. R. Grigera, and T. P. Straatsma, "The Missing Term in Effective Pair Potentials" J. Phys. Chem. **91**, 6269 (1987).

[50] Y. Zhang et al, PANS **108**, 12206 (2011).

[51] A. Bródka, "Diffusion in restricted volume" Mol. Phys. **82**, 1075 (1994).

[52] A. Bródka and T.S. Zerda, "Properties of liquid acetone in silica pores: Molecular dynamics simulation" J. Chem. Phys. **22**, 6319 (1996).

[53] T.S. Gulmen and W.H. Thompson, "Grand canonical Monte Carlo simulations of acetonitrile filling of silica pores of varying hydrophilicity/hydrophobicity." Langmuir **22**, 10919 (2006).

[54] L Liu, A Faraone, C-Y Mou, C-W Yen, and S-H Chen, "Slow dynamics of supercooled water confined in nanoporous silica materials" J. Phys. Condens. Matter. **16**, S5403 (2004).

[55] V.F. Sears. "Neutron scattering lengths and cross sections" Neutron News **3**, 26 (1992).

[56] V.F. Sears, "Cold Neutron Scattering By Molecular Liquids: III. Methane" Can. J. Phys. **45**, 237 (1967).

[57] J. Errington and P. Debenedetti, "Relationship between structural order and the anomalies of liquid water" Nature **409**, 318 (2001).

[58] P.-L. Chau and A.J. Hardwick, "A new order parameter for tetrahedral configurations" Mol. Phys. **93**, 511 (1998).

[59] S.S. Dalal, A. Sepúlveda, G.K. Pribil, Z. Fakhraai and M.D. Ediger, "Density and bire-fringence of a highly stable α,α,β-trisnaphthylbenzene glass." J. Chem. Phys. **136**, 204501 (2012).

[60] C. Rodríguez-Tinoco, J. Ràfols-Ribé , M. González-Silveira and J. Rodríguez-Viejo, Sci. Rep, **6**, 204501 (2012).

[61] S.F. Swallen, K.L. Kearns, M.K. Mapes, Y.S. Kim, R.J. McMahon, M.D. Ediger, T. Wu, L. Yu, and S. Satija, "Organic glasses with exceptional thermodynamic and kinetic stability." Science **315**, 35607 (2016).

[62] E. Leon-Gutierrez, A. Sepulveda, G. Garcia, M.T. Clavaguera-Mora, and J. Rodruíguez-Viejo, "Stability of thin film glasses of toluene and ethylbenzene formed by vapor deposition: an in situ nanocalorimetric study" Phys. Chem. Chem. Phys. **12**, 14693 (2010).

[63] K.L. Kearns, M.D. Ediger, H. Huth, and C. Schick, "Observation of low heat capacities for vapor-deposited glasses of indomethacin as determined by AC nanocalorimetry" J. Phys. Chem. Lett. **1**, 388 (2010).

[64] C. Neuber, A. Ringk, T. Kolb, F. Wieberger, P. Strohriegl, H.-W. Schmidt, V. Fokkema, M. Cooke, C. Rawlings, U. Drig, A.W. Knoll, J.-F. de Marneffe, P. De Schepper, M. Kaestner, Y. Krivoshapkina, M. Budden, I.W. Rangelow, SPIE Advanced Lithography, edited by D. Resnick and C. Bencher (International Society for Optics and Photonics, 2014), 90491V.

[65] B.C. Hancock and G. Zografi, "Characteristics and significance of the amorphous state in pharmaceutical systems." J. Pharm. Sci. **86**, 1-12 (1997).

[66] H.B. Yu, Y.S. Luo, and K. Samwer, "Ultrastable Metallic Glass" Adv. Materials **25**, 5904 (2013).

[67] L. Berthier and M.D. Ediger, "Facets of glass physics" Phys. Today **69**, No. 1, 40 (2016)

[68] J.D. Stevenson and P.G. Woylnes, "On the surface of glasses" J. Chem. Phys. **129**, 234514 (2008)

[69] F. Chen, C.H. Lam and O.K C. Tsui, "The Surface Mobility of Glasses" Science **343** 975 (2014)

[70] C. R. Daley, Z. Fakhraai, M. D. Ediger, and J. A. Forrest, "Comparing surface and bulk flow of a molecular glass former" Soft Matter **8**, 2206 (2012)

[71] Y. Zhanga and Z. Fakhraai, "Decoupling of surface diffusion and relaxation dynamics of molecular glasses" Proc. Natl. Acad. Sci. U.S.A. **114**, 4915 (2017).

[72] K.L. Kearns, M D. Ediger, H. Huth, and C. Schick, "Observation of low heat capacities for vapor-deposited glasses of indomethacin as determined by AC nanocalorimetry" J. Phys. Chem. Lett. **1**, 388 (2010).

[73] L. Zhu, C.W. Brian, S.F. Swallen, P.T. Straus, M.D. Ediger, and L. Yu, "Surface Self-Diffusion of an Organic Glass" Phys. Rev. Lett. **106**, 256103 (2011).

[74] L. Berthier, P. Charbonneau, E. Flenner, and F. Zamponi, "Origin of Ultrastability in Vapor-Deposited Glasses" Phys. Rev. Lett. **119**, 188002 (2017)

[75] G. Sun, S. Saw, I. Douglass, and P. Harrowell, "Structural Origin of Enhanced Dynamics at the Surface of a Glassy Alloy" Phys. Rev. Lett. **119**, 245501 (2017).

[76] T.X. Xiang and B.D. Anderson, "Molecular dynamics simulation of amorphous indomethacinâĂŞpoly(vinylpyrrolidone) glasses: Solubility and hydrogen bonding interactions" Mol. Pharmaceutics **10**, 102 (2013).

[77] P.H. Lin, I. Lyubimov, L. Yu, M. D. Ediger, and J.J. de Pablo, "Molecular modeling of vapor-deposited polymer glasses." J. Chem. Phys. **140**, 204504 (2014).

[78] R. Malshe, M.D. Ediger, L. Yu, and J.J. de Pablo, "Evolution of glassy gratings with variable aspect ratios under surface diffusion." J. Chem. Phys. **134**, 194704 (2011).

[79] M.D. Ediger, "Spatially heterogeneous dynamics in supercooled liquids" Annu. Rev. Phys. Chem. **51**, 99 (2000).

[80] L. Berthier and G. Biroli, "Theoretical perspective on the glass transition and amorphous materials" Rev. Mod. Phys. **83**, 587 (2011).

[81] Y. Gebremichael, T.B. Schroder, F.W. Starr, and S.C. Glotzer, "Spatially correlated dynamics in a simulated glass-forming polymer melt: Analysis of clustering phenomena" Phys. Rev. E **65** 030101(R) (2001).

[82] N. Lacevic, F.W. Starr, T.B. Schroder, V.N. Novikov, and S.C. Glotzer, "Growing Correlation Length on Cooling Below the Onset of Caging in a Simulated Glass-Forming Liquid" Phys. Rev. E **66**, 030101(R) (2002).

[83] N. Lacevic, F.W. Starr, T.B. Schroder, and S.C. Glotzer, "Spatially heterogeneous dynamics investigated via a time-dependent four-point density correlation function" J. Chem. Phys. **119**, 7372 (2003).

[84] M. Vogel and S.C. Gltozer, "Spatially Heterogeneous Dynamics and Dynamic Facilitation in a Model of Viscous Silica" Phys. Rev. Lett. **92**, 255901 (2004).

[85] E. Flenner and G. Szamel, Phys. Rev. E **79**, 051502 (2009).

[86] E. Flenner and G. Szamel, Phys. Rev. Lett. **105**, 217801 (2010).

[87] E. Flenner, H. Staley, and G. Szamel, "Universal features of dynamic heterogeneity in super-cooled liquids." Phys. Rev. Lett. **112**, 097801 (2014).

[88] S. Karmakar, C. Dasgupta, and S. Sastry, "Glass Transition in Supercooled Liquids with Medium-Range Crystalline Order" Phys. Rev. Lett. **105**, 015701.

[89] E. Flenner and G. Szamel, "Fundamental differences between glassy dynamics in two and three dimensions" Nature Commun. **6**, 7392 (2015).

[90] S. Vivek and E.R. Weeks, "Glassy dynamics of dense particle assemblies on a spherical substrate" J. Chem. Phys. **147**, 134501 (2017).

[91] S. Vivek, C.P. Kelleher, P.M. Chaikin, and E.R. Weeks, "Long-wavelength fluctuations and the glass transition in two dimensions and three dimensions." PNAS **114**, 1850 (2017).

[92] B. Illing, S. Fritschi, H. Kaiser, C. L. Klix, G. Maret, and P. Keim, "Mermin-Wagner fluctuations in 2D amorphous solids." PNAS **114** 1856 (2017).

[93] B.D. Todd, D. Evans and P. Davis, "Pressure tensor for inhomogeneous fluids" Phys. Rev. E **52**, 1627 (1995)

[94] I. Lyubimov, M.D. Ediger, and J.J. de Pablo, "Perspective: Highly stable vapor-deposited glasses" J. Chem. Phys. **139**, 144505 (2013).

[95] L. Berthier and G. Biroli, "Theoretical perspective on the glass transition and amorphous materials" Rev. Mod. Phys. **83**, 587 (2011).

[96] D.R. Reichman, E. Rabani and P.L. Geissler, "Dynamical heterogeneities in an attraction driven colloidal glass" J. Phys. Chem. B **109**, 14654 (2005).

[97] A.M. Puertas, M. Fuchs, and M.E. Cates, "Dynamical heterogeneities close to a colloidal gel" J. Chem. Phys. **121**, 2813 (2004).

[98] M. E. Cates, M. Fuchs, K. Kroy, W. C. K. Poon and A. M. Puertas, "Theory and simulation of gelation, arrest and yielding in attracting colloids" J. Phys. Cond. Mat. **16**, S4861 (2004).

[99] E. Flenner and G. Szamel, "Relaxation in a glassy binary mixture: Mode-coupling-like power laws, dynamic heterogeneity, and a new non-Gaussian parameter" Phys. Rev. E **72**, 011205 (2005).

[100] E. Flenner and G. Szamel, "'Relaxation in a glassy binary mixture: Comparison of the mode-coupling theory to a Brownian dynamics simulation" Phys. Rev. E **72**, 031508 (2005).

[101] M.P. Ciamarra, R Pastore and A Coniglio, "Particle jumps in structural glasses" Soft Matter **12**, 358 (2016).

[102] W. Zhang, J.F. Douglas, and F.W. Starr, "Effects of a "bound" substrate layer on the dynamics of supported polymer films" J. Chem. Phys. **146**, 203310 (2017).

[103] W. Kob and H. C. Anderson, "Scaling Behavior in the β -Relaxation Regime of a Supercooled Lennard-Jones Mixture" Phys. Rev. Lett. **73**, 1376 (1994).

[104] W. Kob and H. C. Anderson, "Testing mode-coupling theory for a supercooled binary Lennard-Jones mixture I: The van Hove correlation function" Phys. Rev. E. **51**, 4626 (1995).

[105] W. Kob and H. C. Anderson, "Testing mode-coupling theory for a supercooled binary Lennard-Jones mixture. II. Intermediate scattering function and dynamic susceptibility" Phys. Rev. E. **52**, 4134 (1995).

[106] See http://codeblue.umich.edu/hoomd-blue for information about the HOOMD-blue simulation package

[107] B. Doliwa and A. Heuer, "Energy barriers and activated dynamics in a supercooled Lennard-Jones liquid" Phys. Rev. E **67**, 03501(R) (2003).

[108] E.R. Weeks and D.A. Weitz, "Properties of Cage Rearrangements Observed near the Colloidal Glass Transition" Phys. Rev. Lett. **89**, 095704 (2002).

[109] S. P. Niblett, V.K. de Souza, J. D. Stevenson and D. J. Wales, "Dynamics of a molecular glass former: Energy landscapes for diffusion in ortho-terphenyl" J. Chem. Phys. **145**, 024505 (2016).

[110] R Pastore, G Pesce, A Sasso, and M.P. Ciamarra, "Many facets of intermittent dynamics in colloidal and molecular glasses" Phys. Chem. Lett. **8**, 1562 (2017).